Scuola Internazionale Superiore di Studi Avanzati

PhD course in Theory and Numerical Simulation of Condensed Matter

---

Coupled quantum kicked rotors: a study about dynamical localization, slow heating and thermalization

Thesis submitted for the degree in *Doctor Philosophiae*

Supervisors
Prof. Alessandro Silva
Prof. Rosario Fazio

Candidate
Simone Notarnicola

Academic year 2017/2018

Declaration

Il presente lavoro costituisce la Tesi presentata da Simone Notarnicola, sotto la direzione del Prof. Alessandro Silva e del Prof. Rosario Fazio, al fine di ottenere il titolo di Philosophiae Doctor presso la SISSA, Curriculum in Teoria e Simulazione Numerica della Materia Condensata, Area di Fisica. Ai sensi dell'art. 1, comma 4 dello Statuto della SISSA, pubblicato sulla G.U. n. 36 del 13.02.2012, il predetto titolo è equipollente al titolo di Dottore di Ricerca in Fisica.

Trieste, Anno Accademico 2017-2018.

Abstract

Periodically driven systems are nowadays a very powerful tool for the study of condensed quantum matter: indeed, they allow the observation of phenomena in huge contrast with the expected behavior of their classical counterparts. An outstanding example is dynamical localization: this phenomenon consists in the prevention of heating despite an external periodic perturbation. It has been defined for the first time in a single particle model, the kicked rotor. This chaotic system undergoes an unbounded heating in time in its classical limit; on the opposite, in the quantum regime, the kinetic energy grows until a saturation value is reached and the system stops heating. In my thesis I consider a chain of coupled quantum kicked rotors in order to investigate the fate of dynamical localization in presence of interactions. I remarkably show that a dynamically localized phase persists in the quantum system also in presence of interactions. This is an unexpected behavior since periodically driven, interacting, non-integrable quantum systems are expected to heat up to an infinite temperature state. Moreover, I find a genuine quantum dynamics also in the delocalized phase: the heating is not diffusive, as it happens in the classical system, but it follows a sub-diffusive power law. A focus on the properties of the Floquet eigenstates and operators matrix properties gives interesting hints, still under investigation, for a possible justification of the above mentioned slow heating.

Contents

Introduction

Periodically driven systems surround us and, in some cases, are part of us. For example, at the origin of our perception of sound, there is a periodic perturbation, namely the sound wave, which hits our eardrums: in this way, energy is transferred through the wave to our body and activates a chain of processes whose result is our ability to hear. Let us add that our living body may be considered a *self-periodically* driven system, since the periodic contractions of our hearth make all our vital functions possible.

An example of classical periodically driven system is a nail beaten from a hammer into a wall: the energy provided by the hammer passes from the nail to the wall with the effect of creating a hole. There are also systems in which the effect of the perturbation is not dispersed to an external environment. Consider for example a rigid and thermally insulating box containing a gas and an engine made up by two touching disks rotating in opposite directions: the friction between the disks generates heat which is absorbed by the gas and not released outside. In our work we focus on this second class of systems.

While the responses of classical systems to periodic drivings may be kinetic effects, deformations or heating, the scenario changes dramatically as we move from to quantum condensed matter systems [1] since periodic drivings can induce effects which do not have a classical counterpart. This research branch, called Floquet engineering [2], has combined in the recent years theoretical and experimental efforts devoted to the observation of genuine quantum phases of matter. An outstanding example is that of topological effects [3]: periodic drivings obtained via light modulation have been applied to different systems such as graphene [4], quantum wires made up of cold atoms [5] as well as quantum wells [6] for the investigation of phenomena ranging from Quantum Hall Effect [7, 8, 9, 10] to Floquet insulators [11, 12]. Other collective phenomena which can be induced in materials by periodic drivings are superconductivity [13, 14, 15, 16] in cuprates [17] and superfluidity [18, 19], but the list of all the current applications of this out of equilibrium protocol may continue.

An issue which must be taken into account in the study of the previous systems is the role played by interactions in quantum many-body systems: this field has been made accessible to experiments only recently thanks to new experimental achievements [20], as for example the realization of ultracold atoms trapped in optical lattices. These setups are composed by a grid of counter-propagating laser beams which create a spatially-periodic potential. An ultracold gas of atoms ($N \sim 10^3 - 10^4$ atoms at temperature $T \sim 10^{-2}K$) is then released on it and its dynamics is investigated. This setup constitutes a quantum simulator [21] for studying a variety of lattice models and phenomena whose observation is prevented in real materials: impurities, lattice

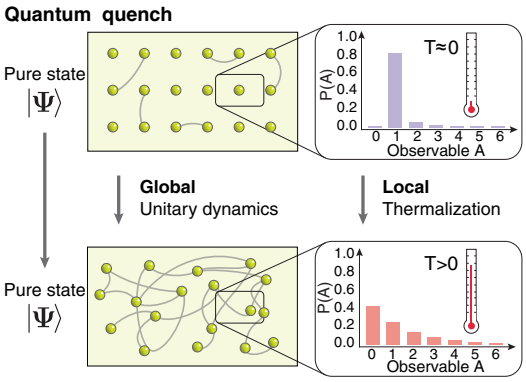

Figure 1: Thermalization process in a closed, interacting quantum many-body system. Figure taken from [31].

vibrations and external noise create entanglement between the environment and the system. As a consequence, unitarity in the evolution is lost and the system collapses in an uninteresting incoherent mixture of states: all these spurious effects are strongly suppressed in optical lattices, in which the artificial nature of the lattice eliminates impurities and the low temperature limits the coupling of the system to external sources of noise (for a review see [22] or [23]). Among the phenomena which have been studied via ultracold atoms in optical lattices let us mention for example the Mott insulator phase transition observed in a Bose Einstein condensate [24] as well as in fermionic ultracold gases [25]. More recent experiments have been devoted to the study of long range interactions [26], synthetic dimensions [27] and lattice gauge theories [28, 29].

Ultracold atoms setups opened the way also to the experimental investigation of thermalization in quantum systems [30, 31], whose mechanism can be described as follows. Let us consider a closed system and prepare an initial state in an eigenstate of a certain local observable $\hat{A}$: due to this choice the initial state is pure in the representation of the eigenstates of the observable $\hat{A}$ and the initial entropy is therefore negligible (upper panels in Figure 1). If an interaction is switched on, for example via a quench, different regions of the system spatially separated start interacting between each other: the global state remains pure because the dynamics is unitary but entanglement arises between different portions of the system. At equilibrium, each local region of the system is now described by a mixed density matrix and, in particular, the expectation value of the observable $\hat{A}$ is given by a classical superposition of its different possible values (bottom panels of Figure 1). It has been observed that this expectation value is independent of the choice of the initial state and coincide with the microcanonical expectation value: the conceptual framework for explaining quantum thermalization is still today object of intense debate. The main established assumptions are enclosed in the Eigenstate Thermalization Hypothesis, which will be discussed in the following (for a review see [32]). Understanding thermalization in quantum systems is important from several points of view: first, it poses fundamental questions, as for example how can a closed system undergoing unitary dynamics reach a maximum entropy state [33]. On the other hand it still stimulates a lot research regarding the possible ways to prevent it. Apart from quantum integrable systems [34],

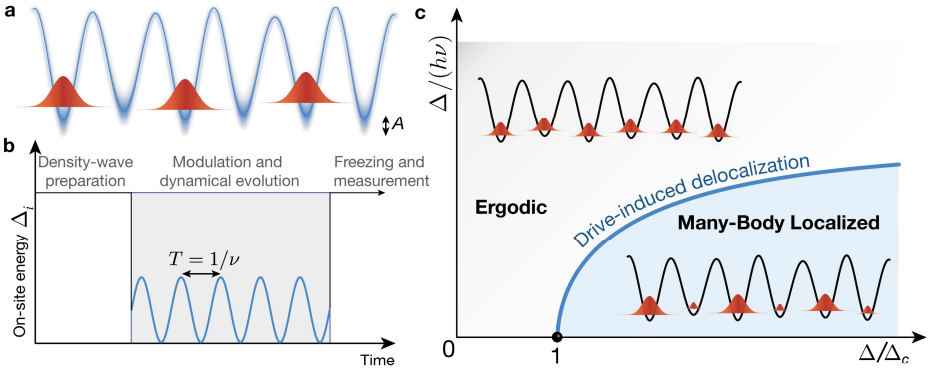

Figure 2: Initial state (a), evolution protocol (b) and phase diagram (c) of a periodically driven interacting fermions system exhibiting many-body localization at high frequencies. Figure taken from [41].

which do not thermalize, a novel quantum phase in which thermalization is prevented is called many-body localization [35, 36]. It constitutes the extension of the known results concerning Anderson localization theory [37, 38] in one dimensional lattices to interacting fermionic systems: in particular, it predicts the existence of a transition from a metal to insulator which takes place as a disordered local potential is increased above a critical value. The mechanism which leads to this phase is the existence of an extensive set of quasi local operators which in presence of disorder behaves as integral of motion and induces an effective integrability into the system [39, 40]. These operators form a set of effective local integrals of motion: as an effect, a slow, logarithmic growth of the entanglement is observed.

Our goal is to study thermalization and localization phenomena in periodically driven interacting quantum systems. It is generally expected that these systems heat up in time up to a structureless state called the infinite-temperature state [42, 43, 44] due to the absence of energy conservation; nevertheless, the absence of thermalization has been observed, for example, in many-body localized periodically driven systems in the case of a weak driving[45]. In other works it has been pointed out that many-body localization survives if the frequency of the driving is so high that the relaxation time scale of the system is larger than the driving time scale [46, 47]. This behavior has been successfully tested in two recent experiments concerning chains of spins and of interacting fermions [41, 48]: in the following we describe the second one. An initial state is prepared by imposing a nonzero imbalance of the occupations of even and odd sites (panel (a) in Figure 2). After a quench the system is let free to evolve under a periodic driving (panel (b)). If the disorder is larger than its critical value there is an interval of high frequencies in which many-body localization can be observed (phase diagram in panel (c)): the initial imbalance persists in time, revealing that the system is not thermalizing. At lower frequencies instead the system reaches a thermal state in which the initial imbalance has disappeared. Apart from absence of thermalization, there have been works focusing also on the intermediate temporal regime which precedes thermalization: indeed, while in classical systems this process is generally governed by the linear Joule heating, despite some particular case which will be discussed later on, periodically driven quantum systems can, instead, exhibit

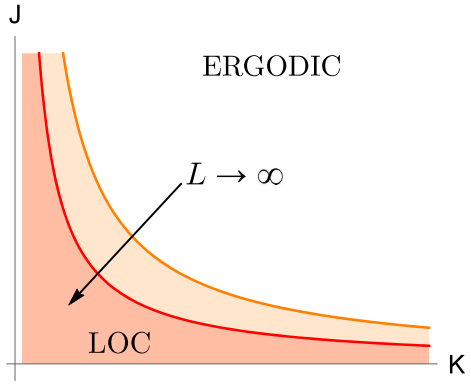

Figure 3: The dynamical phases of our model are pictorially represented in the kick parameters space. The localized phase corresponds to small values, while the ergodic one emerges as they are increased. The delocalized region in which anomalous thermalization is observed (orange) is close to the limit between the localized and the delocalized region. The localized region disappears as L increases.

prethermal regimes [49, 50, 51] analogous to what has been observed in the dynamics of out of equilibrium system after a quench [52], and slow heating [53]. Stable regimes in quantum interacting systems have been found also in absence of disorder, as it has been observed numerically in the case of a chain of coupled Kapitza pendula [54] in the high frequency limit. Another recent example of a non-ergodic many-body behavior has been found in the so called time crystals, characterized by a spontaneous breaking of the time translation invariance [55]; in particular periodically driven systems allowed the observation of Floquet time crystals [56, 57]: in these system the driving as a period T but it is found that the system has a periodicity $T' = nT$ with n integer, breaking the time translational symmetry of the Hamiltonian.

In this Thesis we focus on a chain of coupled quantum kicked rotors. The single kicked rotor describes the dynamics of a rotor, characterized by its angular momentum and phase, which is periodically kicked by a term dependent on the phase and proportional to a given amplitude. It is considered a paradigmatic model for the study of classical chaos [58] and has been playing a fundamental role in the definition of quantum chaos since the beginning of its investigation [59, 60, 61]. As we will explain more in detail, the classical model exhibits dynamical localization for sufficiently small kicks: the kinetic energy does not grow in time and the system is said to be quasi-integrable. For large values of the kick, instead, the energy grows linearly in time. On the other side, the quantum kicked rotor (QKR) exhibits a dramatic different behavior: the kinetic energy reaches a finite asymptotic value and then stops growing independently on the strength of the kick independently on the kick strength. This model has been the first case in which quantum dynamical localization has been predicted. The explanation of this phenomenon makes use of a mapping between the QKR and a time independent model [60] describing a particle hopping in a disordered lattice which undergoes Anderson localization [37]: with an analogous mechanism the dynamics of initial state of the QKR is localized in the angular momentum space, imposing a limitation to the growth of the kinetic energy. Our purpose is to extend the known results about the single quantum kicked rotor to a version of the same

problem in which L quantum kicked rotors interact between each other. We want to understand if dynamical localization persists in presence of interaction and investigate the behavior of the system if localization is lost. The starting point of our research consists in understanding if the above mentioned mapping can extended to the case of $L > 1$ rotors: the first result that we reach is building such a mapping between our periodically driven, interacting model and a disordered lattice: the one dimensional space in the single QKR is replaced, in our case, by a L-dimensional disordered lattice. The lattice model that we obtain is expected to undergo the Anderson localization transition: indeed we show that it is characterized by a quasi random potential and by short-range hopping coefficients. This result allows us to predict that a system with $L > 1$ rotors exhibits a dynamically localized phase, where the spreading of a given initial state in the angular momentum representation of the Hilbert space is suppressed[1]. In particular, for $L = 3$ we expect to find a dynamically localized phase and a delocalized one.

Our analysis continues with the study of these two dynamical regimes in the coupled kicked rotors system for $L = 3$. We use exact diagonalizaton for distinguishing between the dynamically localized and delocalized phases: the tools we use are based on the Floquet theory, according to which the dynamical properties of a driven system can be inferred by analyzing the spectrum and the eigenstates of the propagator over one period, called Floquet operator. This operator plays the same role played by the Hamiltonian in characterizing the dynamics of a time independent system. We find that for $L = 3$ rotors, the system exhibits dynamical localization for small values of the kick parameters. As instead they are increased we enter the delocalized phase, in which the system absorbs energy in time. In Figure 3 we pictorially represent the two delocalized and localized phases (white and red respectively) in the kick parameters space: J is the interaction strength and K a kick term which acts on each rotor separately. We remarkably observe that the growth of the kinetic energy obeys a power law in time, a behavior which differs from the linear growth characteristic of the classical counterpart. This behavior is confirmed by studying an inhomogeneous version of the model in which all the rotors are subject to a kicked interaction and only one rotor receives an additional kick; moreover,we observe that rotors which receive different kicks exhibit qualitatively different heating regimes even though the system is dynamically delocalized.

After the study of the system in the case $L = 3$ we continue our analysis focusing on the dynamics of the system at larger values of L, in order to extrapolate those features which may persist in the thermodynamic limit. First, we find that the region in which the system exhibits dynamical localization disappears as the number of rotors is increased. This observation is supported by a calculation, taken from [63], which shows that an infinite dimensional disordered lattice does not exhibit an Anderson localized phase: from the mapping illustrated above, we conclude that the dynamically localized phase is expected to vanish in the thermodynamic limit. We perform a mean field calculation in order to study the behavior of the system in the thermodynamic limit of the fully connected model. In this case the mean field approximation is exact: we observe that the kinetic energy grows in time with a power law, similarly to the

[1] In the case $L = 2$ the system is expected to be always Anderson localized with the characteristic localization length exponentially increasing as disorder is diminished, while for $L \geqslant 3$ a transition takes place from delocalized to localized as the disorder strength is increased [62].

case $L = 3$. In order to understand if also the model with nearest neighbor coupling exhibits the same behavior in the limit of large L we use exact diagonalization for investigating the delocalized region for $L > 3$.

The evolution of the kinetic energy can be numerically computed for $L = 4$, in which subdiffusion is still observed. Athough it is not possible to investigate the dynamics for larger L, a different analysis can be performed. Indeed, we observe that as the power law heating is observed, the distribution of the off diagonal elements of the kinetic energy operator does not satisfy the ETH and quantum chaos assumptions. Moreover, we find that the distributions obtained with different valus of L coincide in different regions of the parameters space. This regime is observed in the orange region in Figure 3. Note that the localized region soon becomes very narrow as L is increased: as a consequence, the anomalous delocalized region does not move for large values of L. Further investigations are currently going on to understand if these results imply that the power law heating survives in the limit of large L but nevertheless they reveal an anomalous ergodic behavior which persists at large L. This result is in agreement with similar observations relative to time independent as well as periodically driven systems [64]. A full understanding in the study of these anomalous thermalization signatures is still missing [65] and our work aims to put the basis for finding new answers in this direction.

The chapters of the thesis are organized as follows.

- In Chapter 1 we discuss quantum thermalization and ergodicity. Then we introduce the Floquet formalism for the study of periodically driven systems, extending the notion of thermalization to this class of models.

- In Chapter 2 we introduce the coupled quantum kicked rotors model, starting from a brief overview of the known results concerning the single kicked rotor; the relevant observables for the study of the dynamics of the system are defined.

- In Chapter 3 we present the result for the case $L = 3$. The first section is taken from [63] and illustrate the mapping between the system with L coupled rotors and a time independent L dimensional disordered lattice problem. In the second section we analyze the features of the system in its localized and delocalized phases. In the last section a different, inhomogeneous model is considered in which the rotors are uniformly coupled and one of them receives an additional kick: the aim is to study the relation between the dynamical and spatial localization phenomena.

- In Chapter 4 we investigate the case of larger L. In the first section we present a mean field calculation, taken from [63]. In the second section we extend the results found with $L = 3$: by using exact diagonalization, we investigate the subdiffusive heating and the anomalous thermalization signatures which persist at larger values of L.

- In the Conclusions we summarize the results presented in the thesis and discuss possible directions which are left for future work.

Chapter 1

Quantum thermalization and periodically driven systems

In this Chapter we review the notions of thermalization and ergodicity in time independent quantum systems; then we introduce the Floquet formalism and we extend the definition of thermalization to periodically driven systems. In the first section we derive the Eigenstate Thermalization Hypothesis and in the second one we explain how quantum chaos is responsible for ergodicity in quantum systems, showing its connection with Random Matrix Theory. The third section is devoted to the definition of the Floquet operator to study the dynamics of periodically driven systems; the Inverse participation ratio is defined for inferring localization or delocalization from the structure of the Floquet eigenstates. Finally we define thermalization in periodically driven systems; in particular we introduce the level spacing distribution and level spacing ratio for studying the spectral properties of the Floquet operator.

1.1 The Eigenstate Thermalization Hypothesis

In the Introduction we described the equilibration process in an isolated non-integrable system, showing that the system behaves as a bath for the thermalization of its own local components. Understanding this mechanism has been a debated topic for a long time; a fundamental boost came from the recent experiments [66, 67] in which the thermalization process has been observed by using ultracold atoms and the existence of prethermal regimes has been pointed out. In the following we illustrate the main issues which brought to the formal definition of quantum thermalization: to this purpose, let us start with a short introduction about thermalization in a non-integrable isolated classical system. Let us recall that thermalization is prevented in integrable systems, namely those systems with N degrees of freedom which admit $N-1$ integrals of motion. Thermalization in classical mechanics is strongly related to irreversibility: given a time independent system prepared in an arbitrary initial state, it is said to thermalize if it evolves toward an asymptotic state which is independent from its microscopic initial conditions and is characterized by a set of few thermodynamic macroscopic observables. Moreover, it has been proven that the equilibrium distribution of the

microscopic configurations is the Boltzmann one (H-theorem)[1]; at equilibrium the entropy is maximized and the second law of thermodynamic defines the irreversibility of the thermalization process. A necessary condition for thermalization is ergodicity: the time average of a certain observable taken at long times is equal to the average over the states contained in a given energy shell of the phase space. This statement is true if the system covers all the accessible area in the phase space during its evolution , as it happens for example the set of all the microstates with a given total energy. Chaos plays a fundamental role for ensuring ergodicity, as we will see in the next section.

From what we have just said two difficulties emerge in the definition of quantum thermalization: the first is that ergodicity cannot be defined, since the notion of trajectory and phase space make no sense in quantum mechanics. The second is related to irreversibility: since the system is isolated and its dynamics is unitary, it has been not clear from the early foundation of the quantum theory how equilibrium could be reached. In particular, one of the issues was how the system could loose the memory of the initial state and evolve in a state locally described by a classical superposition of states [32]. This apparent contradiction was solved by Von Neumann [68]: it opened the way to theoretical and recent experimental progresses [30, 20] which brought to the formulation of the Eigenstate Thermalization Hypothesis (ETH) [69, 70], the established conceptual setup for studying thermalization in quantum systems. We introduce it in the following (for a review see [71, 32]).

Let us consider a generic nonintegrable interacting quantum many body system with high density of states; let $\hat{H}$, E and $|E\rangle$ be the Hamiltonian, the energies and the eigenvectors respectively. Given an initial state $|\psi_0\rangle$ and a local observable $\hat{O}$ [2] the time evolution of its expectation value is:

$$\langle O\rangle(t) = \sum_{E,E'} \psi_E \psi^*_{E'} \mathrm{e}^{-i\frac{(E-E')t}{\hbar}} \langle E|\hat{O}|E'\rangle. \tag{1.1.1}$$

The coefficients $\psi_E = \langle E|\psi_0\rangle$ are the components of the initial state in the basis of the energy eigenstates. We henceforth set $\hbar = 1$ and assume that there are no degeneracies in the energy spectrum. We can distinguish two parts in the above equation, a diagonal, time independent one $\hat{O}_{diag}$ and an off diagonal one $\hat{O}_{off}(t)$:

$$O_{diag} = \sum_E |\psi_E|^2 O_{E\,E}\,, \qquad O_{off}(t) = \sum_{E\neq E'} \psi_E \psi^*_{E'} \mathrm{e}^{-i(E-E')t} O_{E'\,E}. \tag{1.1.2}$$

By considering the time average of $\langle O\rangle(t)$ at infinite times, defined as

$$\overline{\langle O\rangle} = \lim_{T\to\infty} \frac{1}{T} \int_0^T \mathrm{d}t\, \langle O\rangle(t), \tag{1.1.3}$$

we observe that the term $O_{off}(t)$ vanishes in the average if the positive series of the coefficients $\{|\psi_E|\}_E$ is convergent [72]. So we obtain

$$\overline{\langle O\rangle} \equiv O_{diag}, \tag{1.1.4}$$

[1] We restrict for simplicity to the case of the canonical ensemble, excluding the existence of other macroscopic constraints which would require the generalized Gibbs ensemble to be considered.

[2] Although there is no a precise definition of the observables to which ETH applies, they are commonly taken to have a local support [71]

which we call expectation value in the diagonal ensemble [30]. The expectation value O_{diag} depends, in principle, on the choice of the initial state, while in an ergodic system the asymptotic expectation value is independent on the initial state. In particular, if the E is the energy of the initial state, it is given by the microcanonical average

$$\langle \hat{O} \rangle_{micro}(E) = \frac{1}{\mathcal{N}_E} \sum_{E' \in [E, E+\Delta E]} \langle E'|O|E' \rangle \,, \tag{1.1.5}$$

where $\mathcal{N}_E$ is the number of eigenstates contained in the energy shell $[E, E+\Delta E]$. The Eigenstate Thermalization Hypothesis solves this apparent contradiction by stating that [73, 70]

$$\langle \hat{O} \rangle_{micro}(E) = \langle E'|\hat{O}|E' \rangle + \delta\hat{O} \qquad \forall\, E' \in [E, E+\Delta E] \tag{1.1.6}$$

with $\delta\hat{O} \sim 1/\sqrt{\dim\mathcal{H}}$. By recalling Eqs. (1.1.4) and (1.1.5) we have that

$$O_{diag} \simeq O_{E\,E} \sum_{E'} |\psi_{E'}|^2 = \langle \hat{O} \rangle_{micro}(E) \,, \tag{1.1.7}$$

which proves the equivalence between the diagonal and the microcanonical ensemble.

The ETH states that each eigenstate of the system contains a superposition of states for a certain local observable. The dynamical notion of classical ergodicity is replaced by an assumption on a static property of the quantum system, namely the structure of its eigenstates. Moreover, the superposition does not change significantly by considering another eigenstate close in energy to the previous one, justifying the equivalence between the microcanonical ensemble and the diagonal one.

The formal statement of ETH has been extended to the off diagonal elements of the operator matrix: given two eigenstates with energies E and E' sufficiently close [3] between each other we have that

$$O_{E\,E'} = \mathrm{e}^{-S(\bar{E})/2} f(\bar{E}, \omega) R_{E\,E'} \,, \tag{1.1.8}$$

where $f(\bar{E}, \omega)$ is a smooth function of $\bar{E} = (E + E')/2$ which vanishes as $\omega = E - E'$ becomes large and $R_{E\,E'}$ is a random variable with unit variance and zero average. More details about $R_{E\,E'}$ will be given by Random Matrix Theory, as we will se in the next paragraph.

1.2 From classical to quantum chaos

Many phenomena in classical physics are dubbed as chaotic: a few examples range from single particle systems, as the Sinai's billiard [74] and the double pendulum [75], or interacting systems as gravitational systems [76] and fluids [77]. These systems are examples of non-integrable systems in which chaos arises from interactions between more than two components or from non-linear equation of motions. In a chaotic system dramatic different effects are observed by starting from initial states which are *apparently* equal between each other: the apparent equality depends on the maximum precision with which a measurement can be carried out. In regular systems

[3] With non extensive difference.

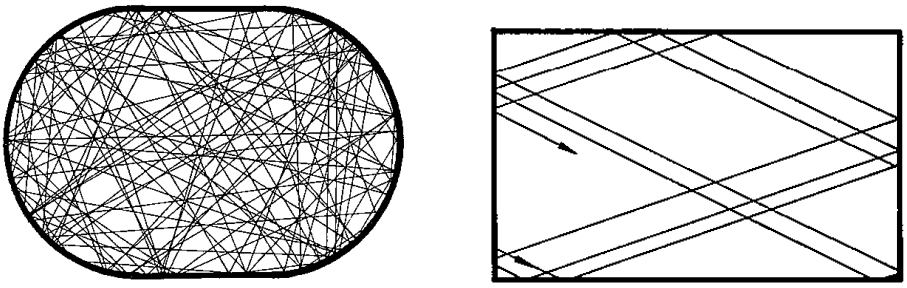

Figure 1.1: Example of a chaotic trajectories in the Sinai's billiard and regular dynamics in the rectangular billiard. The difference is entirely induced by the curve lateral walls of the billiard. Figures are taken from [78].

uncertainties smaller than this precision do not usually affect the final observations, while in chaotic systems they do influence profoundly the dynamics. In this sense the chaotic evolution of a system is often considered unpredictable due, in fact, to our ignorance of the initial state. In Figure 1.1 we show trajectories of a Sinai's billiard (left panel): in this case close initial points generate completely different trajectories. In contrast, the rectangular billiard (right panel) is regular in the sense that trajectories with close initial conditions describe similar orbits. The idea of distinguishing chaotic and regular dynamics by measuring the divergence of trajectories lead to definition of the Lyapunov exponents [79]: given a system evolving in the phase space with two trajectories ψ_t and ψ'_t whose distance in the phase space is called $\delta_t = |\psi_t - \psi'_t|$ the Lyapunov exponent [4] is defined as follows [80]:

$$\lambda = \lim_{t\to\infty} \lim_{\delta_0\to 0} \frac{1}{t} \log \frac{|\delta_t|}{|\delta_0|} \,. \tag{1.2.1}$$

The system is chaotic if λ is positive, indicating that δ_t increases exponentially in time.

An important feature of chaotic systems is that they are ergodic and allow thermalization, as we told before. For this reason, in order to understand how a quantum system can thermalize one needs to define quantum chaos and ergodicity. As we already mentioned, the problem of the absence of trajectories in quantum mechanics must be taken into account. One approach for investigating quantum chaotic behaviors consists in computed objects called Out of Time Ordered Correlators (OTOC)[81]. These quantities are introduced for measuring the return probabilities for a given initial state: instead of varying the initial state as in classical systems one of the Hamiltonian parameters [82] is slightly varied between the forward and backward time evolution: in this way a quantity equivalent to the Lyapunov exponents for a quantum system can be defined.

A different approach makes use Random Matrix Theory (RMT) [83, 84] in the definition of quantum chaos: indeed this formalism provides a mathematical setup for recognizing systems which thermalize and those that do not by focusing on the

[4] the number of Lyapunov exponents varies with the number of degrees of freedom but the definition can be easily extended. In particular the regular or chaotic behavior is determined by the largest of the Lyapunov exponents which is called maximal Lyapunov exponent.

spectral properties of the model Hamiltonian. It has initially observed that the Hamiltonian of a quantum system with a chaotic classical counterpart has the same spectral properties of a random matrix chosen from one of the Gaussian Ensembles [85][5]; in particular, the distribution of the spacings between successive eigenvalues obeys the Wigner Dyson distribution [86, 83]. The previous observation applies to generic many body nonintegrable quantum systems [87, 88, 89] as well. The level spacing distribution has been found to obey the Poisson statistics if the system is integrable [85]. The same is true for many body localized systems [90] due to the presence, also in this case, of an extensive number of local integrals of motion: in the first case it descends from the structure of the Hamiltonian while in the second it is due to a sufficiently strong disorder [39, 40]. A complete explanation for the connection between quantum chaos and RMT is still missing, apart from results valid for a single particle [91] or in the semiclassical limit [92] and a recent attempt to explain the agreement between the spectral properties of nonintegrable systems [93]; nevertheless this result is a very powerful tool to distinguish localization/delocalization transition in quantum many body non integrable systems, see for example [94].

Within this framework, the eigenstates of a chaotic Hamiltonian are random vectors whose amplitudes obey a Gaussian distribution with zero mean and variance $\sigma^2 \sim 1/\dim\mathcal{H}$ [95]. This implies that the variable $R_{E\,E'}$ in Eq. (1.1.8) is Gaussian too. We conclude that the scaling of the off diagonal elements contain information regarding the thermalization of the system, while the shape of their distribution is a signature of its ergodicity. In the next section we introduce the Floquet formalism which will allow us to define thermalization and ergodicity in periodically driven systems.

1.3 Floquet theory

1.3.1 The Floquet operator

The Hamiltonian operator is fundamental in the study of time independent systems since it allows the computation of the exact dynamics of the system [96]. Moreover, its eigenvalues and eigenstates encode useful information for classifying the dynamics of the system as it happens, for example, for many body localized systems: the ergodic and localized phases of the system can be inferred through in the spectral properties of the energy spectrum and in the structure of eigenstates [65]. The study of time dependent systems is complicated by the fact that the Hamiltonian does not commute at different times and, in principle, a spectral representation of the evolution propagator cannot be derived. In the case of periodically driven system the application one uses Floquet theory: it was introduced for the first time in 1883 [97] with the purpose of solving linear differential equations with time dependent, periodic coefficients and then it found a natural application in the context of periodically driven quantum systems [98]. The great advantage of this theory is that it allows to study periodically driven systems with techniques similar to those used in time independent ones by replacing the Hamiltonian operator with a new one, called Floquet operator [99], which we define hereafter. Unless differently specified we set $\hbar = 1$. Let $\hat{H}(t)$ be

[5]The Ensemble is the Orthogonal, Unitary or Symplectic one depending on the symmetry under time reversal transformation.

a time dependent, periodic Hamiltonian with period T:

$$\hat{H}(t+T) = \hat{H}(t) \quad \forall t. \tag{1.3.1}$$

Let us indicate a generic set of independent solutions of the corresponding Schrödinger equation with $\{|\phi_\alpha(t)\rangle\}$, where the index α runs over the Hilbert space dimension. Analogously let $\{|\phi_{\alpha'}(t+T)\rangle\}$ be the another independent set of vectors obtained from $\hat{H}(t+T)$ [100]. Due to the periodicity of the Hamiltonian there is a unitary transformation which maps the first set into the second. We define $\hat{U}_F(t)$ the unitary operator which maps the first set of vectors into the second and we indicate with $\{\mathrm{e}^{-i\mu_\alpha T}\}$ its eigenvalues. Now we consider the class of states $|\psi(t)\rangle = \sum_\alpha c_\alpha |\phi_\alpha(t)\rangle$, with normalized coefficients $\{c_\alpha\}$, such that $|\psi(t+T)\rangle = \sigma|\psi(t)\rangle$: this condition is satisfied if $|\psi(t)\rangle$ is one of the eigenstates of $\hat{U}_F(t)$ and σ is one of its eigenvalues. In general we have

$$|\psi_\alpha(t+T)\rangle = \hat{U}_F|\psi_\alpha(t)\rangle = \mathrm{e}^{-i\mu_\alpha T}|\psi_\alpha(t)\rangle. \tag{1.3.2}$$

The Floquet theorem states that the states $\{|\psi_\alpha(t+T)\rangle\}$ are solutions of the Schrödinger equation and can be written in the form:

$$|\psi_\alpha(t)\rangle = \mathrm{e}^{-i\mu_\alpha t}|\tilde{\psi}_\alpha(t)\rangle, \quad |\tilde{\psi}_\alpha(t)\rangle = |\tilde{\psi}_\alpha(t+T)\rangle. \tag{1.3.3}$$

On the other hand, the operator $\hat{U}_F(t)$ is simply the propagator $\hat{U}(t, t+T)$ over one period, defined as

$$\hat{U}(t, t+T) = \mathcal{T}\ \mathrm{e}^{-i\int_t^{t+T}\hat{H}(t')\mathrm{d}t'}, \tag{1.3.4}$$

with $\mathcal{T}$ indicating that the ordered product is taken in the exponential. It is easy to see that, due to the periodicity of $\hat{H}(t)$, $U_F(t)$ does not change if it is computed at different times $t' = nt$ with n integer.

The unitary propagator over one period $\hat{U}_F$ is called the Floquet operator and its eigenstates $|\psi_\alpha\rangle$ are the Floquet eigenstates [98, 101]. The quantities μ_α deduced from the eigenvalues of $\hat{U}_F$ are the Floquet quasienergies: note that they are defined up to integer multiples of the quantity $2\pi/T$. Since $\hat{U}_F$ is a unitary operator it can be seen as the exponentiation of an Hermitian operator: such operator is the Floquet Hamiltonian, defined such that

$$\hat{U}_F = \mathrm{e}^{-\frac{i}{\hbar}\hat{H}_F T}. \tag{1.3.5}$$

A remark is needed. The definition of $\hat{U}_F$ contains an ambiguity in the choice of the initial time for the computation of the propagator. This arbitrariness has been associated to the freedom one has in the definition of a gauge field [2]: choosing the initial time of the propagator $\hat{U}_F$ fixes the so called Floquet gauge. We can change it by taking the unitary propagator $\hat{W}$ over an interval of time smaller than T and defining the shifted Floquet operator $\hat{\tilde{U}}_f = \hat{W}^\dagger \hat{U}_F \hat{W}$. Accordingly we have $|\tilde{\psi}_\alpha\rangle = \hat{W}^\dagger|\tilde{\phi}_\alpha\rangle$. The eigenstates change during this transformation, but the quasienergies are left invariant:

$$\begin{aligned} \hat{\tilde{U}}_f|\tilde{\psi}_\alpha\rangle &= \hat{W}^\dagger \hat{U}_F \hat{W}\, \hat{W}^\dagger|\tilde{\phi}_\alpha\rangle \\ &= \hat{W}^\dagger\, \hat{U}_F\ |\phi_\alpha\rangle \\ &= \hat{W}^\dagger\, \mathrm{e}^{-i\mu_\alpha}\ |\phi_\alpha\rangle = \mathrm{e}^{-i\mu_\alpha}|\tilde{\psi}_\alpha\rangle \end{aligned} \tag{1.3.6}$$

As we will see, this ambiguity can be exploited for making some symmetry of the system more explicit.

By diagonalizing the Floquet operator we can compute the stroboscopic dynamics of a periodically driven system at times which are integer multiple of the period T. Indeed, given an initial state $|\psi(0)\rangle$ we have

$$\begin{aligned} |\psi(nT)\rangle \equiv |\psi(n)\rangle &= \hat{U}(nT,0)|\psi_0\rangle \\ &= [\hat{U}_F]^n|\psi(0)\rangle = \sum_\alpha \mathrm{e}^{-i\mu_\alpha nT} c_\alpha |\psi_\alpha\rangle, \end{aligned} \tag{1.3.7}$$

with $c_\alpha = \langle\psi_\alpha|\psi(0)\rangle$ and n integer. In the same way given an observable $\hat{O}$ its evolution is given by

$$\langle\hat{O}(n)\rangle = \sum_{\alpha\,\beta} c_\alpha c_\beta * \mathrm{e}^{-i(\mu_\alpha-\mu_\beta)nT} O_{\alpha\,\beta}, \tag{1.3.8}$$

with $\hat{O}_{\alpha\,\beta} = \langle\alpha|\hat{O}|\beta\rangle$. In the next paragraph we show how dynamical localization / delocalization can be inferred from the Floquet eigenstates.

1.3.2 Inverse participation ratio

The IPR is a quantity which is used to understand if a state of a quantum system is localized or not with respect to a certain local basis of the Hilbert state [102]. In this paragraph we define it by starting from the limiting case of a perfectly delocalized state; the definition applies both with or without a driving.

Let us consider the motion of a particle on a d-dimensional support with linear size L and let $\psi(\mathbf{r})$ be its normalized wave function. The state is said to be delocalized if the probability amplitude is uniformly distributed along all the support: due to normalization it follows that

$$|\psi(\mathbf{r})|^2 \sim 1/L^d. \tag{1.3.9}$$

We now introduce the q_{th}-order moments of the distribution $|\psi(\mathbf{r})|^2$ [103]defined as:

$$\mathcal{I}_\psi(q) = \int_{L^d} \mathrm{d}\mathbf{r}\, |\psi(\mathbf{r})|^{2q}. \tag{1.3.10}$$

The underscore should remind to the reader that the quantity depends on the state we are considering. The first moment $\mathcal{I}_\psi(1)$ is identically equal to the unity due to normalization. The second moment $\mathcal{I}_\psi(2)$ defines instead the IPR_ψ of the state described by the wave function $\psi(\mathbf{r})$:

$$\mathrm{IPR}_\psi := \mathcal{I}_\psi(2) = \int_{L^d} \mathrm{d}\mathbf{r}\, |\psi(\mathbf{r})|^4. \tag{1.3.11}$$

It follows from Eqs. (1.3.9) and (1.3.11) that for a delocalized state $\mathrm{IPR}_\psi \sim 1/L^d$; the following general relation holds:

$$\mathcal{I}_\psi(q) \sim 1/L^{d(q-1)} \equiv 1/\dim(\mathcal{H})^{(q-1)}, \tag{1.3.12}$$

where $\mathcal{H}$ is the system's Hilbert space. This means that for a delocalized state all the moments $\mathcal{I}(q)$ scale as a power law with the Hilbert space dimension with the exponent given by Eq. (1.3.12).

Now we consider a localized state, namely a state whose wave function $\psi_\ell(\mathbf{r})$ has a finite support Ω contained in L^d. The IPR now scales with the size of the system or

$$\mathrm{IPR}_{\psi_\ell} \sim \mathcal{I}_\psi(q) \sim const \ \forall q \in \mathbb{N}\,, \tag{1.3.13}$$

provided that the linear size is larger than Ω. The limiting case of a localized state is the one whose wave function is a Dirac Delta, meaning that the state lies on a single state in the chosen local basis of $\mathcal{H}$. In this case $\mathcal{I}_{\psi_\ell}(q) = 1.0$ independently on q. In real computations, states whose wave functions are exponentially decaying in some local basis are said to be localized, as it happens for the Hamiltonian eigenstates of systems exhibiting Anderson localization. In these cases one expects the IPR to be independent on the size of the system if L is larger than the characteristic localization length.

So far we have derived the behavior of the IPR in two limiting cases, namely a perfectly delocalized or a localized state: in fact there are cases in which the IPR satisfies anomalous intermediate scaling laws. In this case the state is said to exhibit multifractal properties [103] and it is necessary to study higher moments for a proper characterization of its states. Such behavior has been found for example at the the critical point of the Anderson transition [104, 105] or in the Quantum Hall effect[106, 107]. In these cases indeed the momenta $\mathcal{I}(q)$ satisfy a modified version of Eq. (1.3.12) which reads

$$\mathcal{I}_\psi(q) \sim 1/\dim(\mathcal{H})^{D_q(q-1)}, \tag{1.3.14}$$

where D_q, satisfying $0 < D_q < 1$, is the fractal dimension associated to the $q-$th momentum.

In the following we want to understand if the dynamics of a periodically driven system is localized or not. In order to do this we will focus on the localization properties of the Floquet eigenstates. For this purpose we define IPR as the average of the inverse participation ratios IPR_α relative to the Floquet eigenstates $|\psi_\alpha\rangle$:

$$\mathrm{IPR} := \frac{1}{\mathcal{N}}\sum_\alpha \mathrm{IPR}_\alpha = \frac{1}{\mathcal{N}}\sum_{\alpha,\mathbf{m}} |\langle \mathbf{m}|\psi_\alpha\rangle|^4. \tag{1.3.15}$$

At this point two remarks are needed. The first is that, if the system were time independent, we would have sampled the Hamiltonian eigenstates from a small energy interval with an approximately uniform density of states. In a periodically driven system the situation is different since the quasienergies stay in the interval $[-\pi, \pi]$ and the density of states is uniform: it follows that we can consider all the eigenstates for the computation of the average. Most importantly there are strong fluctuations which involve different orders of magnitude between the IPRs of different eigenstates the dynamics may be dominated by some rare events and do not attain with the scaling of the averaged IPR. We check the role played by the fluctuations of the IPR by computing the probability distribution $P(\mathrm{IPR}_\alpha)$ and checking the shape of the tails. Power law, slow decaying tails reveal the presence of non negligible rare values of the IPR_αs and indicate that the averaged IPR is not able to describe the dynamics of the system.

Another possibility is to take the log average of the IPR_αs defined as follows:

$$\mathrm{IPR}_{log} = \exp\langle \ln \mathrm{IPR}_\alpha \rangle\,, \tag{1.3.16}$$

where $\langle\cdot\rangle$ stands for the average taken over the Floquet eigenstates ensemble. The equation above is an operative definition the geometric mean of the IPR_α: in the following it will be referred as log -average, or logarithmic average or geometric one as well. The log-average of a set of data is always smaller than the linear one and the distance between the two increases with the amount of fluctuations. It follows that if the values of the IPR and IPR_{log} are close, then the averaged IPR is a good indicator for investigating the dynamics of the system. In practical computation we are interested in the scaling of the IPR with the local truncation M: we ask how robust the scaling fit is against fluctuations and how representative is it for describing the dynamics of the system. To get an answer we fit both the linear averaged IPR and the log one and then check if the two fits are compatible within the errorbars. If the answer is positive then the fitting parameters are reliable and they contain meaningful information for the description of the system. Otherwise there are rare events in the distribution of the IPR_αs which affect the behavior of the system and the linear algebra is not enough for capturing its dynamics and a more deep analysis is needed.

1.3.3 Thermalization and quantum chaos in periodically driven systems

The formalism illustrated above has been extended to the case of periodically driven systems. A generic non-integrable quantum system is expected to heat unbounded in time under a periodic driving. This is formalized by saying that the Floquet eigenstates are associated to infinite-temperature states and, from a microncanonical point of view, they belong to the same energy shell. It has been found [44] that systems which heat up to the infinite temperature state have a Floquet operator whose distribution of spacings between the quasi energies obey the Wigner Dyson distribution, while it is Poisson if the system is in a dynamically localized phase. Given a nonintegrable interacting periodically driven systems with Hamiltonian $\hat{H}(t)$ and Floquet eigenstates $|\psi_\alpha\rangle$ the infinite temperature state is defined by the following density matrix

$$\rho(T\to\infty) = \frac{1}{\mathcal{N}}\sum_\alpha |\psi_\alpha\rangle\langle\psi_\alpha| \,. \tag{1.3.17}$$

This is called the uniform ensemble and comprehends all the eigenstates due to the reason we explained above. It follows that the microcanonical average of a given observable $\hat{O}$ reduces to

$$\overline{\langle O\rangle} = \frac{1}{\mathcal{N}}\sum_\alpha O_{\alpha\,\alpha} \tag{1.3.18}$$

with $O_{\alpha\,\alpha} = \langle\psi_\alpha|O|\psi_\alpha\rangle$. A periodically driven system satisfies the ETH if $\overline{\langle O\rangle}$ coincides with the expectation value obtained from the diagonal ensemble

$$O_{diag} = \sum_\alpha |\psi_\alpha|^2 O_{\alpha\,\alpha}. \tag{1.3.19}$$

We suppose in the previous equation to start from an initial state ψ_0 and we call $\psi_\alpha = \langle\psi_\alpha|\psi_0\rangle$. The expression is analogous to the one in Eq. (1.1.2) but the Hamiltonian eigenstates have been replaced by the Floquet ones.

Finally, let us remark that the function $f(\bar{E}, \omega)$ defined in Eq. (1.1.8) is replaced by a constant factor in the definition of ETH for a periodically driven system [6] : it follows that all the elements should be considered in the computation of the distribution.

Nevertheless we will study the distributions of the off diagonal elements of some relevant observable in order to investigate the dynamics at long but not asymptotic times. For this reason, we will be interested only in those elements $O_{\alpha\,\beta}$ such that the difference $|\mu_\alpha - \mu_\beta|$ is sufficiently small. Now we define the level spacing distribution and the average spacing ratio which uses spectral properties of the Floquet operator for distinguishing dynamical localization from ergodicity

Level spacing distribution. We consider the quasienergies μ_α listed in increasing order and define the spacings as

$$\lambda_\alpha = \mu_{\alpha+1} - \mu_\alpha, \tag{1.3.20}$$

with $1 \leqslant \alpha \leqslant D-1$, where D is the dimension of the relevant subspace of the Hilbert space. We compute the probability distribution $P(s)$ of the variable

$$s = \rho(\mu_\alpha)\lambda_\alpha, \tag{1.3.21}$$

where λ_α is the spacing above defined and ρ_α is the density of states of the quasi energies. From a computational point of view the interval $[-\pi, \pi]$ is divided in N_{bin} bins with length $\mathrm{d}\mu$, then the density of states is computed as

$$\rho_i = \frac{\#_i(\mu_\alpha)}{D\,\mathrm{d}\mu}, \quad 1 \leqslant i \leqslant N_{bin}, \tag{1.3.22}$$

where $\#_i(\mu_\alpha)$ is the number of quasi energies in the $i-$th interval of length $\mathrm{d}\mu$. Then $\rho(\mu_\alpha)$ is the density of states in the interval containing μ_α.

Averaged level spacing ratio. The averaged level spacing ratio is

$$\langle r \rangle = \frac{1}{D-2} \sum_{\alpha=1}^{D-2} \frac{\min\{\lambda_\alpha, \lambda_{\alpha+1}\}}{\max\{\lambda_\alpha, \lambda_{\alpha+1}\}}. \tag{1.3.23}$$

The computation of $\langle r \rangle$ is a practical way to recognize the distribution of the level spacings: if the distribution is Poisson then $\langle r \rangle \sim 0.386$, if the distribution is Wigner Dyson instead $\langle r \rangle \sim 0.530$. In the next section we introduce the model on which our analysis is focused.

[6] The reason is due to the so-called eigenstate mixing [43].

Chapter 2

Coupled quantum kicked rotors model

In this chapter we introduce the core model for this thesis. In the first section we review the known results concerning the classical and quantum kicked rotor. In the second section we define the coupled quantum kicked rotor model; finally we define the observables that we study in the computation of the exact time evolution of the system.

2.1 The kicked rotor model

The Hamiltonian for the classical KR is

$$H(t) = \frac{1}{2I}p^2 + K\cos\theta \sum_{n=-\infty}^{+\infty} \delta(t - Tn) \tag{2.1.1}$$

in which I is the inertia momentum of the rotor and T the period of the kick. We rewrite the Hamiltonian Eq. (2.1.1) in units of I/T^2, defining the following adimensional quantities: $t' = t/T$, $K' = T\,K/I$, $p' = p\,T/I$ [84]. After this rescaling, the kicking period is 1 and we recall al the quantities without the $'$. We will henceforth be interested in the stroboscopic evolution of the system at each period of time: we consider the state of the system only at discrete times $t_n \equiv n$. Without the kick the system is trivially integrable and its trajectories correspond to straight lines or isolated points in the phase space. By adding a small kick $K \ll 1$ the system is quasi integrable: according to the KAM theorem [108, 109] the orbits are deformed and become quasi periodic but they are confined in regular regions of the phase space delimited by the so called KAM tori. As a consequence the energy of the system still remains bounded in time, resulting in the so called classical dynamical localization. In this regime the phase space still appears covered by regular trajectories (top left, panel in Figure 2.1). As K is increased, reaching the critical value $K \simeq K_c = 0.971635$ (upper panels from left to right) chaotic regions emerge in the phase space, but they are separated from the regular ones by some of the KAM tori which are still present: in this regime there is a coexistence of regular trajectories, characterized by dynamical localization, and chaotic ones. This phenomenon disappears as the kick amplitude

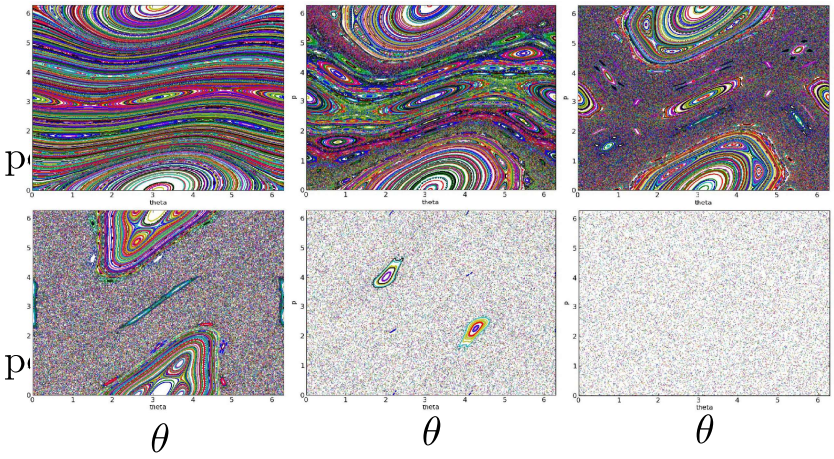

Figure 2.1: Poincaré section for the classical kicked rotor. Upper panels (from left to right): $K = 0.5, 0.971635, 1.3$. Lower panels: $K = 2.1, 5.0, 10.0$. Figure taken from [110].

becomes much larger than K_c: the regular parts of the phase space disappear and the dynamics is chaotic almost everywhere in the phase space.

Due to the absence of energy conservation they are not confined in a given energy shell but cover all the phase space. Moreover the evolution of the trajectory in the phase space can be assumed to be characterized by uncorrelated shifts occurring at each kick. Therefore we can describe the evolution of the kicked rotor as a diffusive process in the phase space. Assuming that the initial state is the zero angular momentum one, we focus on its stroboscopic evolution at integer times $t \equiv n$. We measure the spreading of the trajectory in the momentum space by evaluating the variance $\sigma_p^2(n)$ immediately before the n-th kick: it grows linearly since the process is diffusive. Now we observe that $\sigma_p^2(n) \equiv \overline{p^2(n)} = 2E(n)$[1] (the average $\overline{(\cdot)}$ is taken over an ensemble of randomly chosen initial conditions): the diffusive spread of the trajectory in the phase space coincide with a linear growth of the kinetic energy of the kicked rotor. The growth rate is $D_{KR} \simeq K^2/4$ and it can be derived by assuming that, due to ergodicity, the time autocorrelators of the trajectories vanishes. This is a simple case in which we can prove that a periodically driven classical system heats up linearly in time. In the following we describe the behavior of the quantum kicked rotor.

The quantum counterpart of this model (quantum kicked rotor – QKR) is obtained by imposing the commutation rules

$$[\hat{\theta}, \hat{p}] = i\bar{k}, \qquad \bar{k} = \hbar T/I. \tag{2.1.2}$$

Quantum mechanics dramatically changes the behavior of this model. The dynamics is no longer ergodic, indeed the kinetic energy, after a linear growth up to a time n^* [95, 61], reaches an asymptotic condition and fluctuates around a finite value [2].

[1] The dynamics preserves the symmetry $p \to -p$, therefore if we choose all the initial conditions of the ensemble such that $p(0) = 0$ we have $\overline{p}(n) = 0 \; \forall \, n$ and then $\sigma_p^2(n) \equiv \overline{p^2(n)}$.

[2] This phenomenon is observed for every value of K but $\bar{k}$ incommensurate with π since differently quantum resonances occur and kinetic energy $E(n)$ grows quadratically in time.

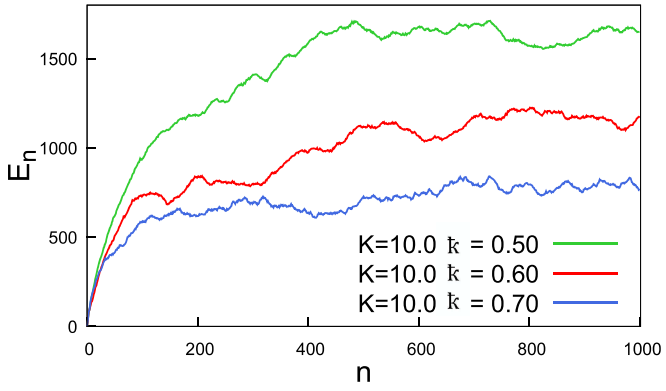

Figure 2.2: Energy saturation at a fixed value of K and different values of $\hbar$

Remarkably, this quantum dynamical localization is independent on K, although the saturation values of the kinetic energy depends on it. Dynamical localization in the kicked rotor can be explained via a mapping, introduced for the first time in [60, 61]. We consider the Floquet operator for this model:

$$\hat{U}_{KR} = \mathrm{e}^{-i\frac{\hat{p}^2}{2}}\mathrm{e}^{-iK\cos\hat{\theta}} \tag{2.1.3}$$

and we indicate with ϕ_α its eigenstates and with $\{\nu_\alpha\}$ its quasienergies. The mapping shows that the Floquet eigenstates equation, written in the angular momentum representation of the Hilbert space, is equivalent to the Schrödinger equation for a time independent model: in particular, a single particle hopping on a disordered one dimensional lattice. The particle undergoes Anderson localization [37] and the eigenstates are exponentially localized in the real space of the particle: the eigenfunction of a given eigenstate with energy ϵ is in the form $\psi_\epsilon(x) \sim \mathrm{e}^{-x/\xi}$, where ξ is the localization length. The mapping transforms the real space of the particle into the angular momentum space of the kicked rotor. As a consequence the Floquet eigenstates are localized in the angular momentum space in the same way as the Hamiltonian eigenfunctions of the lattice model are localized in space. It follows that an initial state of the kicked rotor will involve during its dynamics a finite number of Floquet eigenstates: their support in the angular momentum space is bounded since they are localized and as a consequence the kinetic energy cannot grow beyond a certain limit. The time n^* can be estimated with an heuristic argument [111]. Suppose that N_ψ is the number of Floquet eigenstates involved in the evolution of the initial state ψ: the averaged spacing among the quasienergies is therefore $\delta \sim 1/N_\psi$ and therefore for $n < n^* = 1/\delta \sim N_\psi$ the system will evolve as its classical counterpart. The number of states N_ψ can be estimated by assuming that it is proportional to the spread of the initial state in the momentum space $\Delta p(n)$: we have $N_\psi \sim \Delta p(n^*)$. But due to diffusion $\Delta p(n^*) \sim \sqrt{Dn^*}$, with $D = (K/\hbar)^2/2$. We finally obtain $n^* \sim 1/\hbar^2$. In Figure 2.2 different kinetic energy trajectories are plotted as a function of the stroboscopic time n. Note that the time n^* increases as $\hbar$ diminishes.

Dynamical localization has been experimentally observed for the first time with a cloud of ultracold atoms moving in a pulsed, one dimensional periodic optical lattice [112] but it has been object of several successive experiments [113]: the kicked rotor model has been used in studies about the quantum-to-classical transition, thanks

to the sharp difference which distinguish its behavior in the two different limits. In particular, some work focused on the enhancement of diffusion [114], on testing the robustness of its resonances via some noise [115]; in other the decoherence process [116] via photons scattering is investigated [117]. This interest reveals how rich is the spectrum of phenomena which can be observed in this model. In the next section we introduce the interacting version of the QKR model, which is the object of our investigation.

2.2 Coupled quantum kicked rotors model

The dynamics of L rotors is described by the following Hamiltonian:

$$\hat{H}(t) = \hat{H}_0 + \sum_{n=-\infty}^{+\infty} \delta(t-n)\hat{V}(\boldsymbol{\theta})\,, \tag{2.2.1}$$

with a time independent kinetic term and an angle-dependent kick

$$\hat{H}_0 = \sum_{j=1}^{L} \frac{\hat{p}_j^2}{2}\,, \qquad \hat{V}(\boldsymbol{\theta}) = \sum_{j=1}^{L} \Big[K\cos\hat{\theta}_j + J\cos(\hat{\theta}_j - \hat{\theta}_{j+1}) \Big]\,. \tag{2.2.2}$$

We impose periodic boundary conditions, $\hat{\theta}_{L+1} \equiv \hat{\theta}_1$ and we impose the canonical commutation relations to the angle and angular momentum operators, namely $[\hat{\theta}_j, \hat{p}_k] = i\hbar\,\delta_{j\,k}$ and $[\hat{p}_j, \hat{p}_k] = [\hat{\theta}_j, \hat{\theta}_k] = 0$. The effective Planck's constant is the same defined in Eq. (2.1.2)

The model describes the dynamics of a collection of single quantum rotors subject to a kicked interaction of strength J which couples nearest neighbor rotors and a term of strength K which kicks them separately one by one; since the interaction is contained into the kicked part of the Hamiltonian, then two terms of the Hamiltonian, $\hat{H}_0$ and $\hat{V}(\boldsymbol{\theta})$, are diagonal in the angular momentum and angle representation, respectively. Let us briefly recall that the classical counterpart of the model (2.2.1) with $L > 1$ has been studied in the past [118, 119] as an example of a many particle system whose dynamics is chaotic, and recently reconsidered in the works focusing of classical prethermalization phenomena [120, 121]. It has been shown that if the amplitude of the perturbation which breaks the integrability, namely the periodic driving, is small, then the system persists on quasi periodic trajectories for exponentially long times [122]; nevertheless the dynamics finally becomes chaotic and the system starts evolving diffusively in the phase space. From the point of view of the energy absorption the chaotic dynamics causes a linear growth of the kinetic energy (see Appendix A). We will show in the next chapter that the dynamics of the quantum system presents a dramatically different behavior: indeed it is characterized by a localized phase in which the energy does not grow in time and by a delocalized one in which the heating mechanism has the shape of a power law in a region of the parameters space.

Previous works about coupled kicked rotors concerned the two rotors problem, both from a theoretical and an experimental point of view [62, 123, 124, 125, 126]. Other works focused instead on the three body problem [127, 128, 129] but by means of a single rotor model with a quasi periodic kick obtained with a number of incommensurate frequencies: it has been found that such a model reproduces the dynamics

of a system with a number of rotors equal to the number of frequencies; moreover, this model has been mapped onto a time independent disordered hopping problem in which the Anderson localization transition was expected. Due to the experimental feasibility of the quasiperiodic kicked model it has been possible [130] to realized the Anderson localization transition in three dimension by using ultracold atoms in a pulsed optical lattice.

In a series of recent works [131, 124] a chain of kicked rotors with linear kinetic term in the Hamiltonian has been considered for the study of many body dynamical localization. In this case the transition is induced by commensurability/incommensurability of the rotor velocities: when incommensurate between each other an extensive set of integral of motion can be found and the system is dynamically localized exactly like an integrable one. We are instead interested in a model of coupled rotors and quadratic kinetic term: despite not being exactly solvable, unlike the linear case, this model will allow us to investigate how the addition of the interaction alters the localized dynamics of the nonlinear single quantum kicked rotor.

The Hilbert space in which the system evolves is

$$\mathcal{H} = \bigotimes_{j=1}^{L} \mathcal{H}_j \,, \tag{2.2.3}$$

where $\mathcal{H}_j$ is the Hilbert space of a single rotor. In the following we will indicate the basis vectors relative to the angle representation with $|\boldsymbol{\theta}\rangle = |\theta_1, \dots \theta_L\rangle$. As for the single kicked rotor, given a state $|\psi\rangle$ its wave function in the angle representation $\psi(\boldsymbol{\theta}) = \langle\boldsymbol{\theta}|\psi\rangle$ must be 2π-periodic for each angle variable θ_j: it follows that each angular momentum operator can be written as $\hat{p}_j = \hbar\,\hat{m}_j$, where $\hat{m}_j$ is a number operator whose spectrum is $\mathbb{Z}$. We indicate the basis vectors relative to the number operators representation with $|\mathbf{m}\rangle = |m_1, \dots m_L\rangle$ and hereafter we will refer to it as the angular momentum, or simply momentum, representation.

A first remark must be devoted to the dimension of the Hilbert space of the many rotor system, which is $\mathcal{N}_\infty = \mathbb{Z}^L$. In order to perform numerical simulations it is necessary to artificially truncate the local Hilbert space, considering only local angular momentum eigenstates with $m_j = -m_{max}, \dots, m_{max}$ at each site j. We define $M = 2\,m_{max} + 1$ and so we restrict the system to live in a subspace of the whole Hilbert space whose dimension is $\mathcal{N} = M^L$.

The second remark concerns the symmetries of the Hamiltonian: the first is the global momentum parity, which is associated to the following couple of transformations:

$$\hat{p}_j \to -\hat{p}_j \,, \quad \hat{\theta}_j \to -\hat{\theta}_j \qquad \forall j. \tag{2.2.4}$$

Two other symmetry transformations [3] are related to the spatial uniformity of the Hamiltonian combined to the choice of periodic boundary conditions: they are the spatial translations and inversion defined respectively by the transformations

$$\begin{aligned} &\hat{\theta}_j \to \hat{\theta}_{j+\ell} \qquad \ell < L \quad \forall j \,, \\ &\hat{\theta}_j \to \hat{\theta}_{L-j} \qquad \forall j. \end{aligned} \tag{2.2.6}$$

[3] One more symmetry is present in the case with $K = 0$ where the rotors evolve only via the interaction term which conserves the total angular momentum $\hat{P} = \sum_j \hat{p}_j$. Indeed, given a momentum

The symmetries defined in Eqs. (2.2.7), (2.2.6) allow us to write the Hamiltonian matrix in a block-diagonal form and divide the Hilbert space in sectors which do not mix during the dynamics, if the initial state is chosen from one of those subspaces. The last symmetry built into this system is the time reversal, whose associated transformation is

$$\begin{aligned} t &\to -t \\ \hat{p}_j &\to -\hat{p}_j\,, \qquad \forall j. \end{aligned} \tag{2.2.7}$$

The importance of this symmetry will be clear after the definition of the Floquet operator $\hat{U}_F$ which is, according to Eq. (1.3.4):

$$\hat{U}_F = \exp\left(-\frac{i}{\hbar}\hat{H}_0\right)\exp\left(-\frac{i}{\hbar}V(\hat{\boldsymbol{\theta}})\right)\,. \tag{2.2.8}$$

We indicate with $|\phi_\alpha\rangle$ the Floquet eigenstates which satisfy the eigenvalue equation

$$\hat{U}_F\,|\phi_\alpha\rangle = \mathrm{e}^{-i\mu_\alpha}\,|\phi_\alpha\rangle\,, \tag{2.2.9}$$

where μ_α are the Floquet quasienergies. By using the ambiguity discussed in section 1.3.1 we rewrite the Floquet operator in a form which results convenient for diagonalizing it thanks to the presence of the time reversal symmetry. Let us start by unitarily transforming the Floquet operator as follows:

$$\hat{U}_F \to \mathrm{e}^{i\hat{H}_0/(2\hbar)}\,\hat{U}_F\,\mathrm{e}^{-i\hat{H}_0/(2\hbar)} = \mathrm{e}^{-i\hat{H}_0/(2\hbar)}\mathrm{e}^{-iV(\hat{\boldsymbol{\theta}})/\hbar}\mathrm{e}^{-i\hat{H}_0/(2\hbar)} \equiv \hat{\tilde{U}}_f. \tag{2.2.10}$$

The Floquet eigenstates accordingly transform in $|\phi_\alpha\rangle \to |\tilde{\phi}_\alpha\rangle = \exp(i\hat{H}_0/(2/\hbar))\,|\phi_\alpha\rangle$ while the eigenvalues of $\hat{U}_F$ are left invariant, as we shown in Eq. 1.3.6. Therefore the localization structure of the Floquet states in the momentum basis does not change, since the operator $\hat{H}_0$ is diagonal in this basis. We neglect the $\tilde{\cdot}$ to indicate the Floquet eigenstates and the Floquet operator hereafter.

In this new definition the Floquet operator is described by a symmetric complex matrix and therefore the following hermitian operators are described by real symmetric matrices: they are

$$\sin\hat{U}_F = \frac{\hat{U}_F - \hat{U}_F^\dagger}{2i}\,, \quad \cos\hat{U}_F = \frac{\hat{U}_F + \hat{U}_F^\dagger}{2}. \tag{2.2.11}$$

These two operators have the same eigenvectors and the eigenvalues are $\sin\mu_\alpha$ and $\cos\mu_\alpha$, respectively: in this way we can compute the Floquet eigenstates as real vectors and the quasienergies by diagonalizing two real matrices instead of two complex ones.

---

eigenstate $|\mathbf{m}\rangle$, the coupling term which involves the sites j and $j+1$ acts in the following way:

$$\begin{aligned} \cos(\hat{\theta}_j - \hat{\theta}_{j+1})|\mathbf{m}\rangle &= \frac{\mathrm{e}^{i(\hat{\theta}_j - \hat{\theta}_{j+1})} + \mathrm{h.\,c.}}{2}|\mathbf{m}\rangle \\ &= \frac{|..., m_j+1, m_{j+1}-1, ...\rangle + |..., m_j-1, m_{j+1}+1, ...\rangle}{2}\,. \end{aligned} \tag{2.2.5}$$

In this case the symmetry operation is given by the projector, diagonal in the angular momentum representation, on a subspace with a fixed total angular momentum. This symmetry will not be considered in this work although it may be an interesting prosecution.

The investigation tools we have introduced in the previous section require the exact diagonalization of the Floquet operator with the computation of the full quasienergies spectrum. In this process the symmetries and the Floquet gauge we have introduced above play an important role since they can be used to reduce the dimension of the Hilbert space to an effective smaller one and allow us to consider larger values of the local truncation M in our numerical computations. In Appendix B we show that we can reduce the dimension of the effective Hilbert space by a factor of $4L$ by implementing the parity and spatial symmetries defined in Eqs. (2.2.7) and (2.2.6).

In the next paragraph we will discuss the information we can get from the study of the exact evolution of the system.

2.3 Exact dynamics and energy absorption

The study of the evolution of the system, and in particular of its heating in time, is useful for understanding whether the system is localized or not at infinite times as well as for investigating its transient dynamics.

In our periodically driven system it is convenient to define the infinite temperature state $\rho(T=\infty)$ introduced in Eq. (1.3.17) as the mixed state in which the eigenstates of the kinetic term of the Hamiltonian $\hat{H}_0$ are all occupied with equal probability. Since $\hat{H}_0$ is diagonal in the momentum eigenstates basis we have that [4]

$$\rho(T=\infty) = \frac{1}{\mathcal{N}} \sum_{\mathbf{m}} |\mathbf{m}\rangle\langle\mathbf{m}|. \tag{2.3.1}$$

Note that this state satisfies translational invariance and it is spatially uniform. Starting from $\rho(T=\infty)$ the infinite temperature kinetic energy $E(T=\infty)$ can be defined:

$$E(T=\infty) = \langle \hat{H}_0 \rangle_{\rho(T=\infty)} = \frac{k^2}{2\,\mathcal{N}} \sum_{\mathbf{m}} |\mathbf{m}|^2 \,. \tag{2.3.2}$$

It will be useful in the following to understand the behavior of $E(T=\infty)$ as the local truncation value M is increased; in order to do this we first note that due to translational invariance we can define a local, space – averaged infinite temperature state [5]

$$\rho_s(T=\infty) = \frac{1}{M} \sum_{m=-m_{max}}^{m_{max}} |m\rangle\langle m| \,, \tag{2.3.3}$$

where the underscore s indicates that the state refers to a single rotor. Now it is possible introduce the infinite temperature energy per rotor

$$E_s(T=\infty) = E(T=\infty)/L = \frac{k^2}{2\,M} \sum_{m=-m_{max}}^{m_{max}} m^2 \,, \tag{2.3.4}$$

and observe that $E_s(T=\infty) \sim M^2$.

[4] This definition of the infinite temperature state is equivalent to the one given in Eq. (1.3.17) since the two states are proportional to the identity matrix.

[5] By defining the projector operator on the momentum eigenstate m $\hat{O}_m = 1/L \sum_{j=1}^{L} (\otimes_{l\neq j} \mathbf{1}_l |m_j\rangle\langle m_j|)$ it follows $\rho_s(T=\infty)_{m\,m} = \mathrm{Tr}[\hat{O}_m\, \rho(T=\infty)]$.

In the following we will use $E_s(T=\infty)$ to understand if the asymptotic state of a system is ergodic or not. Indeed, we can compare the averaged infinite temperature energy with the energy averaged at infinite times

$$E_{av}(t\to\infty)=\sum_{\alpha}E_{\alpha}|\langle\phi_{\alpha}|\psi_0\rangle|^2\,, \tag{2.3.5}$$

where $|\psi_0\rangle$ is the initial state we are considering and $E_{\alpha}=\hbar^2/2\sum_{\mathbf{m}}\mathbf{m}^2|\langle\mathbf{m}|\phi_{\alpha}\rangle|^2$. Note that $E_{av}(t\to\infty)$ is a quantity which in principle depends on the choice of the initial state. Nevertheless this is not the case if the system thermalizes to $\rho(T=\infty)$ defined in Eq. (2.3.3) due to the periodic driving, loosing any memory of the initial state.

We expect that if the evolution starts from a state with an initial energy which is less than $E(T=\infty)$ and the dynamics is not ergodic the energy $E_{av}(t\to\infty)$ will saturate at a finite asymptotic value; moreover, this value will be independent from the local truncation, provided that M is larger than a certain value. Differently, in case of ergodic dynamics the system will reach an asymptotic value which will depend on the local truncation M.

This statement can be quantified by defining the ratio $I(M)$ as follows:

$$I(M)=\frac{E_{av}(t\to\infty)}{E(T=\infty)}\,. \tag{2.3.6}$$

The dynamical behavior of the system can be inferred from $I(M)$ as follows: if the system exhibits dynamical localization $I(M)$ will decrease as $M\to\infty$, since the infinite time energy is independent from M while on the other hand $E(T=\infty)$ is not. In particular, since we know how $E(T=\infty)$ scales with M we expect

$$I(M)\sim M^{-2} \tag{2.3.7}$$

for a localized state. On the other side if the dynamics is ergodic and the system heats unbounded we expect $E_{av}(t\to\infty)$ to grow up to $E(T=\infty)$ or at least to an asymptotic value which scales as $E(T=\infty)$ with M:

$$I(M)\sim O(1)\,. \tag{2.3.8}$$

Finally, we point out that considering the exact dynamics of the system provides information about the heating process of the system: for example consider the time evolution of the kinetic energy of the system computed as the expectation value of the operator $\hat{H}_0$ on the state $|\psi(t)\rangle$ or, more precisely, given an initial state $|\psi_0\rangle$, the stroboscopic dynamics at integer times n. The time evolved state will be

$$|\psi(n)\rangle=(\hat{U}_F)^n|\psi_0\rangle \tag{2.3.9}$$

and accordingly we will consider the energy per rotor

$$E(n)=\frac{\langle\psi(n)|\hat{H}_0|\psi(n)\rangle}{\hbar^2\,L}, \tag{2.3.10}$$

which corresponds to take the expectation value of the number operators $\hat{m}_j$ instead of $\hat{p}_j$. It is fundamental to remark that any feature of the heating process can be assumed to be physical only if it persists by computing the dynamics with different values of the local truncation M. This will be particularly important in the analysis of the delocalized region in which we will discuss the power law growing of the energy $E(n)$ and we will show that it is independent on the truncation.

Chapter 3

Dynamical localization and subdiffusion with $L = 3$

In this Chapter we present the results concerning a system of $L = 3$ coupled kicked rotors. In the first section we present a mapping, taken from [63], between our system and a particle moving in a $L-$dimensional, disordered lattice undergoing the Anderson localization transition. This mapping provides an analytical explanation for the phases which emerge in the dynamics of our system and is described in the rest of the Chapter. In the second section we present the two main phases which can be observed in the dynamics of the system, namely one characterized by dynamical localization and another in which the system heats up continuously in time. In the fourth section we describe a modified version of the model in which the translational invariance is broken by applying a non uniform kick to the rotors. This new model allows us to check whether spatial localization phenomena can be generated and how they are related to the dynamical one. We conclude with a summary of the results presented in the Chapter.

3.1 Mapping onto a time independent disordered lattice model

As we have shown in the previous chapter, the single kicked rotor model can be mapped in a time independent model describing a particle hopping in a one dimensional disordered lattice [60, 61, 132]: the real space in which the particle moves corresponds to the Hilbert space of the rotor in the angular momentum representation. Since it is known that a particle hopping a 1D disordered lattice always undergoes Anderson localization [37, 133], this argument allows to predict the dynamical localization typical of the single kicked rotor: the localization in angular momentum space implies that the kinetic energy absorbed by the rotor is bounded and therefore the system cannot heat up to the infinite temperature state.

In this paragraph we show that this argument can be extended to the case of L coupled rotors: the number of rotors L fixes the dimensionality of the lattice and the space in which the particle moves corresponds to the rotors Hilbert space in the angular momentum representation, as in the single rotor model. In the following we will first build the mapping between the two models and then we will numerically

study the properties of the time independent one. It is known that the motion of a particle in a L-dimensional disordered lattice undergoes the Anderson localization transition [38] if the disorder is sufficiently high and the hopping is short ranged. In our lattice model we cannot change the amplitude of the disorder but, as we will see, we can modify its hopping properties. We will show that our model can admit a localized phase by looking at the hopping coefficients: we verify that they have a short range since this is indeed a necessary condition for a localized phase. For increasing values of the parameters the range of the hopping increases, suggesting the passage to the delocalized phase. According to this observations we expect that the periodically driven model with L should admit a dynamically localized phase for small kick parameters and a delocalized regime as $K/\hbar$ and $J/\hbar$ are increased. We will analyze both the cases $L = 2$ and $L = 3$ to show that in both cases the hopping has a short range and that in the first case the increasing of the range is slower: this may be related to the fact that in two dimensions the systems is expected to always be localized, with a localization length exponentially large in the hopping range [62].

In order to build up the mapping of our model onto an Anderson one let us start from the Floquet operator defined in Eq. (2.2.10). We start from the following pair of equations:

$$\mathrm{e}^{\mp i\hat{H}_0/(2\hbar)}\mathrm{e}^{\mp i\,V(\hat{\boldsymbol{\theta}})/\hbar}\mathrm{e}^{\mp i\hat{H}_0/(2\hbar)}\,|\phi_\alpha\rangle = \mathrm{e}^{\mp i\mu_\alpha}\,|\phi_\alpha\rangle\,. \tag{3.1.1}$$

By using the resolution of the identity

$$\mathbf{1} = \sum_{\mathbf{m}'} \big|\mathbf{m}'\big\rangle\big\langle\mathbf{m}'\big| \tag{3.1.2}$$

we write the sum of Eqs. (3.1.1) in the basis of local momentum eigenstates and we can finally rewrite the Floquet eigenvalues equation as

$$\sum_{\mathbf{m}'\neq\mathbf{m}} W_{\mathbf{m}\,\mathbf{m}'}\,\big\langle\mathbf{m}'\big|\,\phi_\alpha\big\rangle + \epsilon(\mathbf{m})\,\langle\mathbf{m}|\,\phi_\alpha\rangle = 2\cos(\mu_\alpha)\,\langle\mathbf{m}|\,\phi_\alpha\rangle\,, \tag{3.1.3}$$

with

$$W_{\mathbf{m}\,\mathbf{m}'} = 2\mathrm{Re}\left[\mathrm{e}^{-i(\varphi(\mathbf{m}')+\varphi(\mathbf{m}))}\int\frac{\mathrm{d}^L\boldsymbol{\theta}}{(2\pi)^L}\mathrm{e}^{-iV(\boldsymbol{\theta})/\hbar}\mathrm{e}^{-i(\mathbf{m}'-\mathbf{m})\cdot\boldsymbol{\theta}}\right], \tag{3.1.4}$$

and

$$\epsilon(\mathbf{m}) = 2\mathrm{Re}\left[\mathrm{e}^{-2i\varphi(\mathbf{m})}\int\frac{\mathrm{d}^L\boldsymbol{\theta}}{(2\pi)^L}\mathrm{e}^{-iV(\boldsymbol{\theta})/\hbar}\right];\quad \varphi(\mathbf{m}) = \frac{\hbar}{4}\sum_{i=1}^{L} m_i^2\,. \tag{3.1.5}$$

Equation (3.1.3) can be interpreted as the Schrödinger equation of a particle hopping in an L-dimensional potential $\varepsilon(\mathbf{m}) = W_{\mathbf{m}\,\mathbf{m}}$. $\varepsilon(\mathbf{m})$ is a quasi random disordered potential which is responsible for inducing localization in a one-dimensional next-nearest-neighbor tight-binding model. A quasi random disorder has been proven to be sufficient for inducing Anderson localization in a three dimensional lattice [134] and observed experimentally in the one dimensional case [135]. Moreover, the same universality class has been observed in the localization–delocalization transition of an effective three kicked rotors model [136]. The only remark regards the choice of $\hbar$ which must be different from 4π: in this case the potential $\varepsilon(\mathbf{m})$ is constant and cannot

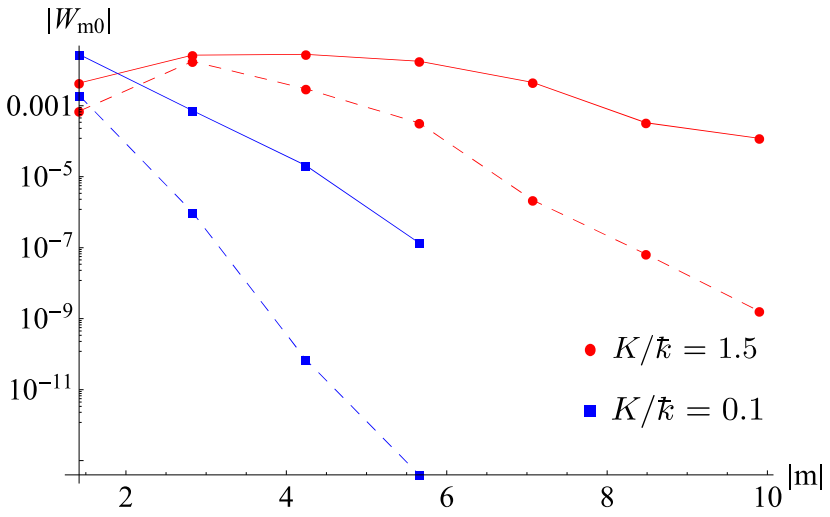

Figure 3.1: The modulus of $W_{\mathbf{m}\,\mathbf{0}}$ is plotted as a function of $|\mathbf{m}|$ for $K/\hbar = 0.1$ (blue squares) and $K/\hbar = 1.5$ (red circles) for $L = 3$. We set $J = K$. The continuous and dashed lines correspond to two orthogonal directions in $\mathbf{m}$ space. We see the slope of the exponential decaying which decreases as $K/\hbar$ is increased; an analogous behavior is found with $L = 2$.

induce any localization. Our mapping is different from the one introduced in Refs. [60, 61] for the single kicked rotor: in our case the hopping does not show unphysical divergences which instead occur in Refs. [60, 61] due to the small convergence radius of the Fourier series of the tangent. Our wave-function $\langle \mathbf{m}' | \, \phi_\alpha \rangle$ is normalized by construction and there is no risk of spurious unphysical divergences in the hopping because the integrand in Eq. (3.1.4) is always bounded in absolute value. In the single-rotor ($L = 1$) case, the hopping is

$$W_{m\,m'} = 2J_{m'-m}\left(\frac{K}{\hbar}\right)\mathrm{Re}[i^{m'-m}\mathrm{e}^{i(\varphi(m)+\varphi(m'))}] \tag{3.1.6}$$

where $J_{m'-m}$ is the Bessel function of order $m'-m$. The modulus of this expression always decays faster than exponentially [137] with $m'-m$ and never shows unphysical divergences. We have therefore a one-dimensional Anderson model which is always localized [37].

Now we go through the analysis of the hopping coefficients $W_{\mathbf{m}\,\mathbf{m}'}$ for $L > 1$. We observe that, although they depend on $\mathbf{m}$ and $\mathbf{m}'$ separately, they are symmetric under the parity transformation $(\mathbf{m}, \mathbf{m}') \to (-\mathbf{m}, -\mathbf{m}')$ and permutations of the Cartesian components of $\mathbf{m} - \mathbf{m}'$ (namely, $\mathbf{m}$ and $\mathbf{m}'$ undergo the same permutation of the components). Also, the $W_{\mathbf{m}\,\mathbf{m}'}$ depend on the direction given by the vector $\mathbf{m} - \mathbf{m}'$.

In order to apply existing results on the Anderson model to the case $L > 1$ we need to verify that the hopping is short ranged, as it is for $L = 1$. The exact analytical expression for $W_{\mathbf{m}\,\mathbf{m}'}$ cannot be established, nevertheless we can infer information on how this hopping coefficient decays with $|\mathbf{m} - \mathbf{m}'|$ by observing that $W_{\mathbf{m}\,\mathbf{m}'}$ is the linear combination of real and imaginary part of the Fourier transform of $f(\theta) = \mathrm{e}^{-\mathbf{i}\mathbf{V}(\boldsymbol{\theta})/\mathbf{k}}$. Since the function $f(\theta)$ is $\mathcal{C}(\infty)$ and it is 2π-periodic in all the θ_j, its Fourier

components $\hat{f}(\mathbf{m}' - \mathbf{m})$ decay exponentially fast with $|\mathbf{m}' - \mathbf{m}|$. It means that the hopping $W_{\mathbf{m}\,\mathbf{m}'}$ is short ranged and therefore the results concerning the Anderson model can always be applied to the effective hopping model Eq. (3.1.3).

In the following we numerically show the decaying properties of the hopping coefficients for $L = 2$ and $L = 3$. In Figure 3.1 we set $\mathbf{m}' = 0$ and plot the behavior of the hopping coefficients $|W_{\mathbf{m}\,\mathbf{0}}|$ as a function of the distance $|\mathbf{m}|$ for $K/\hbar = 0.1$ and $K/\hbar = 1.5$; $\mathbf{m}$ are taken along two orthogonal directions (dashed and continuous lines in Figure 3.1). The exponential decay clearly appears and is slower for increasing values of $K/\hbar$. This behavior is the same along the two directions even if the values of $|W_{\mathbf{m}\,\mathbf{0}}|$ are different due to the space anisotropy.

In order to quantify the strength of the hopping we introduce two quantities: the first is the hopping integral Σ

$$\Sigma = \sum_{\mathbf{m}\in\mathbb{Z}^L} |W_{\mathbf{m}\,\mathbf{0}}|. \tag{3.1.7}$$

For a short ranged lattice we expect this quantity to be finite at fixed $K/\hbar$, and to diverge if the hopping is long ranged. The second is the hopping range, defined as

$$\rho = \frac{\sum_{\mathbf{m}\in\mathbb{Z}^L} |W_{\mathbf{m}\,\mathbf{0}}|\,|\mathbf{m}|}{\Sigma}. \tag{3.1.8}$$

We say that the hopping strength of the lattice model increases when the hopping integral and the hopping range increase. We first verify that the hopping in the lattice Eq. (3.1.3) is short ranged and therefore well defined. In addition the hopping strength, estimated through the hopping integral and range (see Equations (3.1.7) and (3.1.8)) is found to be monotonously increasing as a function of $K/\hbar$.

Let us discuss the numerical computation leading to these results (in the rest of the discussion $\hbar = 400$ and $J = K$ for definiteness).

The exponential decay of the hopping strength makes the hopping integral defined in Eq. (3.1.7) finite: we compute it by taking the asymptotic value $\Sigma \equiv \lim_{M\to\infty} \Sigma_M$ of

$$\Sigma_M = \sum_{\mathbf{m}\in\mathcal{C}(M)} |W_{\mathbf{m}\,\mathbf{0}}|\,, \quad M \in \mathbb{N} \tag{3.1.9}$$

where $\mathcal{C}(M)$ is the $N-$dimensional cube with edge length $2M$ centered in $\mathbf{0}$. The hopping integral is plotted in Figure 3.2 as a function of $K/\hbar$ for $L = 2$ and $L = 3$. The inset shows some examples of convergence of Σ_M for increasing values of M, for some values of $K/\hbar$ and $L = 3$. In the case $L = 2$ the behavior is the same, except that higher values of M have to be considered to achieve the convergence (the limitation on the value of M is connected to limiting the error in the computation of $W_{\mathbf{m}}$ up to a certain $\mathbf{m}$ to $\sim 10\%$). In a similar way we compute the hopping range defined in Eq. (3.1.8) to find that it is finite: we consider the series

$$\rho_M = \frac{\sum_{\mathbf{m}\in\mathcal{C}(M)} |W_{\mathbf{m}\,\mathbf{0}}|\,|\mathbf{m}|}{\Sigma_M}\,, \quad M \in \mathbb{N} \tag{3.1.10}$$

and check its convergence as M is increased. In Figure 3.3 ρ is plotted as a function of $K/\hbar$ for $L = 2$ and $L = 3$. The inset shows also in this case the convergence of ρ as a function of M for some values of $K/\hbar$.

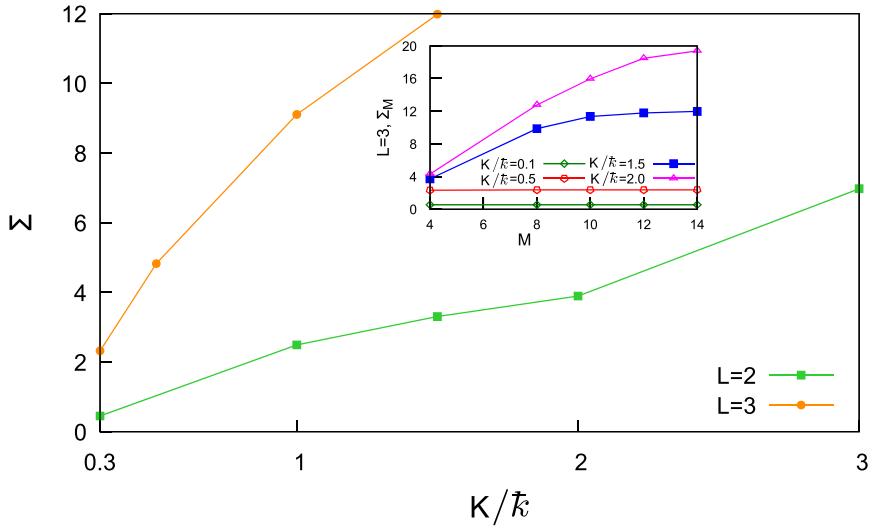

Figure 3.2: The hopping integral Σ vs. $K/\hbar$ is plotted for $K = 2$ (green squares) and $L = 3$ (orange circles). At fixed L there exists a maximum value of M for which the integrals $W_{\mathbf{m}}$ can be computed: this imposes a limit to the maximum value of $K/\hbar$ for which Σ can be computed. This is shown in the inset for $L = 3$; since for $L = 3$ the maximum value is $M = 14$, then the convergence of ρ_M can be observed only up to $K/\hbar = 2.0$. For the $L = 2$ case the maximum value is $M = 40$. The resulting hopping integral Σ is a monotonically increasing function of $K/\hbar$ as shown in the main figure.

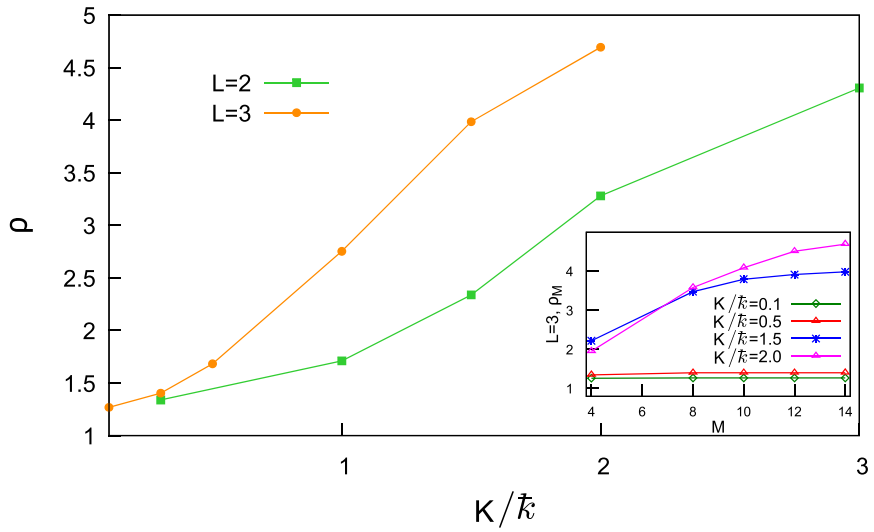

Figure 3.3: The hopping range ρ vs. $K/\hbar$ for $L = 2$ (green squares) and $L = 3$ (orange circles): it grows as $K/\hbar$ is increased. As for the computation of Σ, in the the numerical computation of $W_{\mathbf{m}}$ we have a maximum $M = 14$ for $L = 3$ implying that the convergence of ρ is observed only for $K/\hbar \leqslant 2.0$ (see inset). For the case $L = 2$ the interaction range is plotted up to $K/\hbar = 3.0$ where convergence is observed with $M = 36$. Notice that also in this case ρ is an increasing function of $K/\hbar$.

In conclusion, we have provided an analytical argument to state that the lattice model is short ranged. Moreover, we have numerically checked this property in the interval of $K/\hbar$ we have access to, finding also that the hopping strength (i.e. both Σ and ρ) increases with $K/\hbar$. Therefore we can apply the general theory on Anderson localization [37, 62] and we predict that for $L = 3$ our model will undergo a localization/delocalization transition at some value of $(K/\hbar)_c(L)$. In the next sections we will go through the analysis of the two dnamical regimes in parameters space, namely the localized and the delocalized one. We will use the average level spacings ratio, the IPR and the exact dynamics of the system to understand different facets of the phenomenon.

3.2 The dynamical localization - delocalization transition with $L = 3$

In this section we show that different dynamical behaviors can be observed in the dynamics our model with a finite number of rotors $L \geqslant 3$. According to the mapping between the driven coupled L-rotors chain and a disordered L-dimensional lattice there are two expected phases: a dynamically localized and a delocalized one.

We will show the presence of these two different phases in the case with $L = 3$ and we will discuss the intermediate one between them. The reason for choosing L=3 is merely due to computational reasons: since each site is characterized by a discrete, unbounded Hilbert space a truncation is needed and by choosing a small L we can access larger values of the local truncation M. In the next chapter we will go through the study of cases with larger L in order to catch the dynamical features which characterize the system in the thermodynamic limit.

We start our discussion by analyzing how the dynamics of the system changes by fixing the value of the interaction $J/\hbar$ and varying $K/\hbar$. We arbitrarily set $\hbar = 5.0$ in the rest of this Chapter. In Figure 3.4 the behavior of the averaged ratio $\langle r \rangle$ is plotted as a function of $K/\hbar$ at the fixed value $J/\hbar = 0.3$. Two phases can be distinguished: in the first, for $K/\hbar \lesssim 0.5$, we have $\langle r \rangle \simeq 0.386$, which is the expected value for a Poisson level spacing distribution. In the second phase, with $K/\hbar \gtrsim 2.0$, one finds that $\langle r \rangle \simeq 0.536$, which is the Wigner Dyson value, as expected in case of ergodic dynamics. Notice that $\langle r \rangle$ in the delocalized region assumes, on the average, a value smaller than the expected one. This difference is due to finite size effects: the observed value is close to $\langle r \rangle \simeq 0.527$, namely the one expected from the Circular Orthogonal Ensemble (COE) of symmetric unitary matrices, to which our Floquet operator belongs. The values of $\langle r \rangle$ expected from the COE and the GOE coincide in the thermodynamic limit [42]. In the following we analyze the regions in which dynamical localization - delocalization is expected according to Figure 3.4, by using the inverse participation ratio and the exact dynamics. The intermediate region is due to finite size effects originated from the truncation; we cannot see it, but according to the mapping we expect them to disappear at higher values of M. In Appendix F we describe this crossover region, showing that the dynamics of the system depends on the choice of the initial state in the angular momentum representation.

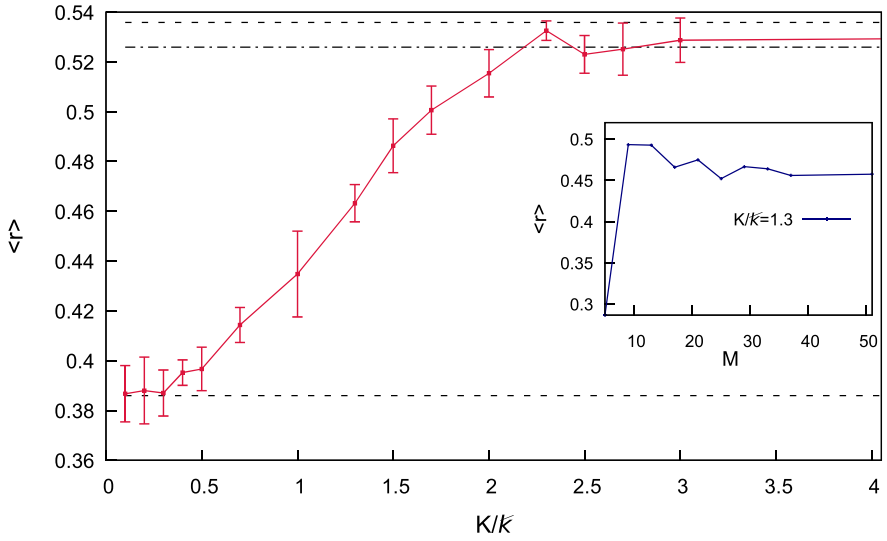

Figure 3.4: The behavior of the average ratio $\langle r \rangle$ vs $K/\bar{k}$ for $J/\bar{k} = 0.30$. The errorbars are obtained by averaging over the values corresponding to different values of M, once convergence is achieved. The top (bottom) dashed line indicates the expected value of $\langle r \rangle$ in the case of ergodicity (localization). The dot-dashed line represents the expected value for $\langle r \rangle$ from the COE. In the box we plot $\langle r \rangle$ as a function of M for an arbitrary chosen value of $K/\bar{k} = 1.3$: the intermediate value of $\langle r \rangle$ is stationary in the accessible range of values of M. Other parameters: $L = 3$, $\bar{k} = 5.0$.

3.2.1 The localized phase

We start the analysis of the localized region by looking at the behavior of the IPR as defined in Eq. (1.3.15). The behavior of the IPR for some values of $K/\bar{k}$ with $J/\bar{k} = 0.3$, such that the system is in the localized region, is shown in Figure 3.5. The IPR is constant for M larger than a threshold value which changes with $K/\bar{k}$, as expected; this implies that the dynamics of a given initial state will be localized in momentum space. As a consequence, we expect its kinetic energy to grow until it reaches a finite saturation value. We can check this by computing the growth of the kinetic energy during the evolution of an initial state with different values of the local truncation M. If the different curves collapse one on each other it means that the localization we observe is not a fictitious effect but it is a true property of the system. As an example we have computed the growth of the kinetic energy per rotor with $K/\bar{k} = 0.2$ and $J/\bar{k} = 0.3$ in the localized region. The initial state that we have chosen is the angular momentum eigenstate $|\mathbf{0}\rangle = |m_1 = 0, ..., m_L = 0\rangle$; the result is plotted in Figure 3.6, with the kinetic energy expressed in units of $\bar{k}^2$. The expectation value of the kinetic energy is plotted for $M = 29$ (circular dots) and $M = 51$ (continuous line). The two curves perfectly collapse on each other, confirming that the dynamical localization we observe is a true physical effect.

An equivalent result is obtained by looking at the ratio $I(M)$ defined in Eq. (2.3.6): indeed we expect, as discussed before, that $I(M)$ scales as M^{-2} if the state is localized while it is independent from M for a delocalized state. In this way we distinguish two regions in the kick parameters space which are relevant for recognizing the localized

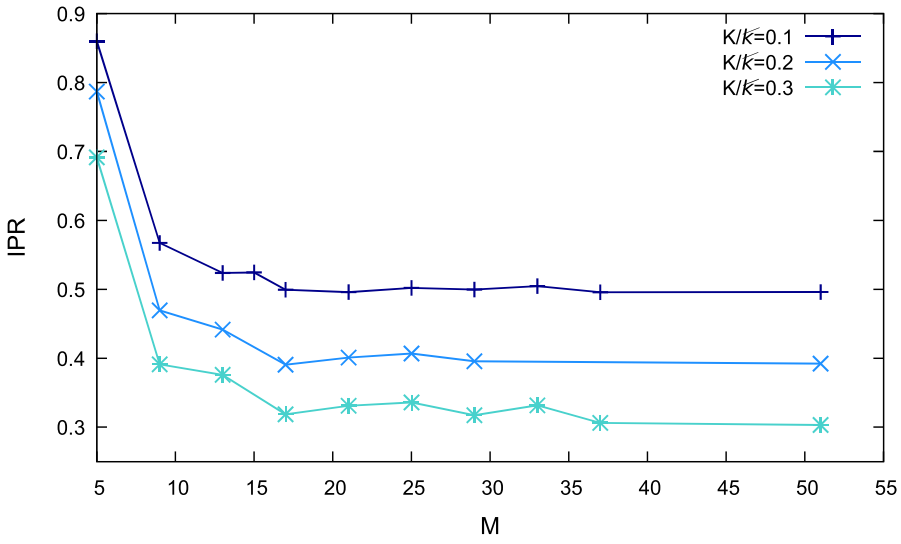

Figure 3.5: The behavior of the average IPR vs M is plotted for $J/\hbar = 0.3$ and $K/\hbar = 0.1, 0.2\,0.3$. For this values the system is localized and the IPR does not decrease as we increase the local Hilbert space truncation. Other parameters: $L = 3$, $\hbar = 5.0$.

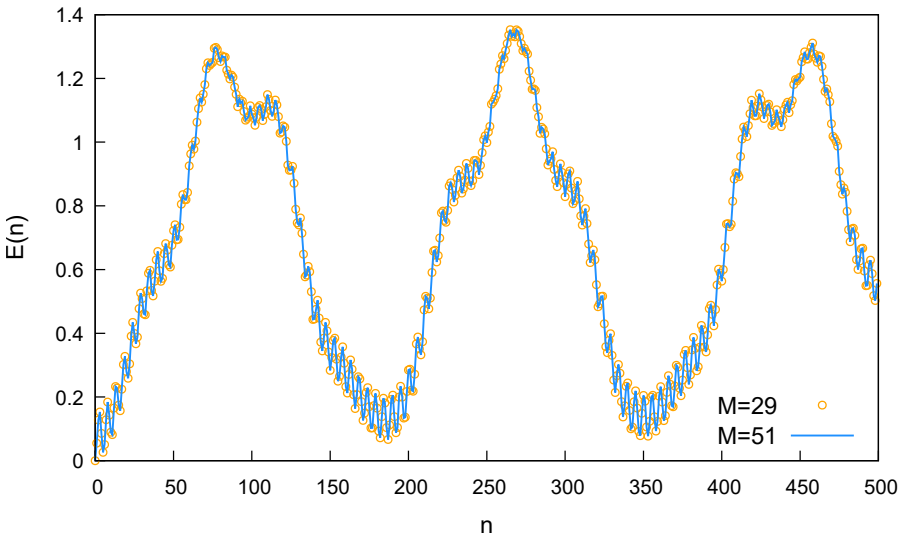

Figure 3.6: Evolution of the expectation value of the kinetic energy per rotor (in units of $\hbar^2$) with $K/\hbar = 0.2$, $J/\hbar = 0.3$. The two curves obtained with different local truncation values coincide, showing that the behavior of $E(n)$ is independent on M. Other parameters: $L = 3$, $\hbar = 5.0$.

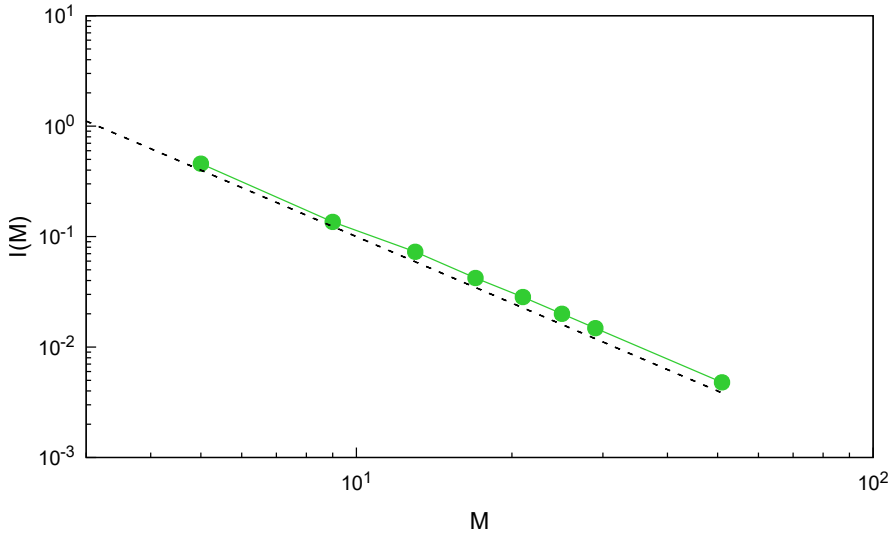

Figure 3.7: The ratio $I(M)$ is plotted as a function of M for $K/\hbar = 0.4$ and $J/\hbar = 0.3$ in the log-log scale. The points follow a power law with slope $\alpha = -1.94 \pm 0.016$ while the dashed curve has the expected slope -2.Other parameters: $L = 3$, $\hbar = 5.0$.

phase: the first one in which $I(M) \sim M^{-2}$ corresponding to dynamical localization. In the second $I(M)$ decreases but the slope in the log-log plane is not definite: in this case the system may be localized even if we cannot state it. In Figure 3.7 the scaling of $I(M)$ with M is plotted for $K/\hbar = 0.2$ and $J/\hbar = 0.3$ to show that the slope of the line is $\alpha = -1.94 \pm 0.016$, close to the expected one.

By looking again at Figure 3.5 we observe that the asymptotic value of the IPR decreases as $K/\hbar$ is increased. The quantity 1/IPR counts the localized states or, equivalently, the extension of their support in the Hilbert space: we conclude that the higher $K/\hbar$ the larger is the localization length of the Floquet eigenstates. Also the observation that the truncation value M at which the convergence of the IPR is reached increases with $K/\hbar$ leads to the same conclusion. This result is in agreement with the increase of the hopping range with $K/\hbar$ found by analyzing the hopping coefficients $W_{\mathbf{m}\,\mathbf{m}'}$ in the disordered lattice model.

3.2.2 The delocalized phase

While most of the early literature regarding many-body localization has focused more on the localized phase, recent theoretical works focused on the ergodic phase [138] pointing out the existence of anomalous thermalization phenomena [139, 64]; at the same time, new experiments have been realized to confirm the predictions of the Eigenstate Thermalization Hypothesis [31].

In this paragraph we discuss the properties of our system in the region in which the averaged ratio of the level spacing $\langle r \rangle$ is close to the Wigner Dyson value r_{WD}. We will first show the border of this region in the $J/\hbar - K/\hbar$ plane; then we will study the properties of the eigenstates, showing that they have a multifractal structure. Finally we will focus on the dynamics of the system: we will show the results concerning the heating process, which is remarkably characterized by a power-law growth of the

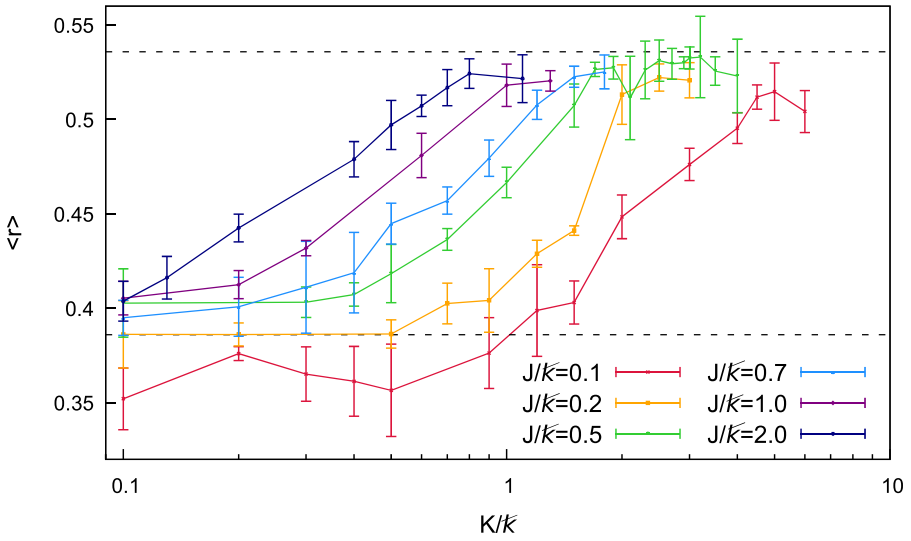

Figure 3.8: The behavior of the average ratio $\langle r \rangle$ against $K/\hbar$ for different values of $J/\hbar$. The errorbars are obtained by averaging over the values obtained with different values of M, once convergence was achieved. In this plot the maximum value of M which has been used is $M_{max} = 39$. Other parameters: $L = 3$, $\hbar = 5.0$.

kinetic energy, and the asymptotic state in terms of the infinite-time averaged kinetic energy defined in Eq. (2.3.5).

In Figure 3.8 we plot $\langle r \rangle$ as a function of $K/\hbar$ for some values of $J/\hbar$ to show that for each curve there is a value of $K/\hbar$ at which $\langle r \rangle$ reaches a plateau close to r_{WD} (upper dashed line). The values of $\langle r \rangle$ are obtained by averaging over several values of M once convergence has been achieved and the errorbars have been computed as the square root of the variances. By extracting the critical values of $K/\hbar$ for several values of $J/\hbar$ we obtain the line which separate the delocalized region from the intermediate one, represented in Figure 3.9. Please note that $J/\hbar$ scales slowly as a function of $K/\hbar$, so for each $K/\hbar$ we have considered there is a small but finite value of $J/\hbar$ separating a localized region from a delocalized one. This is expected because for $J = 0$ the system is equivalent to a single kicked rotor and it is dynamically localized for all the values of $K/\hbar$.

Now we focus on the structure of the eigenstates by studying the average inverse participation ratio IPR. The scaling of the IPR with the local truncation M in the delocalized phase is shown in Figure 3.10 for $J/\hbar = 0.3$ and $K/\hbar = 2.50$, 3.0, 10.0. It satisfies the relation

$$\text{IPR} \sim 1/\dim\mathcal{H}^{\delta_2}\,, \tag{3.2.1}$$

with $\delta_2 < 1$ and increases in modulus with $K/\hbar$ (recall that $\dim\mathcal{H} = M^L/(4L)$). As discussed in the previous section the inverse participation ratio of a perfectly delocalized state is expected to scale as $1/\dim\mathcal{H}$ independently from the Hamiltonian parameters. If instead the IPR scales as $1/\dim\mathcal{H}^{D_2}$, with $D_2 < 1$, the state has a multifractal structure (see Eq. (1.3.14)). Since we find $\delta_2 < 1$ in the averaged IPR, we suppose that the Floquet eigenstates have a multifractal structure. Their fractal dimension D_2 coincides with δ_2 if the scaling of the average IPR is representative of

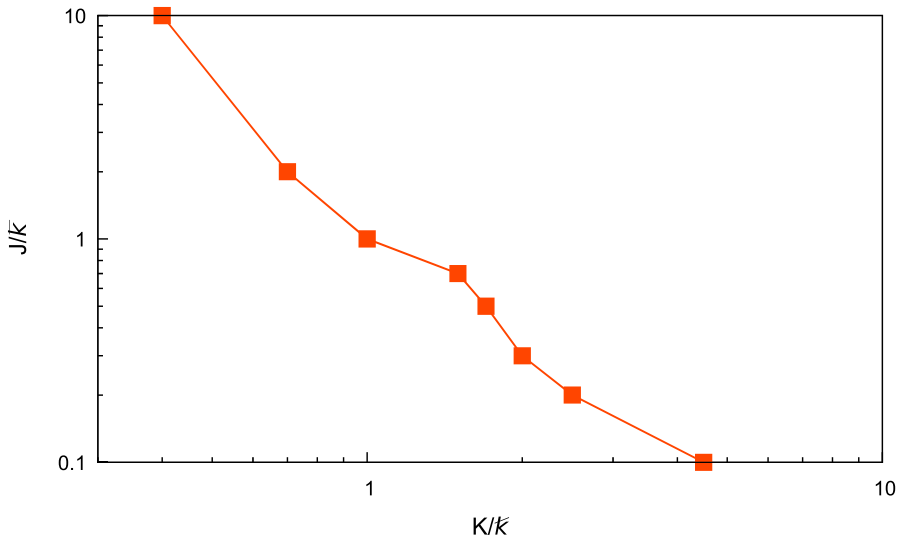

Figure 3.9: This plot represents the boundary between the intermediate and the delocalized region in the $K/\hbar - J/\hbar$ plane. It has been obtained by finding the values of $K/\hbar$ in which $\langle r \rangle$ reaches a plateau for different values of $J/\hbar$. A slow decaying of the critical value of $J/\hbar$ for which the ergodic region starts is expected since in the limit of $J \to 0$ the system is localized for all the values of $K/\hbar$. The maximum value of M which has been used is $M = 39$. Other parameters: $L = 3$, $\hbar = 5.0$.

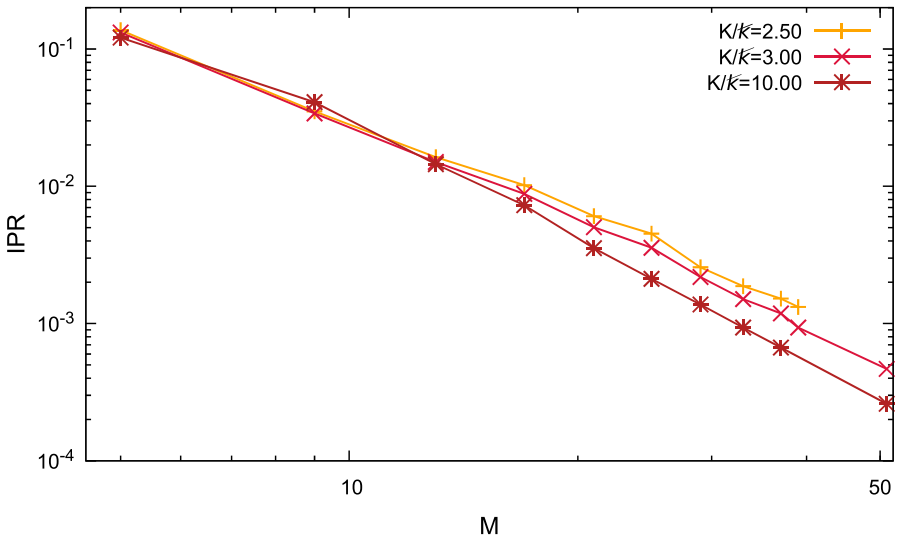

Figure 3.10: The behavior of the average IPR vs M is plotted for $J/\hbar = 0.3$ and $K/\hbar = 2.5, 3.0, 10.0$ (from lighter to darker colors). For this values the system is delocalized and the IPR scales as a power law with the dimension of the Hilbert space. Other parameters: $L = 3$, $\hbar = 5.0$.

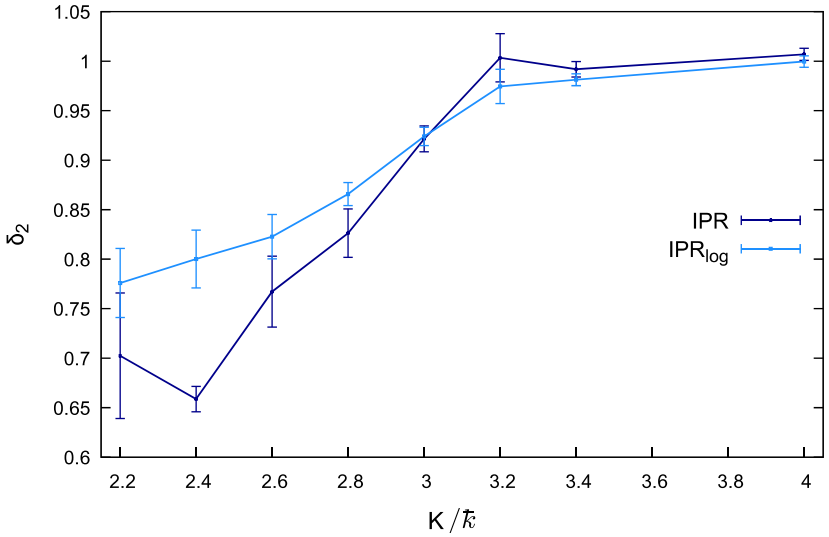

Figure 3.11: The exponent δ_2 vs $K/\hbar$ is plotted for $J/\hbar = 0.3$. It passes from a value less then one to one when $K/\hbar \lesssim 3.0$ The linear and the log averages are close (apart) when fluctuations are small (large). Other parameters:$M = 51$, $L = 3$, $\hbar = 5.0$.

the scaling of the inverse participation ratio of the single eigenstates, namely if the fluctuations are negligible. In order to investigate this possibility we first measure the scaling exponent δ_2 defined in Eq. (3.2.1). We set $J/\hbar = 0.30$ and choose $K/\hbar$ from an interval in the delocalized region. In order to study the fluctuations in the distribution of the IPR_α we compute the coefficient δ_2 by using both the linear average of the inverse participation ratios and the log-average IPR_{log} defined in Eq. (1.3.16). We consider the fluctuations negligible if the coefficients we obtain are consistent with each other within the errrorbars. The results are plotted in Figure 3.11: for small values of $K/\hbar$ the two curves are apart within each other with respect to the errorbars, while they get closer as $K/\hbar$ is increased. This means that we cannot estimate the value of D_2 through δ_2, but nevertheless we find that the eigenstates have a fractal dimension D_2 smaller than one for small values of $K/\hbar$ which tends to unit as $K/\hbar$ for larger values.

The reduction of fluctuations appears as well by looking at the distribution of the IPR_α of the single Floquet states. In panel (a) of Figure 3.12 we plot the probability distributions for increasing values of $K/\hbar$ taken in the delocalized region and $J/\hbar = 0.3$. The distributions have a power-law tail whose amplitude decrease as we increase $K/\hbar$, leading to the observed reduction of fluctuations. In panels (b) and (c) we show the distributions of the IPR_α [1] in a case in which $\delta_2 < 1$, with $K/\hbar = 2.6$, $J/\hbar = 0.3$, and $\delta_2 = 1$, with $K/\hbar = 2.0$, $J/\hbar = 2.0$, respectively. The peaks of the distributions moves to lower order of magnitude as M is increased and their positions scale as power law with M: in panel (d) we plot the scaling of peaks' positions vs M together with the corresponding average M. This corresponds to the increasing of the scaling exponent of the IPR.

We finally show the multifractality of the Floquet eigenstates by computing the

[1]We computed the distributions of the logarithms of the IPR_α in order to enhance the visibility of the distribution in the log scale along the x axis.

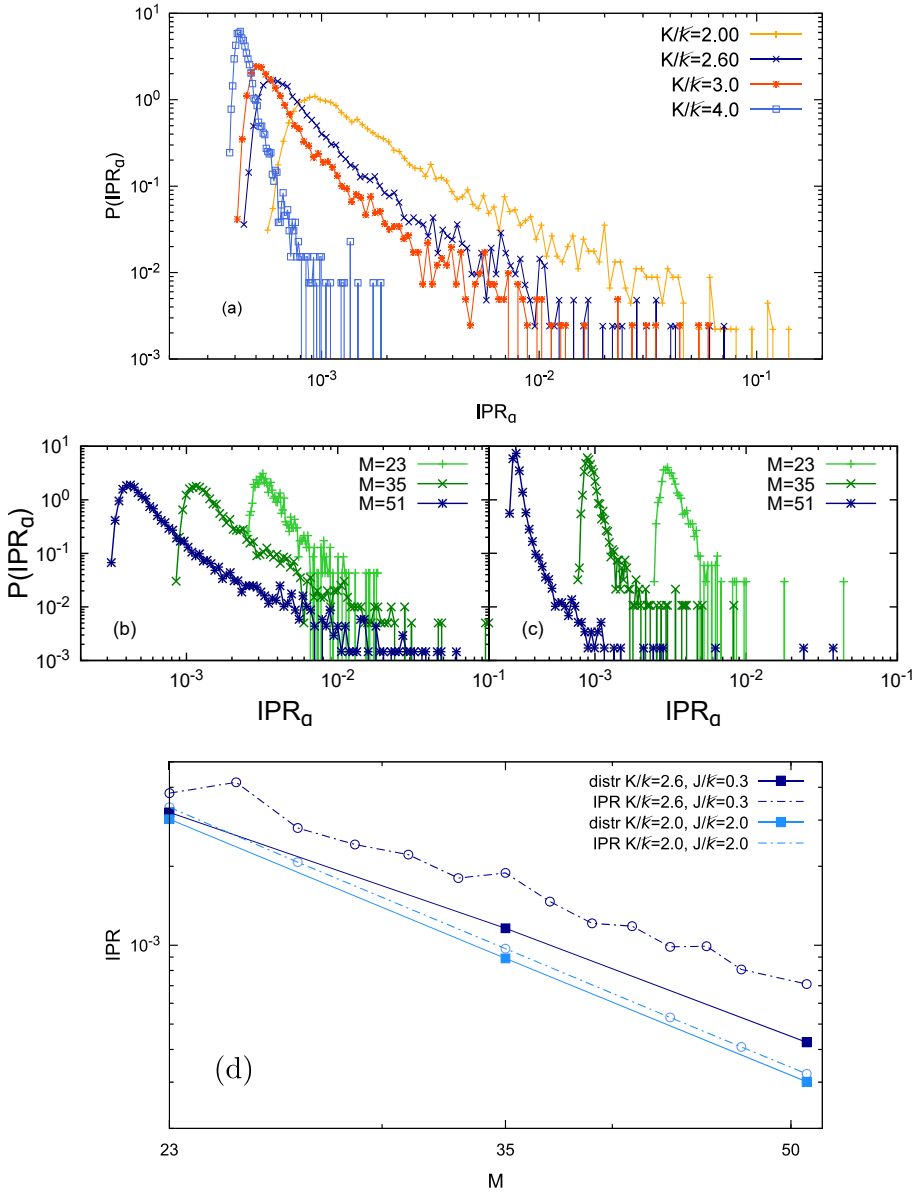

Figure 3.12: (a): Probability distribution of the IPR_α: for increasing values of $K/\bar{k}$ the width of the distribution diminish in the log scale. (b) Probability distribution of the IPR_α computed for $J/\bar{k} = 0.3$ and $K/\bar{k} = 2.6$: the tails of the distributions are power-law with different slopes. (c) Probability distribution of the IPR_α computed for $J/\bar{k} = 2.0$ and $K/\bar{k} = 2.0$: the distributions appear shifted by order of magnitudes as M is increased. (d): positions of the peaks vs M for $J/\bar{k} = 0.3$, $K/\bar{k} = 2.6$ (dark line, full dots) and $J/\bar{k} = 2.0$, $K/\bar{k} = 2.0$ (light line, full dots). The difference between the scaling of the IPR and the positions of the peaks is of order $\sim 0.3\%$ in the ergodic case (light color lines) and $\sim 10\%$ in the other case, due to the larger fluctuations (panel (c)). $\bar{k} = 5.0$.

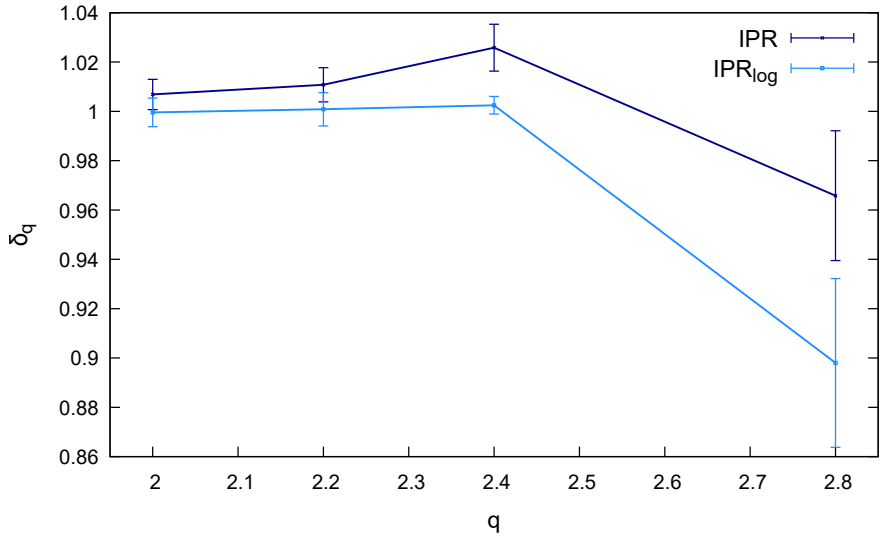

Figure 3.13: The exponent δ_q vs $K/\hbar$ is plotted for $J/\hbar = 0.3$ and $K/\hbar = 4.0$. As long as the values obtained from the linear (dark colored curve) and the log averaged (light colored curve) values are compatible between each other they reveal that the system is delocalized. Other parameters: $M = 51$, $L = 3$, $\hbar = 5.0$.

scaling exponents of different momenta of the eigenfunctions probability distribution. We compute the exponent δ_q defined such that

$$\mathrm{IPR}(q) = \sum_{\alpha} \sum_{\mathbf{m}} |\psi_\alpha(\mathbf{m})|^{2q} \sim 1/\dim \mathcal{H}^{\delta_q(q-1)}\,, \tag{3.2.2}$$

in analogy with Eq. (1.3.14); we indicate with $\mathrm{IPR}_{log}(q)$ the logarithmic average. We have considered decimal fractal dimensions, interpolating the cases between $q = 2$ and $q = 3$. In Figure 3.13 we plot the exponent δ_q in the case $K/\hbar = 4.0$ and $J/\hbar = 0.3$, for which we observed the same scaling of IPR and IPR_{log} (see Figure 3.11). It appears that the higher the momentum, the stronger the role played by fluctuations: we see that for $q \gtrsim 2.4$ the values of $\mathrm{IPR}(q)$ and $\mathrm{IPR}_{log}(q)$ are far apart between each other and for higher momenta we cannot reach convergence of the slope of the curve $\mathrm{IPR}(q)$ vs M.

We conclude that an anomalous ergodic regime emerges close to the localization–delocalization transition line (see Fig. 3.9). In this regime the Floquet eigenstates are characterized by a multifractal structure and their distributions do not satisfy the definition of quantum ergodicity [95]. The presence of fluctuations which emerge in the log scale leads to the question if there is coexistence of eigenstates with different localization properties, but more research would be needed in this direction. By increasing $K/\hbar$ this multifractal behavior disappears, fluctuations are reduced and the eigenstates behave as expected in a thermalizing ergodic system.

Now we focus on the dynamics of the system. We consider as initial state the state $|\psi_0\rangle = |\mathbf{0}\rangle$ with zero angular momentum on each rotor and we study the asymptotic state and the heating process. We expect that the infinite temperature state defined in Eq. (2.3.3) is asymptotically reached. We can check this by looking at the ratio $I(M)$ defined in Eq. (2.3.6) since we know that for a delocalized state it should be

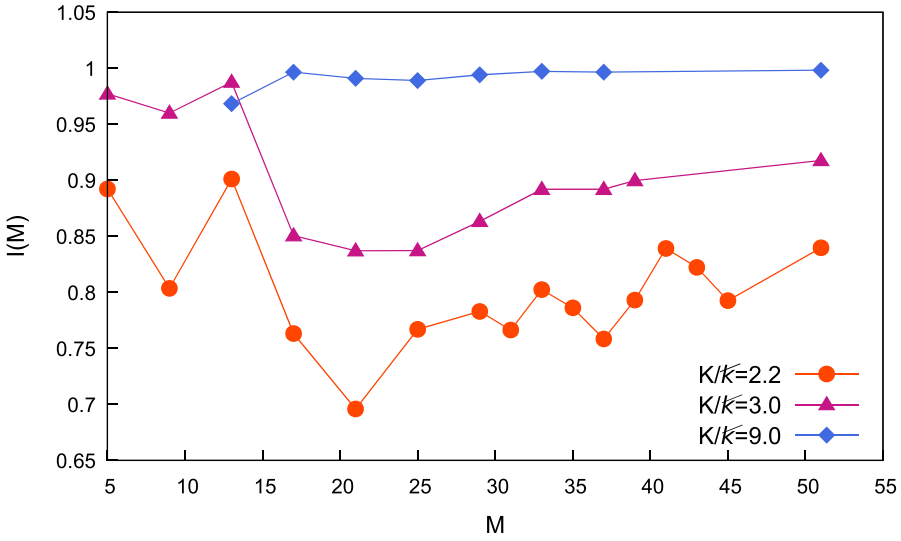

Figure 3.14: The ratio $I(M)$ is plotted for $K/\hbar = 2.2$ (red circles), $K/\hbar = 3.0$ (purple triangles) and $K/\hbar = 9.0$ (blue squares) for $J/\hbar = 0.3$. It is $O(1)$ with M as expected and it approaches one as $K/\hbar$ is increased. This tendency is expected as the fractal structure of the eigenstates becomes trivial for $K/\hbar \gtrsim 3.0$. Other parameters: $L = 3$, $\hbar = 5.0$.

independent of M; moreover, for a thermal state the ratio $I(M)$ is equal to one. In Figure 3.14 we plot $I(M)$ for $J/\hbar = 0.3$ and $K/\hbar = 2.2$ (red circles), $K/\hbar = 3.0$ (purple triangles) and $K/\hbar = 9.0$ (blue squares): the ratio $I(M)$ fluctuates but does not change significantly for all the values of $K/\hbar$ and tends to one as $K/\hbar$ is increased. This result confirms that the system is delocalized but not completely thermal; thermalization is reached at higher $K/\hbar$ where $I(M) \to 1$. We see here for the first time a signature of anomalous thermalization in our system emerging close to the transition line. This result is in agreement with the observation of the multifractal structure of the eigenstates: as long the eigenstates have a nontrivial fractal structure (see Figure 3.11) the asymptotic state is not exactly the infinite temperature one. When the fractal dimensions tend to unit, as it is for $K/\hbar \gtrsim 3.0$, the state at infinite times is thermal and the ratio $I(M)$ tend to one. A comment is in order: the ratio $I(M)$ is related to thermalization, namely to the asymptotic behavior of the system. From its definition (see Eqs. (2.3.6) and (2.3.5)) it emerges that $I(M)$ strongly depends on the structure of the eigenstates via their squared probability amplitudes: we conclude that an the anomalous thermalization revealed by $I(M)$ is a consequence of the anomalous ergodicity discussed above. In the following we move from the analysis of asymptotic properties to the intermediate time dynamics of the system.

To this purpose we consider the energy absorption. We find that in a large region in the delocalized phase the kinetic energy $E(n)$ defined in Eq. (2.3.10) grows in time as

$$E(n) \sim n^{\alpha} \tag{3.2.3}$$

with $\alpha < 1$. As anticipated, we need to check if this result is either physical or due to the truncation. We answer this question by computing $E(n)$ as a function of the

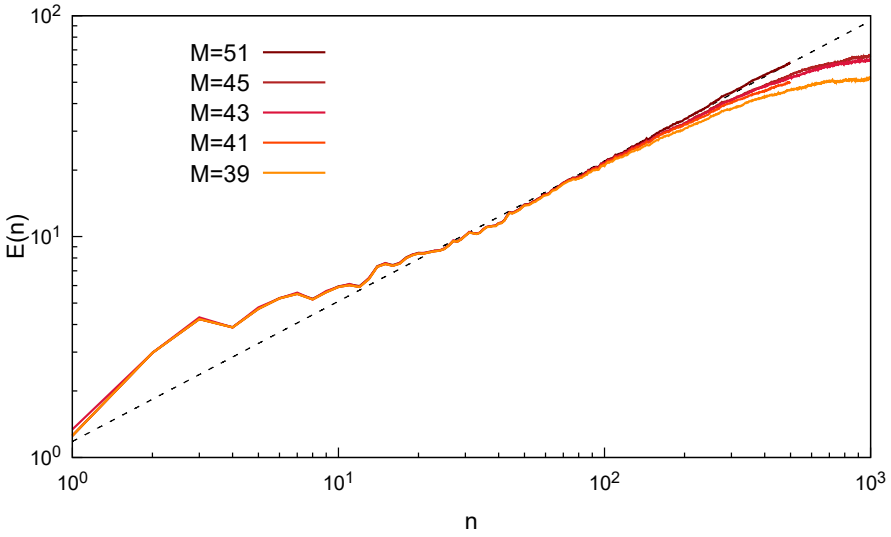

Figure 3.15: The growth of the kinetic energy is plotted for $K/\hbar = 2.2$ and $J/\hbar = 0.3$. The power law appears for the three values of the truncation we consider, from $M = 39$ (lighter curve) to $M = 51$ (darker curve). The time at which the growth stops depends on the saturation value of the energy, which increases with M. It is evident that the larger is M, the longer the time window where the power law persists, the better the fit. Other parameters: $L = 3$, $\hbar = 5.0$.

stroboscopic time n for different values of M. In Figure 3.15 we plot the results for $K/\hbar = 2.2$ and $J/\hbar = 0.3$: we see that the curves follow the same power law up to their saturation to an M-dependent value. In order to see how the power-law exponent depends from $J/\hbar$ and $K/\hbar$ we compute the dynamics at different values of $J/\hbar$ in an interval of values of $K/\hbar$. In order to determine the values of the exponents and the errorbars we compute the power-law exponent over different time intervals: we extract the power-law exponent for each interval, then take the average and the semi-difference between the largest and the smallest data we obtain. We find that the exponent α depends on $J/\hbar$, while it fluctuates around a constant value when $K/\hbar$ is changed. This result is shown in Figure 3.16: we compute the exponent α for $J/\hbar = 0.3, 0.5, 0.7$ and $K/\hbar$ varying in intervals in which we observe the power-law heating.

In order to find an explanation for the power-law growth of the kinetic energy we investigate the statistical properties of the off diagonal matrix elements of the kinetic energy operator. Let us recall that, according to RMT, the distribution of the off diagonal elements is Gaussian. In Figure 3.17 the distributions of the off diagonal elements are plotted and we see that they are not Gaussian. We see that the higher is $J/\hbar$, the closer is the distribution to a Gaussian one: in panel (a) $K/\hbar$ is fixed and $J/\hbar$ increases. On the other side, if we fix $J/\hbar$ and vary $K/\hbar$ the distributions don't change (see panel (b)). This is in agreement with the behavior of the power law we have found: the exponent changes if $J/\hbar$ is varied but oscillates around the same value as $K/\hbar$ is changed at a fixed $J/\hbar$. In order to check that the shape of the distribution is not due to the truncation we show the distributions obtained by fixing $J/\hbar$ and $K/\hbar$ and varying M: in panels (c) and (d) we fix $J/\hbar = 0.3$, $K/\hbar = 2.6$ and

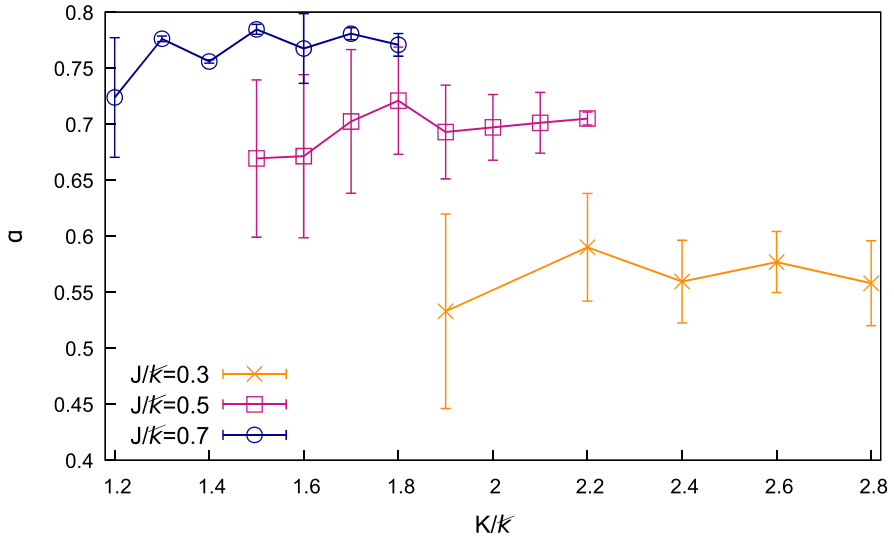

Figure 3.16: The power-law exponent α is plotted for $J/\hbar = 0.3, 0.5, 0.7$ and some values of $K/\hbar$. It appears that the exponent increases as $J/\hbar$ is increased while a clear behavior is not clear in the interval of $K/\hbar$ we can consider within the maximum truncation M we can achieve in our simulations. Other parameters: $L = 3$, $\hbar = 5.0$.

$J/\hbar = 5.0$, $K/\hbar = 2.0$ respectively, finding that the curves coincide; in the second case power law is absent and the distribution is Gaussian in the central part.

In conclusion, we we have found that energy absorption attains an unexpected subdiffusie power-law behavior. It would be interesting to find a relation between this power law and the structure of the Floquet eigenstates: in this way the anomalous ergodicity defined above would be characterized by asymptotic and intermediate-time dynamical properties as well. Encouraged by the results that we have just discussed, we are currently searching a relation between the power-law heating and the distribution of off diagonal elements. We finally remark that a power-law heating like the one observed here has already been observed in quantum systems, both in the single particle as well as in the many body case. In some works the single quantum kicked rotor model has been modified to make the kick quasi periodic and, as a result, the dynamical localization has been destroyed and replaced by a slow heating in time [129, 127, 128, 130]. In other models diffusion in momentum space has been enhanced by colored noise sources: pink noise has been seen to cause slow heating [140], while white noise has been shown to recover the dynamics of the classical model [141, 142]. As an example of many body system in which a power-law heating has been observed, in [53] a $O(n)$ field theory has been studied in which the mass term is periodically driven: after a prethermal regime the system starts heating subdiffusively in time, with a power-law exponent close to $\alpha = 1/2$. In our model the power-law heating naturally emerges from the structure of the Hamiltonian and does not need any noise or disorder source to be enhanced. In the next section we show that an anomalous energy absorption emerges also in a different model in which translational symmetry is broken.

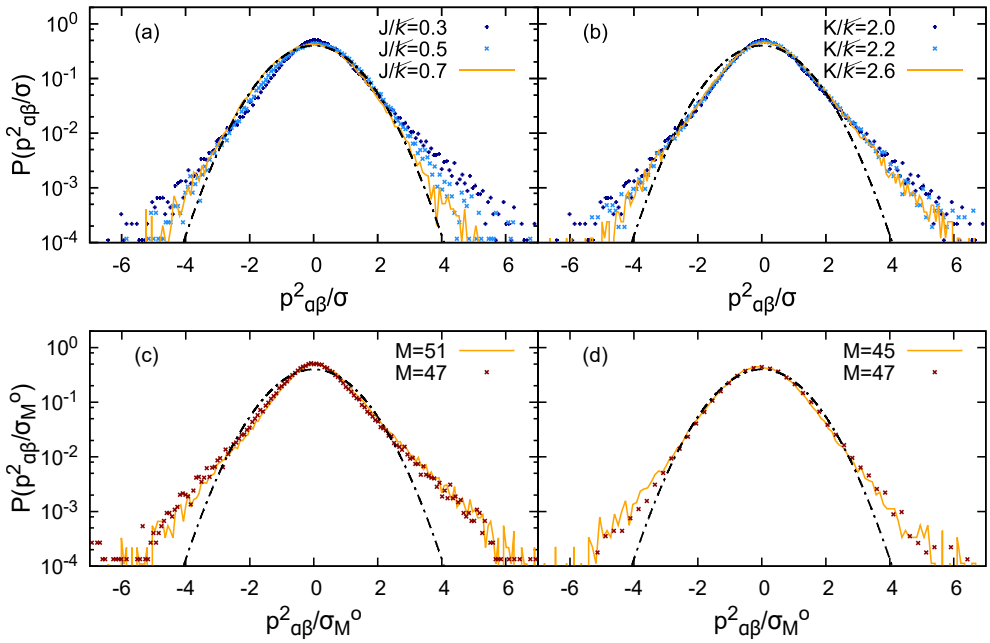

Figure 3.17: (a): Distribution of the off diagonal elements $\{p^2_{\alpha\beta}\}$ for $K/\hbar = 2.0, J/\hbar = 0.3, 0.5$ and $K/\hbar = 1.9, J/\hbar = 0.75$. $M = 51$. (b): Distribution of the off diagonal elements $\{p^2_{\alpha\beta}\}$ for $J/\hbar = 0.3$ and different values of $K/\hbar$. $M = 51$. (c)-(d): distribution of the off diagonal elements $\{p^2_{\alpha\beta}\}$ for $J/\hbar = 0.3$, $K/\hbar = 2.0$ and $J/\hbar = 5.0$, $K/\hbar = 2.0$ respectively and different truncation. $\hbar = 5.0$.

3.3 Dynamical localization in extended models

We have shown in the previous section that our rotors model admits a dynamically localized phase and another in which the kinetic energy $E(n)$ grows unbounded in time: this localization–delocalization crossover takes place in the angular momentum space of each rotor, uniformly in space.

In this section we discuss how dynamical localization and heating are related to transport of energy along the rotors chain: in order to investigate this point we break the spatial translation invariance of the Hamiltonian by studying the dynamics of the system. For small values of $K/\hbar$ and $J/\hbar$ the system is dynamically localized and the dynamical localization is accompanied by a spatial one. In the dynamically delocalized regime characterized by an unbounded growth of the kinetic energy we found that the asymptotic state is the spatially uniform, infinite temperature one. The heating process leading to the infinite temperature state is strongly inhomogeneous in space.

A remark concerning methods is in order: we have used full diagonalization of the Floquet operator for our analysis but, due to the breaking of spatial translations invariance, the only symmetry we can use to reduce the effective Hilbert space dimension is the global momentum parity. This means that the maximum allowed value for the local truncation is $M_{max} = 25$ with $L = 3$. As in the previous simulations we will set $\hbar = 5.0$.

Let start our discussion from the kicking protocol adopted, given by the Hamiltonian

$$\hat{H}_D(t) = \hat{H}_0 + \sum_{n=-\infty}^{+\infty} \delta(t-n)\hat{V}_D(\boldsymbol{\theta})\,, \tag{3.3.1}$$

with the kinetic term unchanged and the kicked part given by

$$\hat{V}_D(\boldsymbol{\theta}) = K\cos\hat{\theta}_1 + J\sum_{j=1}^{L-1}\cos(\hat{\theta}_j - \hat{\theta}_{j+1}) \tag{3.3.2}$$

in which the rotors are coupled by J which is the same for all the sites and K is nonzero only on the site with $j = 1$.

The first quantity we need for our analysis is the local asymptotic imbalance Δ_j. Since we can easily expect that the rotor $j = 1$ absorbs more energy than the other for the definition of the Hamiltonian we define Δ_j normalized as follows:

$$\Delta_j = \frac{E_j(t\to\infty) - E_1(t\to\infty)}{E_1(t\to\infty)}. \tag{3.3.3}$$

It vanishes in the limit in which the energy absorbed by the first rotor is the same as the others and it is close to one in the case of strong imbalance between the asymptotic energies of rotors.

In Figure 3.18 we show a case in which the system passes from exhibiting spatial localization to heating uniformly along the sites as $J/\hbar$ is increased: the imbalance Δ_2 between the first and the second rotors is plotted for $K/\hbar = 0.2$ (orange squares) and $K/\hbar = 0.3$ (green circles). For all the values of $J/\hbar$ in the figure the system is dynamically localized: the values of the asymptotic energies have been obtained by computing the exact dynamics and averaging the values of the kinetic energies once

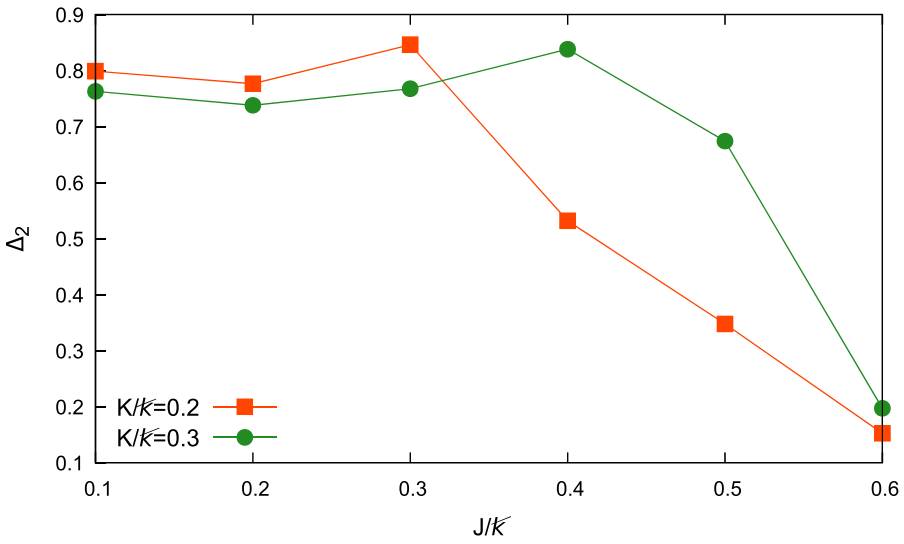

Figure 3.18: The imbalance between the first and the second rotor is plotted for $K/\hbar = 0.2, 0.3$. For $J/\hbar \lesssim 0.3$ the system exhibits both dynamical localization and spatial inhomogeneity in the asymptotic energy profile. By increasing $J/\hbar$ the dynamical localization persists while the energy imbalance vanishes. Other parameters: $L = 3$, $\hbar = 5.0$.

the asymptotic value was reached. The same computation has been performed for different values of M in order to check dynamical localization via the convergence in the energy trajectory.

Now we consider the system governed by the Hamiltonian $\hat{H}_D$ in a region of parameters in which dynamical localization is broken. We compute the dynamics of the system with a fixed M: the asymptotic energies of the rotors are different between each other but this difference diminishes as M is increased. We show this effect in Figure 3.19 in which the imbalance between the second and the first rotor is represented as a function of M. Since it decreases as M is increased we may expect that it goes to zero in the limit $M \to \infty$ and the system reaches the infinite temperature state for $t \to \infty$ but we cannot prove it.

Our next point is to focus on the heating of the system towards its asymptotic state. In Figure 3.20 we plot the kinetic energy of each rotor as a function of the stroboscopic time n for $K/\hbar = 9.0$ and $J/\hbar = 0.5$. The inhomogeneity of the heating process appears very clearly: the energy of the first rotor reaches a saturation value from the very beginning of the simulation, while the energy of the others grows as $n^{\underline{\alpha}_{2,3}}$. The underscores remind that the power-law exponents are different from one site to the other; also, the duration of the power-law regime varies according to the time in which the saturation value is reached.

It is nevertheless crucial to note that the computation relative to Figure 3.20 has been realized with $M = 25$ but the power-law growth phenomenon turns out to be independent from M. It is also remarkable that the phenomenon is very robust with $K/\hbar$: in Figure 3.21 we plot the power-law exponents relative to the energy growth of the second (red triangles) and the third rotor (blue circles): note that the power law exponent does not change sensibly varying $K/\hbar$ in the interval $[2; 40]$ we have

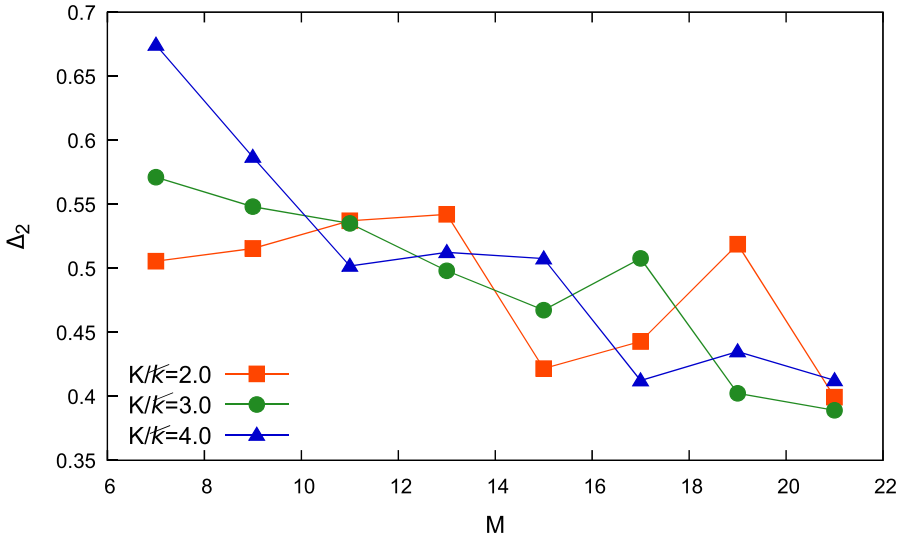

Figure 3.19: Imbalance of the asymptotic energy between the first and the second rotors for $J/\hbar = 0.5$ and $K/\hbar = 2.0$, 3.0, 4.0, (squared, circular and triangular dots respectively). As M is increased the imbalance Δ_2 decreases. Other parameters: $L = 3$, $\hbar = 5.0$.

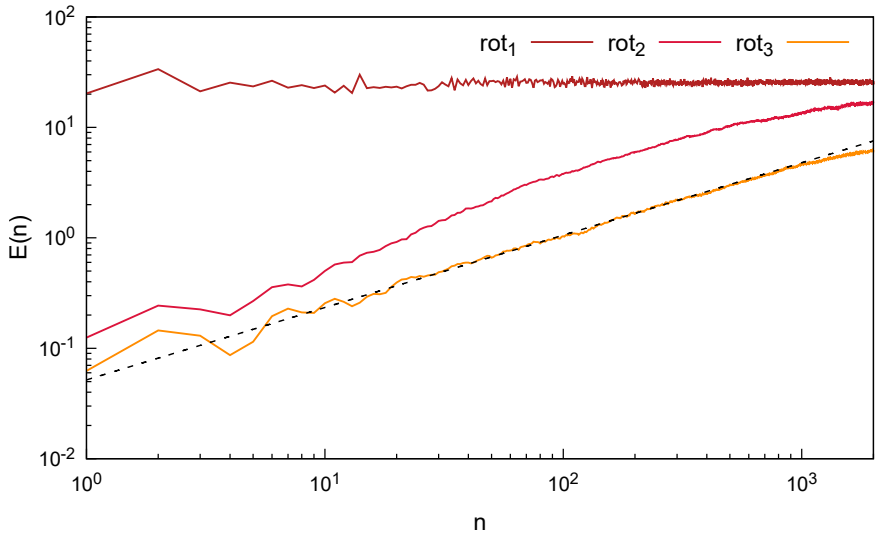

Figure 3.20: Growth of the kinetic energy of each rotor for $K/\hbar = 9.0$ and $J/\hbar = 0.5$. The darkest curve corresponds to the first rotor, the yellow, lighter-colored one to the third. The power law clearly appears for two orders of magnitude in time for $j = 3$. $E(n)$ is expressed in units of $\hbar^2$, according to the definition given in Eq. (2.3.10). Other parameters: $M = 25$, $L = 3$, $\hbar = 5.0$.

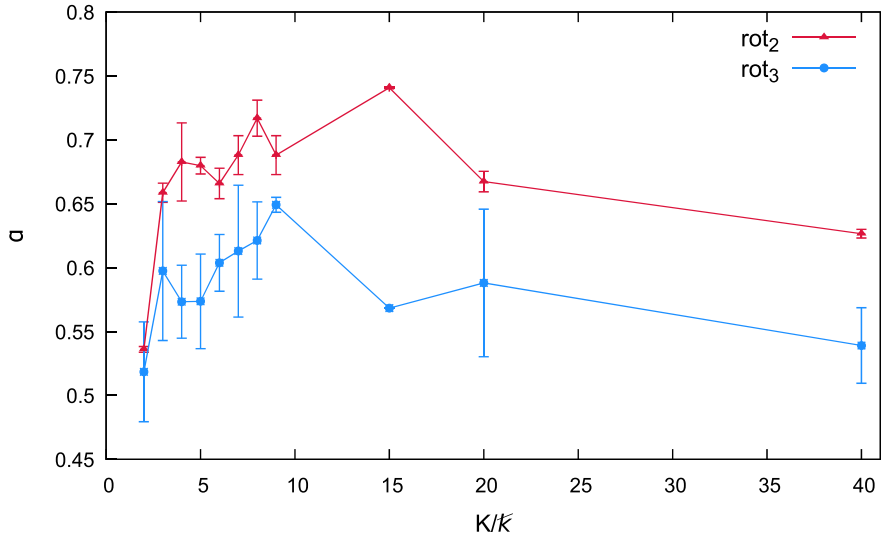

Figure 3.21: Power law exponents for the second and third rotor at $J/\hbar = 0.5$ and $K/\hbar \in [2; 40]$ Blue circles represents the exponents relative to the third rotor, red triangles those of the second. Other parameters: $M = 25$, $L = 3$, $\hbar = 5.0$.

considered.

This inhomogeneity can be quantitatively described, as we will show in the following. In order to do this, we define the probability distribution for the j-th rotor relative to the m-th component in momentum space as follows:

$$|\psi(n)_{m,j}|^2 = \mathrm{Tr}\left[|\psi(n)\rangle\langle\psi(n)| \bigotimes_{i\neq j} \mathbf{1}_i \, |m_j\rangle\langle m_j|\right] \tag{3.3.4}$$

where $|\psi(n)\rangle$ is the state of the whole system at the integer time n and $|m_j\rangle\langle m_j|$ is the projector on the momentum eigenstate m relative to the j-th rotor. With this quantity we can study the evolution of the state site by site. In Figure 3.22 we observe two different profiles of the probability distributions for the first and the third rotor: the former reaches the infinite temperature local state, in which the local momentum eigenstates are equally occupied, from the very beginning of the evolution. Instead, the probability distribution of the latter decays exponentially in the local angular momemtum space with a localization length which increases in time. In the Figure 3.22 we consider the dynamics of the system with $K/\hbar = 9.0$ and $J/\hbar = 0.5$. We plot the marginal probability distributions $|\psi(n)_{m,1}|^2$ (empty dots) and $|\psi(n)_{m,3}|^2$ (full dots) at three different times, $n = 30$, 200, 1000. As anticipated, the probability distribution for the first rotor is uniform in momentum space; instead the marginal distribution of the third rotor can be described as

$$|\psi(n)_{m,3}|^2 \sim \exp(-|m|^\gamma \beta(n)) \tag{3.3.5}$$

with $1 < \gamma < 2$. In principle the exponent γ may be time dependent but we assume as a first approximation that it is constant; on the other side the inverse localization length $\beta(n)$ varies in time. The case $\gamma = 2$ would correspond to a Gaussian probability distribution and would imply a linear growth of the kinetic energy in time. By looking

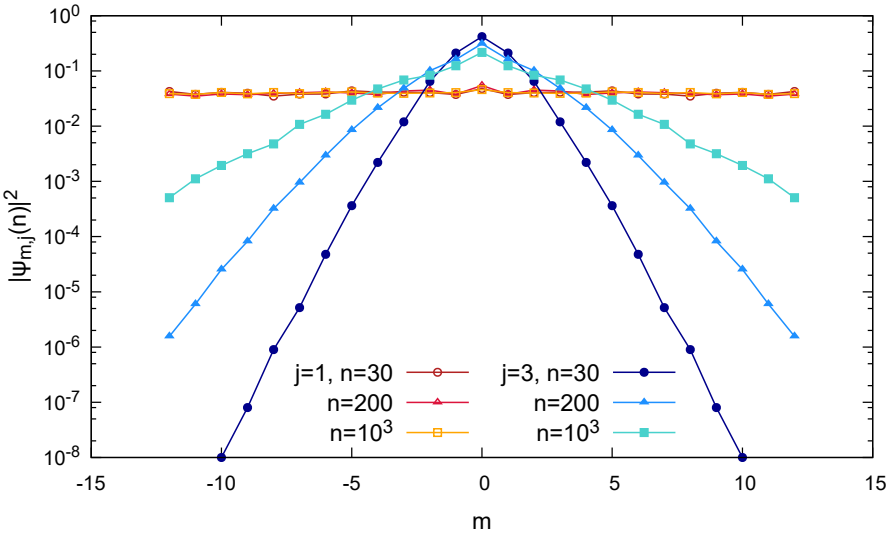

Figure 3.22: The marginal probability distributions $|\psi_{m,j}|^2$ relative to the first ($j = 1$, empty dots) and third rotor ($j = 3$, full dots) are plotted for $K/\hbar = 9.0$ and $J/\hbar = 0.5$ at $n = 30$, 200, 1000 (circular, triangular and squared dots respectively). $|\psi_{m,1}|^2$ is flat and constant in time; $|\psi_{m,3}|^2$ decays exponentially in momentum space with a characteristic length which increases in time. The distributions have been averaged over a small interval of times around the desired n to reduce fluctuations. Other parameters: $M = 25$, $L = 3$, $\hbar = 5.0$.

at the distribtions plotted in Figure 3.22 we choose to fix $\gamma = 1$ as an approximation. Recalling that kinetic energy of the third rotor grows like $E_{j=3}(n) \sim n^\alpha$ we can write the following equation:

$$c\, n^\alpha = \frac{1}{2\Omega(n)} \sum_{m=-\infty}^{+\infty} m^2\, \mathrm{e}^{-|m|\beta(n)} \tag{3.3.6}$$

in which $\Omega(n)$ is a time dependent normalization constant. The parameters c and α are numerically determined by fitting the kinetic energy growth curves as those in Figure 3.20.

The equation 3.3.6 can be inverted to compute the inverse localization length $\beta(n)$ as a function of the power-law exponent α. The first step is to compute the normalization constant $\Omega(n)$: this can be done by solving the equation

$$\sum_{m=-\infty}^{+\infty} \mathrm{e}^{-|m|\beta(n)} = \Omega(n)\,, \tag{3.3.7}$$

coming from $\sum_{m=-\infty}^{+\infty} |\psi(n)_{m,3}|^2 = 1$. After a few passages we obtain

$$\Omega(n) = \mathrm{cotgh}\, \frac{\beta(n)}{2}. \tag{3.3.8}$$

Eq. (3.3.6) can be rewritten as follows:

$$E_3(n) \equiv c\, n^\alpha = \frac{1}{\mathrm{cotgh}\,(\beta(n)/2)} \sum_{m=0}^{+\infty} m^2\, \mathrm{e}^{-m\beta(n)}. \tag{3.3.9}$$

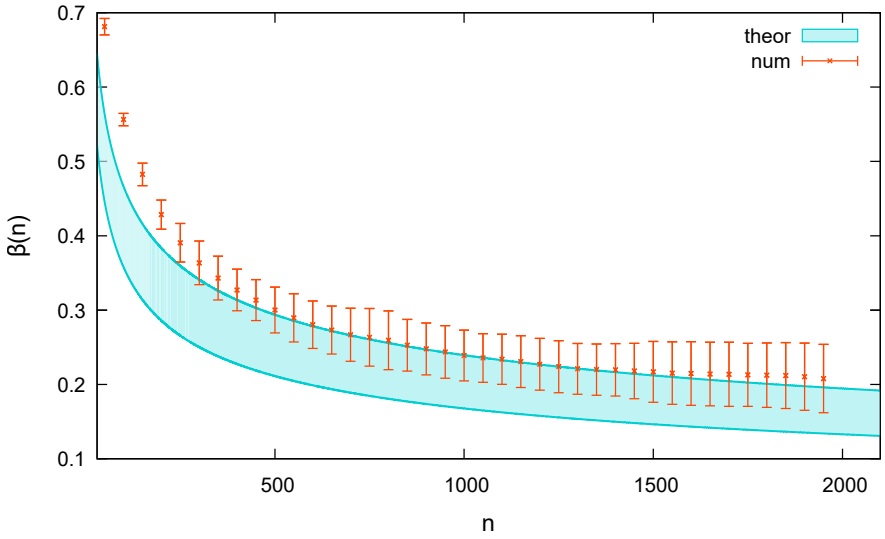

Figure 3.23: The inverse localization length $\beta(n)$ derived from Eq. (3.3.6) is plotted for $K/\hbar = 9.0$ and $J/\hbar = 0.5$. The colored area is obtained by using Eq 3.3.12 with the value of the kinetic energy power-law exponent and the relative error bar. The curve is obtained by measuring the exponent from the marginal probability densities averaged over a time interval shorter than the evolution period. Other parameters: $L = 3$, $\hbar = 5.0$.

At this point we observe that, since the series is absolutely [2] convergent, we can use the following result:

$$\sum_{m=0}^{\infty} z^m m^2 = \left(z\frac{\mathrm{d}}{\mathrm{d}z}\right)^2 \sum_{m=0}^{\infty} z^m = \frac{z(1+z)}{(1-z)^3}\,, \tag{3.3.10}$$

with $0 < z = \mathrm{e}^{-\beta(n)} < 1$. With a few manipulations Eq. (3.3.9) becomes

$$E_3(n) = \frac{z}{(1-z)^2}\,, \tag{3.3.11}$$

from which we obtain as a final result

$$\beta(n) = -\ln\left[\frac{1+2\,c\,n^{\alpha}-\sqrt{1+4\,c\,n^{\alpha}}}{2\,c\,n^{\alpha}}\right]. \tag{3.3.12}$$

The inverse localization length $\beta(n)$ is always positive and its value converges rapidly when the series is replaced by a finite sum: this is important since our marginal probability distribution is affected by the local truncation. We have obtained so far a quantity, $\beta(n)$, whose evolution can be computed in two ways: the first consists in fitting the marginal distribution $|\psi(n)_{m,3}|^2$ in the angular momentum space, starting from Eq. (3.3.5). The second uses the fit of the kinetic energy to compute $\beta(n)$ by using Eq. (3.3.12).

[2] The D'Alambert criterionstates that, given a series with positive terms a_k, if $\lim_{k\to\infty} a_{k+1}/a_k < 1$ then the series is absolutely convergent.

In Figure 3.23 we plot $\beta(n)$ obtained in the two ways and compare the results: the colored area correspond to the computation via the energy fit and Eq. (3.3.12). The errors are determined by the uncertainties of the fit of the exponent α and the initial amplitude. The red-dotted data are obtained by fitting the marginal distribution $|\psi(n)_{m,3}|^2$ and the errorbars have been computed as the variance over a set of close times considered for averaging the probability distributions. Note that the best agreement between the two curves persists in an intermediate time region for $300 \lesssim n \lesssim 1200$: this is the same time interval in which the growth of the kinetic energy is fitted by a power law (see the dashed line in Figure 3.20). Nevertheless a better approximation may be obtained by replacing γ with an additional fitting exponent.

As a conclusion it is interesting to note that a subdiffusive process similar to the one observed in the spatially uniform model has been found. Moreover, in this case the rotors were just subject to the action given by the coupling strength J. Let us also recall that the power law in the previous section was determined mainly by the intensity of the coupling $J/\hbar$ than that of the single kick $K/\hbar$. A full understanding of the role of the coupling term in determining the fractal properties of the system and their influence of its dynamical properties is left for future work: a possible direction could be the study of the system in the case $K = 0$.

3.4 Summary of the results

In this Chapter we have seen that a chain with $L = 3$ coupled kicked rotors exhibits a dynamically localized phase, characterized by the asymptotic saturation of the kinetic energy to a finite value during the evolution of the system. An argument for explaining this behavior is provided by a mapping: it relates a time independent model for a particle hopping in an $L-$dimensional disordered lattice and a chain of L coupled quantum kicked rotors. This mapping allows us to predict that such a dynamically localized phase is present for each $L < \infty$. We have studied the localized phase by looking at the properties of the Floquet eigenstates via the inverse participation ratio and at those of the quasienergies, focusing on the level spacing ratio.

Moreover, if $L \geqslant 3$ the lattice model undergoes the Anderson localization transition: according to the mapping we expect an analogous behavior in the rotor model. Indeed, by increasing the values of $J/\hbar$ and $K/\hbar$ the system is delocalized in the momentum space: we have found an anomalous ergodic region close to the transition line, in which the inverse participation ratio reveals a multifractal structure in the Floquet eigenstates. Far from the localization–delocalization transition line the eigenstates satisfy the definition of quantum ergodicity. In the region of anomalous ergodicity the system exhibits also anomalous thermalization, observed through the asymptotic kinetic energy reached at infinite times. Remarkably we have also observed that the growth of the kinetic energy obeys a subdiffusive power law: this behavior has been put in connection with the statistical properties of the off diagonal matrix elements of the kinetic energy operator even if a complete explanation for this result is still missing.

In the last section we have focused on a different problem, namely the relation between the localization of energy and the spatial inhomogeneities which may appear during the dynamics. We have studied this problem with a different model in which

the translational invariance of the Hamiltonian was broken. We found that if the system is dynamically localized it is possible that the state reaches an asymptotic inhomogeneous state; on the other side, when the system is dynamically delocalized the asymptotic state is the infinite temperature one but the intermediate time dynamics is strongly inhomogeneous.

Chapter 4

Subdiffusion and thermalization towards the limit of large L

While in the previous chapter we have studied the localization/delocalization transition for $L = 3$ rotors, the purpose of this Chapter is to investigate the behavior of a chain of coupled rotors with larger L. As we have shown in Ref. [63] and explained in Appendix C, the mapping introduced in the previous Chapter can be extended to the case $L \to \infty$. In this limit we demonstrate that an infinite dimensional disordered lattice does not exhibit a localized phase: as a consequence we expect that our coupled rotors model is always delocalized in the thermodynamic limit. We apply a mean field calculation to the fully-connected version of the model introduced in Eq. (2.2.1). As a first result we confirm the prediction provided by the model: the system is always dynamically delocalized. But most importantly, we find that the kinetic energy grows as a subdiffusive power-law, analogously to the heating observed in the case $L = 3$. In the second section we study the case $L > 3$ with nearest neighbor interactions. We show that the system with $L = 4$ exhibits two dynamical regimes the first: at large $J/\hbar$ and $K/\hbar$, is characterized by a fast and linear growth of the kinetic energy up to the infinite-temperature value. The second, situated in proximity of the separation between the localized and delocalized phase, is characterized by a subdiffusive heating (as predicted by the mean field in the fully-connected model). We show that these two regimes are accompanied respectively by different properties of the kinetic energy operator matrix analogous to those observed with $L = 3$. Moreover, we find that the anomalous statistics of certain the operators persists for larger L.

4.1 Mean field limit

4.1.1 Formulation

We study directly the large L limit with a mean field calculation which is exact for infinite coordination number or infinite range interactions. For definiteness let us consider the Hamiltonian defined in Eq. (2.2.1) in which the kick term is modified as follows:

$$V(\hat{\boldsymbol{\theta}}) = \left(K \sum_{i=1}^{L} \cos\hat{\theta}_i - J \frac{1}{2(L-1)} \sum_{i \neq j} \cos(\hat{\theta}_i - \hat{\theta}_j) \right) . \tag{4.1.1}$$

We then perform a mean field *Ansatz*: starting from a factorized state, we assume that the system remains factorized during the whole time evolution. Corrections to this behavior turn out to be negligible in the limit $L \to \infty$. The many body initial state we are considering is therefore of the form

$$|\Psi_{\mathrm{MF}}(0)\rangle = \bigotimes_i |\psi_i(0)\rangle \,. \tag{4.1.2}$$

We assume translation invariance, therefore all the initial $|\psi_i(0)\rangle$ are equal to some $|\psi(0)\rangle$, and all of them evolve to the same single-site state. We define this single-site state just before the n-th kick as $|\psi(n)\rangle$: the corresponding many-body state is the tensor product of L copies of this state. In this way, we can describe the dynamics of the system via an effective single particle Hamiltonian containing a time modulation of the kick:

$$\hat{H}_{MF} = \frac{1}{2}\hat{p}^2 + \sum_{n=-\infty}^{+\infty} \delta(t-n)\left[K\cos\hat{\theta} - \frac{J}{2}\left(\psi_{MF}(n)\,\mathrm{e}^{-i\hat{\theta}} + \mathrm{h.c.}\right)\right], \tag{4.1.3}$$

where we have defined the complex mean-field parameter

$$\psi_{MF}(n) \equiv \langle\psi(n)\,|\mathrm{e}^{i\hat{\theta}}\,|\,\psi(n)\rangle\,, \tag{4.1.4}$$

This description is exact for infinite range interactions in the thermodynamic limit. To see this we rewrite the kick term in Eq. (4.1.1) as

$$\begin{aligned} V(\hat{\boldsymbol{\theta}}) = &-\frac{J}{2(L-1)}\sum_{i\neq j}\left[\left\langle \mathrm{e}^{i\hat{\theta}_i}\right\rangle_n \mathrm{e}^{-i\hat{\theta}_j} + \mathrm{h.c.}\right] + \frac{J}{2}\sum_i \left|\left\langle \mathrm{e}^{i\hat{\theta}_i}\right\rangle_n\right|^2 \\ &-\frac{J}{2(L-1)}\sum_{i\neq j}\left[\hat{\delta}_j\hat{\delta}_i + \hat{\chi}_j\hat{\chi}_i\right] + K\sum_{i=1}^{L}\cos\hat{\theta}_i\,, \end{aligned} \tag{4.1.5}$$

where $\hat{\delta}_i \equiv \cos\hat{\theta}_i - \left\langle\cos\hat{\theta}_i\right\rangle_n$ and $\hat{\chi}_i \equiv \sin\hat{\theta}_i - \left\langle\sin\hat{\theta}_i\right\rangle_n$ and $\langle\rangle_n$ is the expectation value over the exact solution of the Schrödinger equation. Imposing translation invariance, the first sum gives the single particle mean-field potential of Eq. (4.1.3). The second sum is in turn a time dependent c-number term that can be neglected. The third sum contains terms in the form $\hat{\delta}_j\hat{\delta}_i$ and $\hat{\chi}_j\hat{\chi}_i$ with $i \neq j$: their expectation value $\langle\hat{\delta}_j\hat{\delta}_i\rangle$ at time n is a spatial connected correlator for the cosine ($\langle\hat{\chi}_j\hat{\chi}_i\rangle$ is the same for the sine). These connected correlators vanish in the thermodynamic limit for each i and j (see Appendix D): more precisely, we explicitly compute $\left\langle\cos\hat{\theta}_i\,\cos\hat{\theta}_j\right\rangle_n$ and show that it can be factorized up to corrections which vanish at leading order as $O(n/L)$, if the state at time $n = 0$ is separable. Therefore the expectation value of the sum of $\hat{\delta}_j\hat{\delta}_i$ grows in a non extensive way ($\sim\sqrt{L}$) and therefore is negligible in the limit $L \to \infty$. We see therefore that spatial correlations vanish for $L \to \infty$. This definitively allows us to study our system via the effective mean-field single particle model described by the Hamiltonian in Eq. (4.1.3).

It is convenient at this point to express the initial wave function in the momentum basis: in the angle representation we have

$$\langle\theta|\,\psi(0)\rangle = \sum_{m=-\infty}^{+\infty} a_m \mathrm{e}^{im\theta}\,, \tag{4.1.6}$$

and average over many random initial conditions with a fixed kinetic energy (the average symbol is $\overline{(\cdot)}$). The initial conditions are obtained by applying one kick to the zero-momentum state and then randomizing the phases of the amplitudes in the momentum basis. We consider initial states such that $a_m = a_{-m}$: it follows that $\psi_{MF}(n)$ is real and that the evolution operator over one period at time n can be written as [1]

$$\hat{U}_{MF}(n) = \mathrm{e}^{-\frac{i}{\hbar}\frac{\hat{p}^2}{2}} \mathrm{e}^{-i\frac{1}{\hbar}[K - J\ \psi_{MF}(n)]\cos\hat{\theta}}\,. \tag{4.1.7}$$

$\hat{U}_{MF}(n)$ depends on the state at time n through the mean field parameter $\psi_{MF}(n)$, which is evaluated according to the prescription given in Eq. (4.1.4). By iterating this procedure we generate the dynamics of the system starting from the initial state Eq. (4.1.6).

As a result of the mean field approach, the many-rotors model is effectively described by a single rotor with a time dependent kicking strength given by

$$K(n) = K - J\psi_{MF}(n)\,. \tag{4.1.8}$$

4.1.2 Results

The quantity on which we focus our analysis is the kinetic energy $E(n) = \overline{\langle\hat{p}^2\rangle_n}/2$ averaged over the initial conditions (for each evolution we define $\langle\hat{p}^2\rangle_n \equiv \langle\psi(n)|\,\hat{p}^2\,|\psi(n)\rangle$). As discussed in the previous section, also in this case the local Hilbert space is infinite dimensional (see Eq. (4.1.6)) and a truncation is therefore necessary. The truncation dimension M varies according to the parameters K and J and to the length of the simulation; it is chosen such that higher momentum states are not involved in the evolution. Notice however that the mean field approximation allows us to use values of M much larger than those used in Chapter 2. The evolution operator defined in Eq. (4.1.7) is factorized in two parts: one is diagonal in the momentum basis and the other in angle representation. We generate the time evolution over one period by applying separately the kinetic and the kick part to the wave-function. We work in the former case in the momentum basis, in the latter in the angle representation.

From the simulations we find that $E(n)$ grows in time according to a power-law n^α, with α depending on $K/\hbar$ and $J/\hbar$ as shown in Figure 4.1 were the exponent α is plotted in the $(K/\hbar, J/K)$ plane. We can distinguish two regions (see Figure 4.1): the red, dark one in which $E(n)$ grows subdiffusively and the yellow, light one in which diffusion is observed. Subdiffusion is an effect purely due to the quantum nature of the system since the classical counterpart always exhibits normal diffusion in all the $(K/\hbar, J/K)$ plane (see Appendix A). The exponent α is almost uniform in all the subdiffusive (red) region in the parameter space with values between 0.6 and 0.7. Some energy time-traces corresponding to different values of $K/\hbar$ and J/K are shown in Figure 4.2. The subdiffusive regime starts at a time t^* which increases by lowering the values of $K/\hbar$ and J/K: during the transient the energy first keeps constant, then it starts growing until it reaches the n^α regime. For certain value of $(K/\hbar, J/K)$ (e.g. $K/\hbar = 1.4$ and $J/K = 0.1$) we do not see the start of either diffusion or subdiffusion

[1] The evolution operator defined in Eq. (4.1.7) preserves the even parity of the state during its evolution: As a conclusion, if $\psi_{MF}(0)$ is real $\psi_{MF}(n)$ is real $\forall n$.

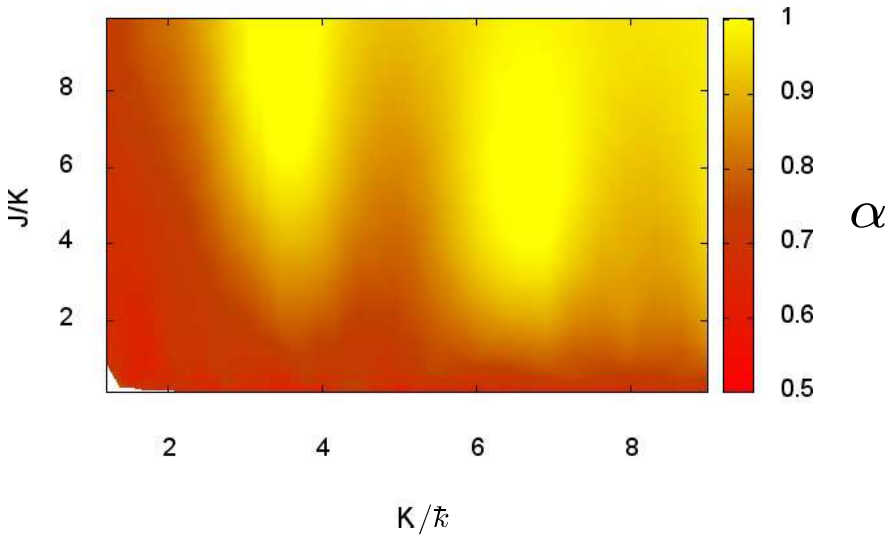

Figure 4.1: The power-law exponent for $E(n)$ growth is plotted against the kick strength $K/\hbar$ and the kick parameters ratio J/K. The subdiffusive region (red, dark one) and the diffusive one (yellow, light one) can be distinguished. The region in the left-bottom corner is not plotted since a stable growth regime does not start within the simulation time length. Other parameters: $M = 4096$, $\hbar = 2.89$.

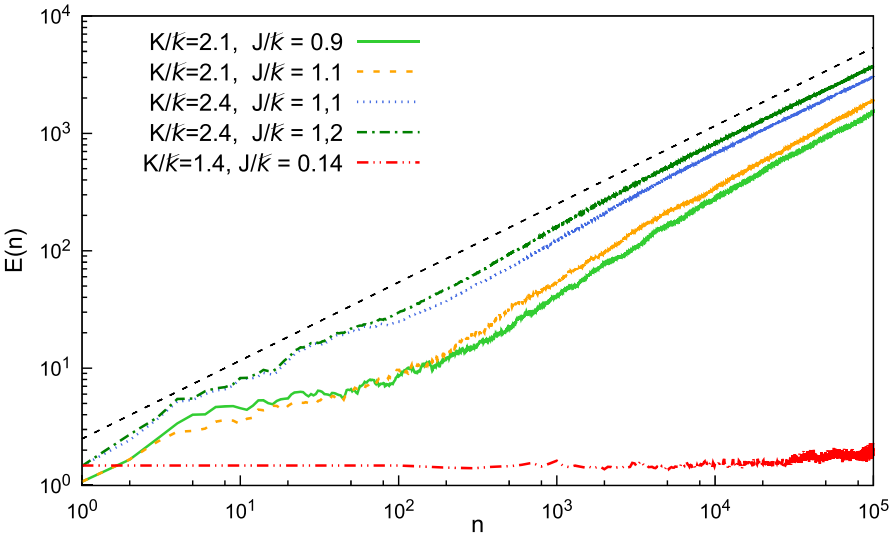

Figure 4.2: Time evolution of $E(n)$ is plotted together with the dashed curve $n^{2/3}$ as a guide to the eye: the power-law growth of $E(n)$ starts at different times but is characterized by an exponent α with a value in the interval [0.6, 0.7]. For $K/\hbar = 1.4$ the energy starts growing at $t \sim 10^6$. Other parameters: $M = 4096$, $\hbar = 2.89$..

within our simulation time ($\simeq 10^6$): the trend appears however to rule out localization but rather suggest that $t^* \geqslant 10^6$.

The dynamics generated through the introduction of the mean field parameter is that of a process in which at each period of time the parameter $K(n)$ is changed and a different Floquet operator is in fact introduced. It seems remarkable that a delocalized regime comes out even if each one of the Floquet operators which are involved during the dynamics would generate dynamical localization if taken separately. The reason can be clarified through the following argument: let us consider the Floquet operators $\hat{U}_F(n)$ and $\hat{U}_F(n+1)$ corresponding to two consecutive periods of evolution , whose eigenstates and quasienergies are $\{|\psi_\alpha\rangle, \mu_\alpha\}$ and $\{\phi_\beta\rangle, \nu_\beta\}$ respectively. Given the state $|\psi(n)\rangle$ we have that

$$\begin{aligned} |\psi(n+2)\rangle &= \hat{U}_F(n)\hat{U}_F(n+1)|\psi_(n)\rangle \\ &= \sum_\alpha \mathrm{e}^{-i\mu_\alpha}|\psi_\alpha\rangle\langle\psi_\alpha| \sum_\beta \mathrm{e}^{-i\nu_\beta}|\phi_\beta\rangle\langle\phi_\beta|\psi(n)\rangle \\ &= \sum_{\alpha,\beta} \mathrm{e}^{-i\mu_\alpha - i\nu_\beta}|\psi_\alpha\rangle\langle\psi_\alpha|\phi_\beta\rangle\langle\phi_\beta|\psi(n)\rangle. \end{aligned} \tag{4.1.9}$$

It is known from Random Matrix Theory that despite $\hat{U}_F(n)$ and $\hat{U}_F(n+1)$ are originated from a small variation of a parameter in the Hamiltonian, their eigenstates can be dramatically different. It follows that the matrix $\langle\psi_\alpha|\phi_\beta\rangle$, which is the identity one in absence of interaction, is a random one and therefore localization is broken.

Let us finally remark that a fundamental role in the power-law heating mechanism is played by the mean field parameter, whose properties change as the heating process change from subdiffusive to diffusive. In Appendix E we go through the comparison between the energy evolution and the dynamics of the mean field parameter.

4.2 Signatures of subdiffusion and anomalous thermalization for large L

In the previous section we have shown, via a mean field calculation, that delocalization is characterized by a power-law growth of the kinetic energy which is subdiffusive in part of the space of couplings $(J/\hbar, K/\hbar)$. Although this approach is exact only in the fully-connected model when $L \to \infty$, the subdiffusive heating dynamics has properties similar to those we have found in the case of three rotors: in particular we refer to the existence of a stable power-law subdiffusive regime for small values of $J/\hbar$ and $K/\hbar$, which becomes diffusive as they are increased. Moreover, we have seen that the subdiffusive heating is accompanied, in the case $L = 3$, by a non Gaussian distribution of the off-diagonal and diagonal elements of the kinetic energy operator matrix. In this section we present results obtained by applying full exact diagonalization to the study of the system in the case $L > 3$ with nearest neighbor interactions in order to shed some light on the possible origin of their subdiffusion.

We start our analysis by showing that the localized region reduces as L is increased. To this purpose we computed the averaged ratio $\langle r\rangle$ for $L = 3, 4, 5$. The result is plotted in Figure 4.3 at the fixed value $J/\hbar = 0.3$: it emerges that the interval of values of $K/\hbar$ in which $\langle r\rangle$ is close to the Poisson value, suggesting dynamical localization,

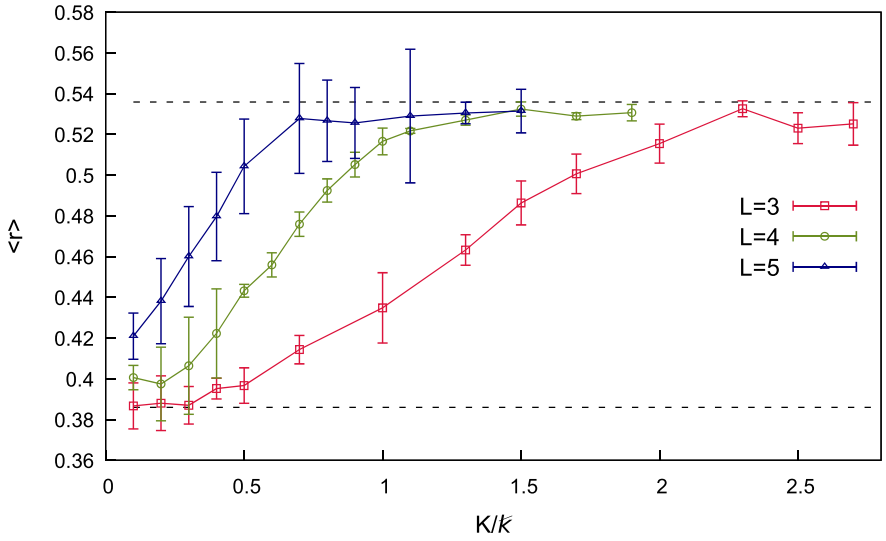

Figure 4.3: The average ratio $\langle r \rangle$ is plotted for $J/\hbar = 0.3$ with $L = 3, 4, 5$. The localized region, corresponding to $\langle r \rangle \simeq 0.386..$ smoothly disappears as L is increased. The values have been obtained by averaging over the results got from different M; the errorbars have been computed as the standard deviation of the available data. The largest errorbars correspond to the cases in which a complete convergence in M cannot be achieved. Other parameters: $\hbar = 5.0$.

is shorter as L is increased [2]. Note also that the region in which $\langle r \rangle$ assumes an intermediate value reduces as well, revealing that the only phase which remains in the thermodynamic limit is the delocalized one.

Concerning the growth of the kinetic energy, in the delocalized region we observe a fast, linear growth for $L = 4$. Close to the localization – delocalization transition line relative to $L = 4$ and we find instead that the kinetic energy of the rotors grows as a power-law. We observe at the same time that the distribution of the matrix elements is not in agreement with Random Matrix Theory predictions, confirming what we found in the case $L = 3$ as discussed in section 3.2.2. Unfortunately the natural question about the fate of this subdiffusion for $L \to \infty$ cannot be directly studied for $L > 4$ since a sufficiently large truncation is not numerically accessible. Nevertheless the anomalous properties of the matrix elements distributions mentioned above are found to survive for higher values of L up to a finite truncation M^*. We are performing further research is being to understand the large-L limit of the system as $K/\hbar$ and $J/\hbar$ are changed. In the following paragraph we study a case in which the dynamics of the system is ergodic, while a case in which anomalous properties emerge is discussed in Paragraph 4.2.2.

[2] The maximum values of M we can access diminish as L increases. In particular, for $L = 3, \ldots 8$ we have $M_{max} = 51, 23, 13, 7, 5, 5$ respectively. At a given M we have $\dim \mathcal{H}_L = M^L/(4L)$. This limitation restricts the possibility of studying the exact dynamics of the system.

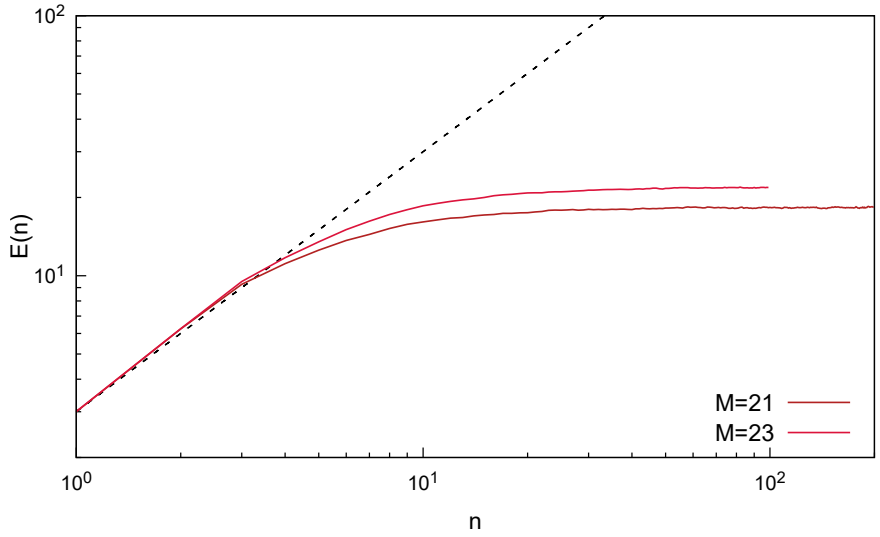

Figure 4.4: The linear growth of the kinetic energy is shown for $L = 4$ with $M = 21, 23$. The dashed line has slope $\alpha = 1$. Other parameters $\hbar = 5.0$.

4.2.1 Ergodic regime

The ergodic regime is observed by choosing large values for $J/\hbar$ and $K/\hbar$. In this paragraph we set $J/\hbar = K/\hbar = 2.0$ unless differently specified. As anticipated above we first show that the growth of the kinetic energy is linear in time, as it emerges from the traces plotted in Fig,ure 4.4: we set $L = 4$ and use $M = 21, 23$. The slope of the dashed line is one, to confirm our result.

Now we focus on the properties of the kinetic energy operator matrix, starting our analysis from the distribution of the off-diagonal elements, as we did in the previous chapter. In the inset (a) of Figure 4.5 we show that the distributions are Gaussian and independent from the truncation M once they have been normalized to their variances. In the inset (b) we show that the distributions do not change also at larger sizes L: in order to reach $L = 8$ we set $M = 5$. The different curves correspond to different L. A Gaussian distribution is plotted with a dashed line as a guide to the eye.

Let us now focus on the variances of these distributions obtained at different L with $M = 5$: the ETH predicts that the fluctuations of the off-diagonal elements should scale as fast as the inverse of the square root of the Hilbert space dimension: in Figure 4.6 we plot the quantity $\sigma_L\sqrt{\dim\mathcal{H}_L}$ for different choices of $J/\hbar$ and $K/\hbar$ for verifying this condition. In particular we start from $K/\hbar = 2.0$, $J/\hbar = 2.0$ and go to smaller values. If ETH is satisfied we expect the following relation to hold:

$$\sigma_L\sqrt{\dim\mathcal{H}_L} \sim const \tag{4.2.1}$$

as a function of L. We see that for large values of $J/\hbar$ and $K/\hbar$ the condition is satisfied, but ceases to be true if the values of the parameters are decreased under a certain threshold. The second statement contained in the ETH concerns the distribution of the diagonal elements and their fluctuations and allows to predict the asymptotic behavior of the system.

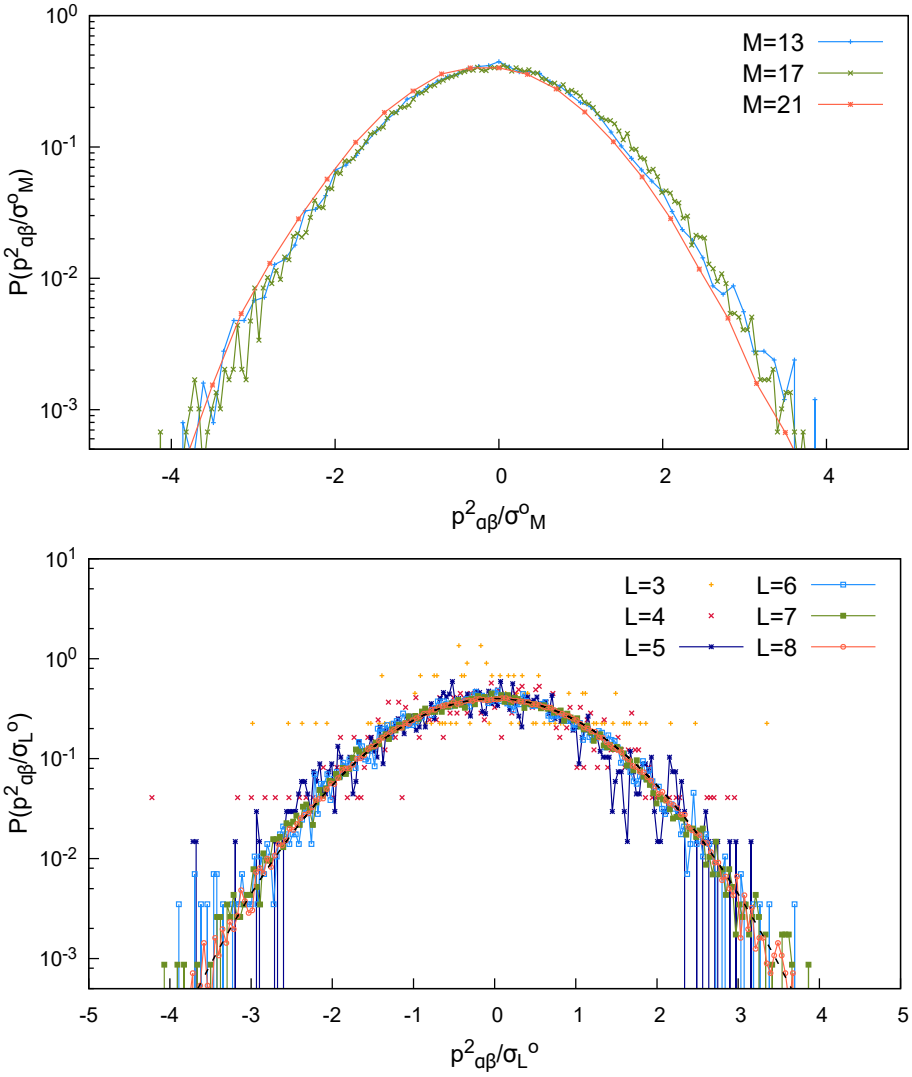

Figure 4.5: (a): Distribution of the off-diagonal elements $\{p^2_{\alpha\beta}\}$ for $L = 4$ and different truncations. (b): Distribution of the off-diagonal elements $\{p^2_{\alpha\beta}\}$ for $L = 3, \ldots 8$. For all the curves $M = 5$. We plot a Gaussian distribution with a dashed line as guide to the eye. Parameters: $K/\hbar = J/\hbar = 2.0$, $\hbar = 5.0$.

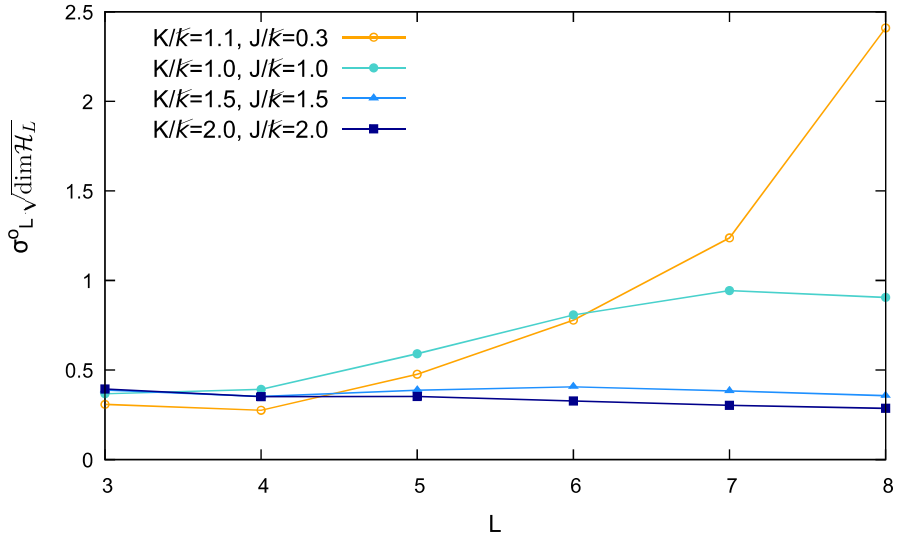

Figure 4.6: The scaling of the variance of the off-diagonal elements distribution is plotted as a function of L. Bottom lines (full dots) agree with Eq. (4.2.1), showing that ETH is satisfied. The top line (yellow empty dots) corresponds to a case in which the system exhibits anomalous thermalization. Other parameters $M = 5, \bar{k} = 5.0$.

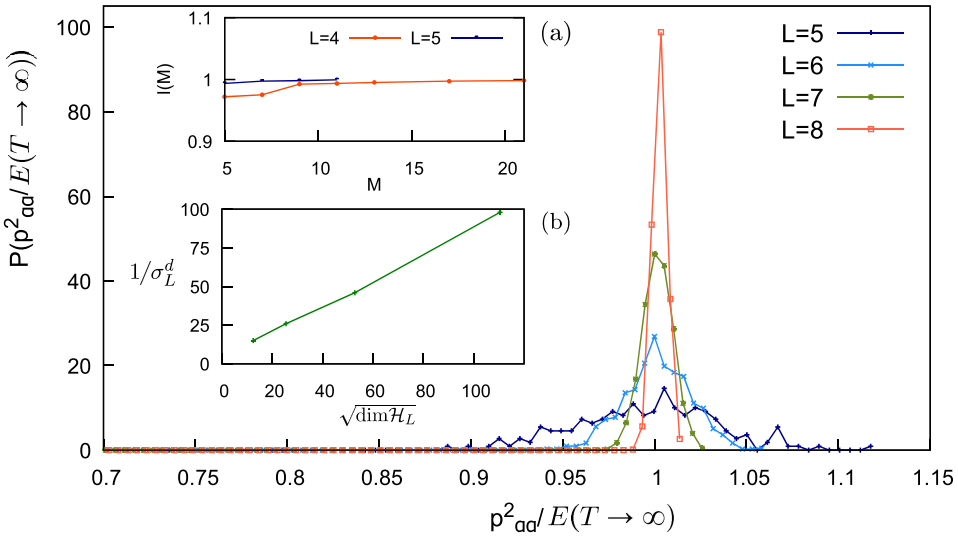

Figure 4.7: Distribution of the $p^2_{\alpha\alpha}$'s for $L = 5, \dots 8$ and $M = 5$. The x axis values have been normalized to the infinite-temperature energy $E(T \to \infty)$ to make the center of the distribution more clear. Inset (a): the ratio between the infinite time energy and the infinite-temperature one is plotted against M to show that ergodicity is satisfied independently from the local truncation. Inset (b): the inverse of the variance, computed as the height of the distributions, increases linearly with $\sqrt{\dim \mathcal{H}_L}$. Parameters: $K/\bar{k} = J/\bar{k} = 2.0$, $\bar{k} = 5.0$.

The distribution of the diagonal matrix elements is plotted in Figure 4.7 for different sizes of the system and $M = 5$: the distributions are centered around the infinite-temperature energy. This first observation is in agreement with the ETH, according to which all the Floquet eigenstates belong to the microcanonical energy shell corresponding to an infinite temperature. As a consequence of this first result, the system is ergodic in the sense that the asymptotic state is the infinite-temperature one, independently from the initial condition: as an example we plot in the inset (a) the ratio between the asymptotic average energy and the infinite-temperature one, which is $I(M) = 1$ for both $L = 4, 5$ in the limit of large truncation values M.

The second observation deriving from Figure 4.7 is that the width of the distributions diminishes as L is increased: this is related to the ETH, according to which the distribution is Gaussian with fluctuations scaling as the inverse of the square root of the Hilbert space dimension. To verify this requirement we plot the inverse of the variance of the distribution against the square root of the Hilbert space in the inset (b). The inverse of the variance coincides with the height of the probability distribution in the Gaussian case. The relation between $1/\sigma_L$ and $\sqrt{\dim\mathcal{H}_\mathcal{L}}$ is linear, confirming that the distributions are Gaussian and their fluctuations satisfy the scaling predicted by the ETH.

The results we have just shown are the same for different choices of $K/\hbar \gtrsim 1.0$ and $J/\hbar \gtrsim 1.0$. We have therefore verified what follows: first, that the system is ergodic, in the sense that diagonal matrix elements are distributed in such a way that the asymptotic state is the infinite-temperature one independently on the initial state. Second, that ETH predictions concerning fluctuations and the consequent equivalence between the microncanonical average and a single eigenstate expectation are valid for large values of $J/\hbar$ and $K/\hbar$.

4.2.2 Anomalous regime

We move now to the analysis of the system in a case in where anomalous properties are present. We consider again Figure 4.6: it emerges that by decreasing $K/\hbar$ and $J/\hbar$ the fluctuations of the off-diagonal elements decrease slower than the square root of $\dim\mathcal{H}_\mathcal{L}$, explaining the positive slope of the curves corresponding to $K/\hbar = 1.0, J/\hbar = 1.0$ and $K/\hbar = 1.1, J/\hbar = 0.3$ (full and empty circular dots, respectively). We focus in particular on the behavior of the system in this last case.

In order to understand the origin of this slow scaling of the variances we compute the corresponding distributions: the results are plotted in Figure 4.8. We have set $M = 5$ and standardized the distributions. We remarkably notice that in this case the distributions are not Gaussian, in contrast to what we found in the previous case. This behavior seems to be independent on L, since the distributions do not change significantly for different values of L. In order to check that this feature is not a fictitious effect of the Hilbert space truncation we computed the same distribution for $L = 4, 5$ for different values of M. The results are plotted in Figure 4.9: the inset (a) contains the distributions for $L = 4$, the inset (b) those for $L = 5$. In both cases the distributions coincide for different values of M and keep a non Gaussian shape in the tails. Moreover, the fluctuations decrease for different values of M not as rapidly as they should according to ETH: this is shown in Figure 4.10 where the variance of the distribution, multiplied by $\sqrt{\dim\mathcal{H}_L}$, is plotted against the size of the system for

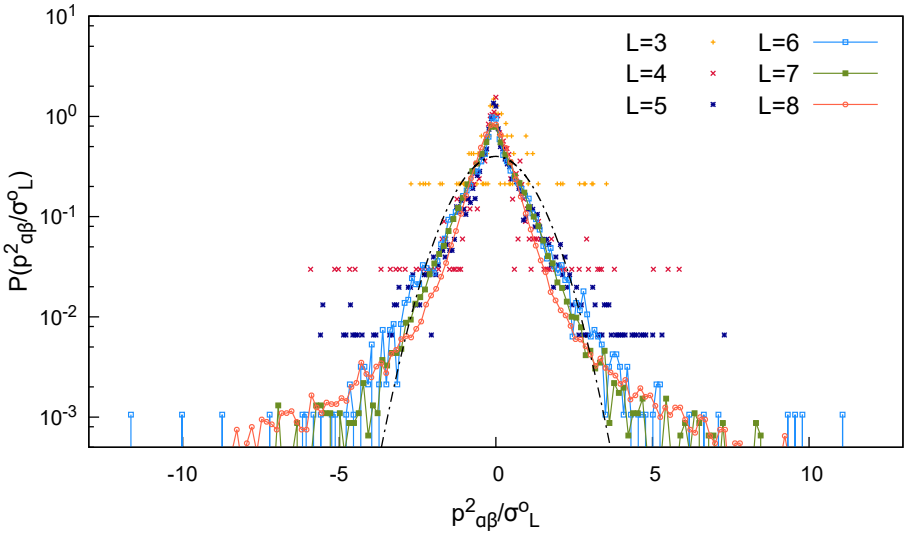

Figure 4.8: The distribution of the off-diagonal elements $\{p^2_{\alpha\beta}\}$ of the kinetic energy operator is computed for $L = 3, \dots 8$ with $K/\hbar = 1.1$ and $J/\hbar = 0.3$. For all the curves $M = 5$. The curves in the plot are standardized but, differently from the previous case, the distributions are not Gaussian. We plot a Gaussian distribution with a dashed line as a guide to the eye. The elements $p^2_{\alpha\beta}$ are chosen such that the difference between the quasienergies $\epsilon_\alpha - \epsilon_\beta$ is sufficiently small. Other parameters $\hbar = 5.0$.

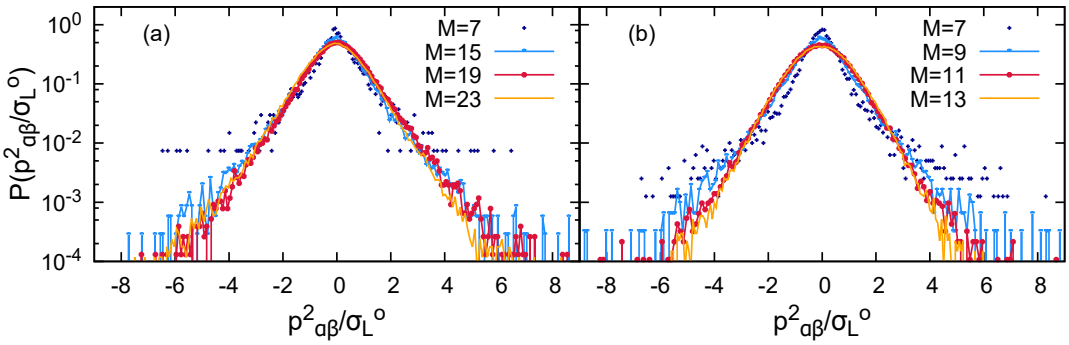

Figure 4.9: The distribution of the off-diagonal elements $\{p^2_{\alpha\beta}\}$ of the kinetic energy operator is computed for $L = 4, 5$ with $K/\hbar = 1.1$ and $J/\hbar = 0.3$. In panel (a) $L = 4$ and $M = 7, \dots, 23$. In panel (b) $L = 5$ and $M = 5, \dots, 13$. Other parameters $\hbar = 5.0$.

$M = 11$.

It is remarkable that this distribution of the off-diagonal elements is accompanied by a power-law subdiffusive growth of the kinetic energy. We show this behavior for $L = 4$: in Figure 4.11 we plot the kinetic energy of the system as a function of time in the case $L = 4$; the choice of different values of M is necessary, as we have shown for $L = 3$, to ensure that the behavior we observe is physical and not due to the artificial truncation.

We conclude our analysis by looking at the distribution of the diagonal matrix elements to compare these results with those obtained in the ergodic case. In Figure

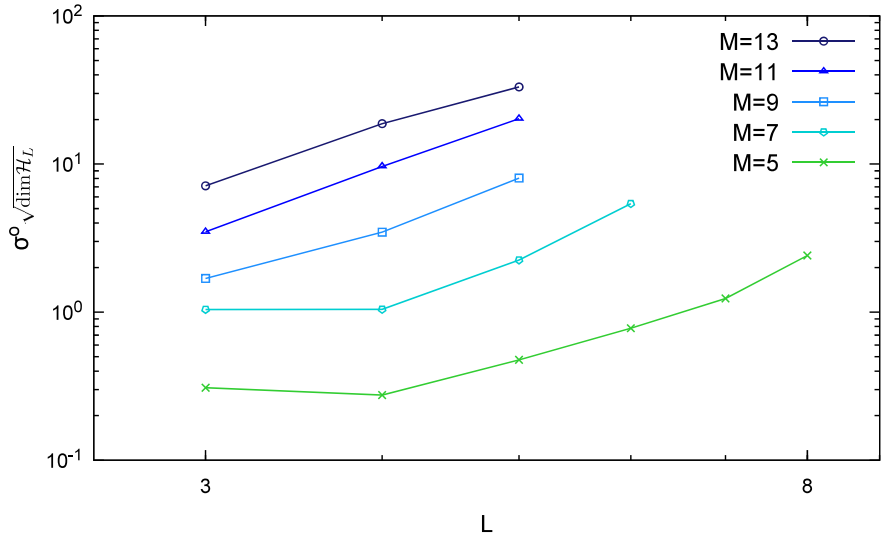

Figure 4.10: The variance of the distribution of the off-diagonal elements $\{p^2_{\alpha\beta}\}$of the kinetic energy operator is computed for $M = 5, \ldots, 13$ with $K/\hbar = 1.1$ and $J/\hbar = 0.3$. The curves have a positive slope since the variances are multiplied by $\sqrt{\dim\mathcal{H}_L}$, revealing for each M that the decrease is not as fast as predicted by ETH. Other parameters $\hbar = 5.0$.

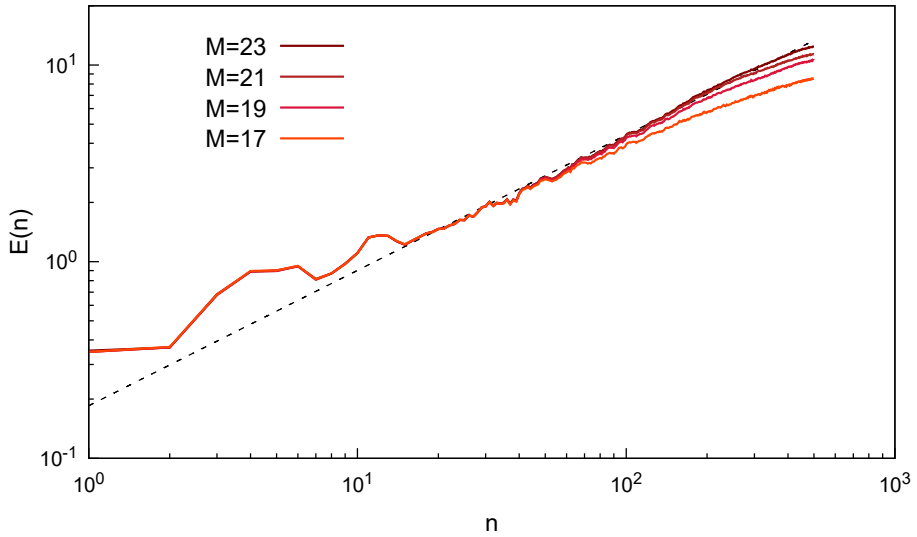

Figure 4.11: The subdiffusive growth of the kinetic energy is shown for $L = 4$. Different values of M show that the trajectory converges for longer interval of times as M is increased. The power-law exponent is $\alpha = 0.688265 \pm 0.005236$. Other parameters $\hbar = 5.0$.

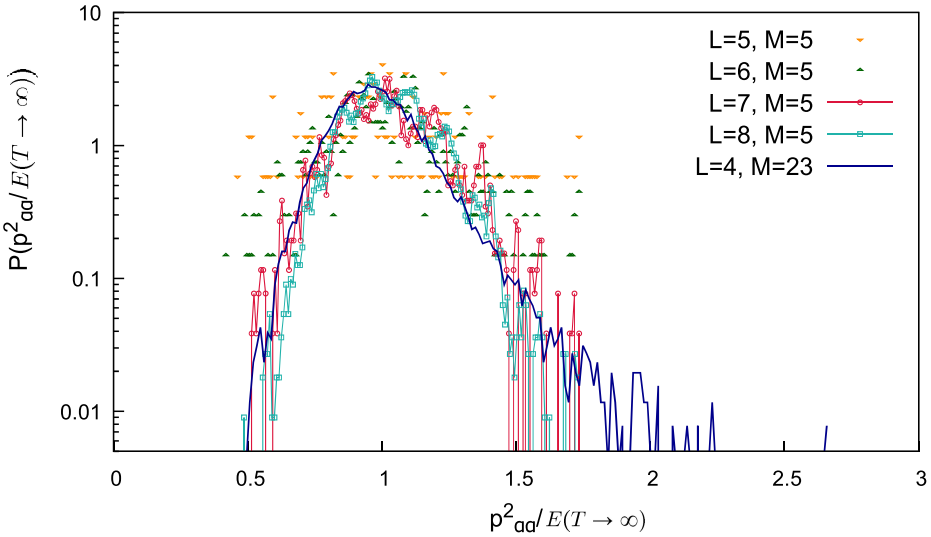

Figure 4.12: The diagonal matrix elements of the kinetic energy operator are plotted for $M = 5$ and $L = 5, ..., 8$ and $L = 4$ with $M = 23$. Note the distributions do not change in height and width as we found in the ergodic case, see Figure 4.7. Other parameters: $K/\hbar = 1.1$, $J/\hbar = 0.3$, $\hbar = 5.0$.

4.12 the distribution of the diagonal matrix elements is plotted for different values of L with $M = 5$ and with $M = 23$ in the case $L = 4$. The last curve is to show that the distribution is independent on M at least for $L = 4$.

We note two features which reveal that the system does not obey ETH, differently from the ergodic case: the distributions do not exhibit a scaling of their width as the dimension of the Hilbert space increases. On the contrary, in the previous case in which ETH was satisfied we showed that the fluctuations decrease exponentially with L (see Figure 4.7). The second element is that the width is much larger than the distribution in the ergodic case: in this way it is clear that the expectation value of the kinetic energy taken on a single eigenstate is not sufficient to obtain the microcanonical expectation value.

We can conclude by saying that we have shown that an anomalous diffusive behavior is present also in the case $L = 4$ close to the transition line which separates the localized and the delocalized phases. This power-law is accompanied, for the parameters we investigated, by anomalous properties of the distributions of the kinetic energy operator matrix elements: since these distribution preserve their properties as L is increased we may argue that also for higher sizes of the system a subdiffusive regime may be found. In this paragraph we have chosen two points in the parameter space and studied the properties of the system in these cases, but further research would be needed to understand how the behavior of the system changes as a function of $K/\hbar$ and $J/\hbar$.

Two final comments are in order: the first regards the anomalous properties of the operator matrix we have presented. They have already observed in other systems [139, 64, 143]: in these cases, as in our system, features revealing anomalous thermalization have been observed close to the critical value of the disorder in a many-body localized spin chain. The difference with our system is the absence of a conserved

quantity, showing that this phenomenon applies to a more general class of systems, and the absence of disorder: indeed, in our case the anomalous heating and thermalization mechanisms are built into the nonlinear Hamiltonian. The fact that other nonlinear systems displays anomalous thermalization [144, 145] reveals that indeed this phenomenon may be characterized by some universal feature which would be interesting to study.

The second comment concerns the intermediate heating process and its correlation with the distribution of the off-diagonal matrix elements and, more in general, with the ETH: in a different system the question has already been posed [53], even though a solution is missing. Our outlook is to focus on the properties of the eigenstates, whose structure is responsible both for the anomalous spreading of a localized initial state in the angular momentum representation (kinetic energy subdiffusion) and for the distribution of the operator matrix.

4.3 Summary of the results

In this Chapter we have presented the results concerning the system at large values of L. By means of a mean field calculation we have predicted the heating behavior of the system in the fully-connected model: it is remarkable that the local heating process follows a power-law growth of the kinetic energy analogous to the one observed in the case with $L = 3$. Then, we have performed an analysis, based on exact diagonalization, to infer the thermalization properties of the system as the number of rotors is increased. We have found that for high values of the kick parameters the dynamics of the system is characterized by a linear growth of the kinetic energy; the system is ergodic, in the sense that the infinite-temperature state is reached independently on the initial state and the ETH is satisfied. We checked this property by analyzing the distribution of the diagonal and off-diagonal matrix elements of the kinetic energy operator.

Remarkably, we have shown that, for $L = 4$, the system exhibits anomalous heating in the proximity of the localization–delocalization transition line; this phenomenon is accompanied by anomalous distributions of the elements of the kinetic energy operator matrix. Most interestingly, we have shown that these properties do not change with L. Even though further research is needed for a complete understanding of this observation we argue that a region in parameters space in which the system is characterized by an anomalous heating may be found in the limit of large values of L.

Conclusions

This Thesis has been devoted to the study of L coupled quantum kicked rotors. In contrast with the behavior of the QKR, which is always dynamically localized, a very rich phenomenology arises when interactions are added to the single rotor model. First of all, we have observed two distinct phases, a dynamically localized and a delocalized one. The observation of a localized phase is in contrast with the behavior of its classical counterpart; moreover it violates the common definition of quantum chaos, according to which a chaotic classical system behaves chaotically in the quantum limit.

We have explained the presence of these two phases with the original mapping introduced in Section 3.1: we have shown that the dynamical localization in our rotors model is equivalent to the time independent Anderson localization occurring in an L-dimensional disordered lattice. This result, valid for each $L \geqslant 3$, has given generality to our exact-diagonalization calculations relative to the case $L = 3$. Note that interactions play a fundamental role in determining the structure of the lattice in the time-independent model. By setting interactions to zero the procedure described by the mapping can in principle still be applied: nevertheless, in this case the time independent model would not describe the hopping of a particle in an L-dimensional lattice, but rather L copies of a particle hopping in a one dimensional disordered lattice. A first issue which could be investigated as a prosecution of this work is a deeper analysis of the mapping for individuating the critical kick strength at which the transition takes place. Moreover, this procedure may be extended to different periodically driven models to test the existence of a localized phase. Indeed, the key ingredients which need to be verified are the presence of a random, or proper quasi random, local disorder and a short-range hopping term: their computation does not require the full diagonalization of the Hamiltonian and therefore it may constitute a valid starting point for a general understanding of the dynamical propertis of the model.

The study of the dynamical phases of the coupled kicked rotor model, predicted by the mapping, has been the focus of the rest of our work. Different quantities have been used for determining the localized phase and the corresponding results have been found in agreement among each other: focusing on a parameters interval in which the averaged level spacing ratio satisfies $\langle r \rangle \simeq r_{POI}$ we have observed that the IPR is independent on the local truncation. Accordingly, the exact dynamics has showed that the kinetic energy reaches a saturation value. The non thermal behavior of the system in this phase has been investigated by checking the ratio between the diagonal ensemble expectation value of the kinetic energy and its microcanonical average. The ratio of these two quantities, far from being equal to one, decreases as a power law as the Hilbert space dimension is increased: recalling that according to ETH, it is

instead expected to be equal to one, we have proven that the ETH assumptions are violated. Although this investigation has been carried out for $L = 3$ an interval in which $\langle r \rangle \simeq r_{POI}$ has been found also for larger values of L; nevertheless numerical limitations to the local truncation have prevented to extend the same analysis to $L > 3$.

The localized phase disappears as the kick parameters are increased and we enter in the delocalized phase, as we have shown in Chapter 3. The first signature revealing the presence of the different phase has been $\langle r \rangle \simeq r_{GOE}$. At the same time we have observed a power law scaling of the IPR with the Hilbert space dimension and an unbounded growth of the kinetic energy. Surprisingly, the analysis of these quantities has revealed a non-trivial behavior of the system in the delocalized phase. In agreement with other recent results [144, 145, 146, 138, 139, 64] we have found that far from being trivial and structureless, the delocalized phase is characterized by peculiar properties: they can help us understand thermalization process and ergodicity in non-integrable quantum systems. To this purpose, we have first investigated the behavior of the delocalized system far from the transition line in the parameters space. We have found that, for $L = 3$, the system is thermal and ergodic: the expectation value of the kinetic energy computed via the diagonal ensemble tends to the microcanonical, infinite temperature one as the parameters are increased. Then we have studied the structure of the Floquet eigenstates in order to investigate the ergodicity of the system: the averaged IPR scales inversely with the dimension of the Hilbert space, revealing that the system is ergodic [95].

A remarkable result has been found instead close to the transition line: indeed we have shown that anomalous thermalization signatures emerge. The anomalous ergodicity appears from the scaling of the IPR: it obeys a power law with an exponent $\delta_2 < 1$, indicating a multi-fractal structure of the Floquet eigenstates. The analysis of the distribution of the inverse participation ratios of the eigenstates has revealed that their behavior is not homogeneous, due to the presence of power law tails in their distributions (see Figure 3.12). This feature disappears by increasing the values of the parameters, restoring the ergodicity of the system. The anomalous thermalization manifests itself in the ratio between the diagonal and microcanonical expectation values of the kinetic energy, which is less than one. This result is related to the previous one, but we prefer to distinguish them: let us remark that in fact the anomalous structure of the eigenstates is responsible not only for the infinite time dynamics, namely the thermalization process, but it may also exhibit some effects at intermediate times.

Indeed, a peculiarity that we have found in the dynamics in our model is a sub-diffusive growth of the kinetic energy: we have observed it for different values of the interaction strengths in a region adjacent the transition line. Although we do not have found yet a precise explanation for this observation, we have shown that it emerges in the same region in which anomalous ergodicity is observed. In particular, the power law exponent α increases with the interaction strength and remain constant changing the kick parameter K. In order to investigate a possible connection between the structure of the eigenstates and this power law growth we have computed the distribution of the off diagonal matrix elements of the kinetic energy operator. We have found that the distribution is not Gaussian; moreover, it tends to a Gaussian one as $\alpha \to 1$. Further research is needed for a complete understanding of this phenomenon but nev-

ertheless we remark that this work may offer the possibility to relate the definition of quantum ergodicity to the intermediate time dynamics of a system and not only to its infinite time ones. Moreover, the study of the interface between the localized and the delocalized phase presents several connection to different quantum model: from the above mentioned anomalous thermalization works [138, 139, 64], to recent ones concerning the observation of a localized phase in disorder-free systems [147, 148]. The study of the transition from localized to delocalized phases in finite size systems is also related to the possibility to shed a light on the quantum-to-classical transition in chaotic systems. Indeed there is no a clear answer to the question if a KAM-like threshold can be found in quantum systems [20]; also, it would be remarkable to connect the subdiffusive power law that we have observed in the coupled rotors, or similar phenomena in different quantum models, to the Arnold diffusion observed in quasi-integrable classical systems with $N > 2$ degrees of freedom in the proximity of the regular-to-chaotic transition.

The results illustrated so far refer to the case $L = 3$. We have continued our analysis in order to investigate the case of larger values of L. From the analysis of the average level spacing ratio we have found that the localized region disappears as L is increased, confirming similar results found also in a different model [148]. In our case, the explanation has been provided by an extension of the mapping to the case $L \to \infty$ [63]; moreover, this result has been confirmed by a mean field analysis of the model in its fully connected version. We have shown that dynamical localization is absent but, remarkably, the kinetic energy growth is subdiffusive, similarly to the one observed with $L = 3$. An analysis of the system in the case $L > 3$ has been carried out via exact diagonalization in the attempt to connect the subdiffusive behaviors observed with the mean field and in the case $L = 3$. The subdiffusive energy growth has been directly observed only for $L = 4$. Nevertheless it has been possible to study the ergodicity and the thermalization of the system up to $L = 8$ by focusing on the distributions of the matrix elements of the kinetic energy operator. We have analyzed two specific cases: in the first we expected to find an ergodic behavior and ETH. In the second instead we have observed anomalous signatures thermalization and ergodicity. In particular in this last case we have observed non-Gaussian distributions both for the diagonal and off-diagonal matrix elements of the kinetic energy operator: remarkably, these distributions coincide at different values of L. Moreover, we have checked the scaling of the fluctuations by varying L: the scaling of variance is slower than the one predicted by ETH ($\sigma \sim 1/\sqrt{\dim\mathcal{H}}$) and thus reveals a regime of anomalous thermalization. This result completes the observation of the non-Gaussian distributions already discussed in the case $L = 3$. Since we have not proven a relation between these anomalous distributions and the subdiffusive power law we cannot state that the slow heating regime survives in the limit of large L. Nevertheless these observations reveal the persisting of some anomalous features even in the limit in which the transition from localization to delocalization disappears: the interpretations of these features will be object of further research.

A final remark concerns a possible experimental realization of our model. The long-time coherent dynamics of our coupled rotors model can be realized in the framework of ultracold atoms in optical lattices [149, 150, 151] and superconducting quantum circuits [152]. Although a pulsed field can be realized in single-particle models [112], pulsed interactions are not easy to engineer. Nevertheless, as well as the single rotor

case the localization physics does not change when a sinusoidal driving is applied [153] we suggest to replace pulsed interactions with modulated ones. Indeed, driven short range interactions can be engineered by means of Feschbach resonances in the ultracold atoms framework, and through SQUIDS in a time-dependent magnetic field in the case of superconducting circuits. We hope that these results may contribute to provide a general characterization of the anomalous ergodic behavior of delocalized systems in the proximity of a localization–delocalization transition, both at intermediate as well as at infinite times.

Appendix A

Classical coupled kicked rotors

In this Appendix we discuss the behavior of the classical counterparts of the model defined in Eq. (4.1.1). We indicate the angle and momentum variables relative to the i rotor at time n as $\{\theta_i^n, p_i^n\}$.

A useful frame for understanding the dynamics of our models is provided by the seminal work of Nehkhoroshev (see Ref. [122]) and other works (see Refs. [118, 119]) about the classical dynamics of our system. For reader's convenience we review some known results and apply them to our models.

The kicked rotor model Hamiltonian can be written as

$$H = H_0(\theta, p) + K\, H_I(\theta, p; t) \tag{A.1}$$

where H_0 is an integrable Hamiltonian and H_I breaks the integrability of the system with a strength given by K. It is relevant that both H_0 and H_I are periodic in θ.

For a system with two degrees of freedom, like the single rotor, we have seen in Section that for $K < K_c$ there are regions in the phase space in which the trajectories keep being closed (this result is in agreement with the KAM theory, as discussed in Section 2.1. The phase space is therefore divided in several regions by these trajectories and the dynamics of the system is not ergodic. The system exhibits, as already discussed, classical dynamical localization.

Nekhoroshev's theorem deals with the dynamics of a system with an Hamiltonian like the one defined in Eq. A.1 with more than two degrees of freedom. It states that, given an initial condition for the momentum variables $\{p_i^0\}_{1 \leqslant i \leqslant N}$, one finds [118]

$$||\mathbf{p}^n - \mathbf{p}^0|| < K^\alpha \tag{A.2}$$

for $n < n^*$. We have $n^* \sim 1/K \exp\{1/K^\beta\}$, $\beta \sim 1/(\text{polynomial function of } N)$ and $\alpha > 0$. This is the same mechanism which allows the orbits of planets to remain stable in very long times: this should emphasize that if $K \ll 1$ the time during which condition in Eq. (A.2) is satisfied can be very long. After this time the trajectories of the system become unstable: their localization in the phase space is broken and the dynamics becomes ergodic.

For time independent Hamiltonians this means that the trajectories span the whole energy shell: averages can be computed using the micro-canonical ensemble.

For a time dependent Hamiltonian, the energy is not conserved and thus the trajectories will spread in all the phase space. This means that the system heats

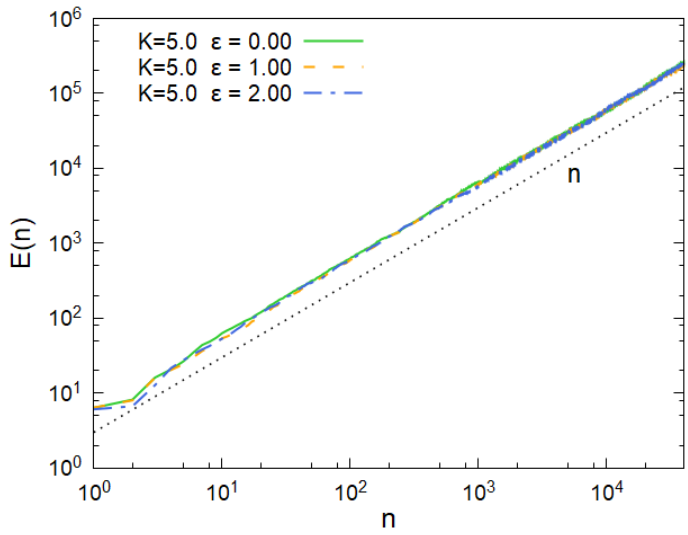

Figure A.1: The time evolution of $E(n)$ is plotted together with the curve n as a guide to the eye to show the diffusive growth of the kinetic energy of the system. The diffusion coefficient is $D_{class} \sim K^2/4 = 6.25$: this is the expected value for the single kicked rotor and it is the same for all the values of J, since the curves are superposed. $N_{rotors} = 100$ in the simulations.

without a bound and thermalizes at $T = \infty$: this is indeed the case of our system, in which the kick breaks the integrability of the Hamiltonian.

Now we numerically check this delocalization process for the two cases we are studying, the long range and the short range interacting ones. Since we are interested in the dynamics at long times we choose amplitudes of the kick (namely the parameters K and J in Hamiltonian of (Eq. 2.21) for which the time n^* is negligible.

We focus on the classical dynamics in the case of infinite-range interactions. It is possible to integrate exactly the Hamilton equations for each rotor over a period, and obtain a map for the stroboscopic evolution of the system: restricting to discrete times $t_n = n$ we have

$$p_i^{n+1} = p_i^n + \left[K \sin\theta_i^n - \frac{J}{(N-1)} \sum_{j \neq i} \sin(\theta_i^n - \theta_j^n) \right], \tag{A.3}$$

$$\theta_i^{n+1} = \theta_i^n + p_i^{n+1}. \tag{A.4}$$

We consider many realizations of the dynamics of the system sampling different initial conditions; they are chosen giving a uniformly random angle to each rotor and setting $p_i^0 = 0 \ \forall i = 1...N$. We focus on the time-evolution of the kinetic energy per rotor averaged over the ensemble of the initial conditions

$$E(n) = \frac{1}{2N} \sum_{i=1}^{N} \overline{(p_i^n)^2}\,. \tag{A.5}$$

This quantity is proportional to the variance of the momenta distribution in time and then gives information on the spreading in time of this distribution.

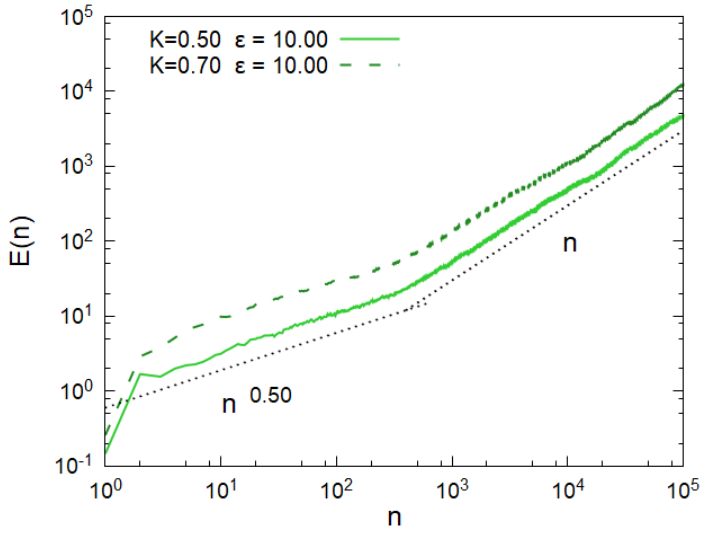

Figure A.2: The time evolution of $E(n)$ is plotted; the two regimes, the subdiffusive and diffusive one, are clearly distinguishable in the log-log scale. $N_{rotors} = 100$ in the simulations.

In the numerical simulations that follow we set $N = 100$: this number of rotors is sufficient to avoid boundary effects and simulate the $N \to \infty$ limit.

In the ergodic regime the time and space correlations between the angles of the rotors rapidly decay to zero (as it always occurs in chaos [154, 155]): this implies in particular that

$$\langle \cos(\theta_i^n - \theta_j^n) \cos(\theta_{i'}^m - \theta_{j'}^m) \rangle = \frac{1}{2} \delta_{n\,m} (\delta_{i\,i'} \delta_{j'\,j} + \delta_{i\,j'} \delta_{i'\,j}), \tag{A.6}$$

where the average is taken over the ensemble of the initial conditions. Now we consider the following expression for the momentum at time n

$$p_i^n = \sum_{\tau=0}^{n-1} \left[K \sin\theta_i^\tau - \frac{J}{(N-1)} \sum_{j \neq i} \sin(\theta_i^\tau - \theta_j^\tau) \right]. \tag{A.7}$$

By squaring it and using Eq. A.6 we obtain the following coefficient describing the linear increase of the kinetic energy for the long-range interacting model:

$$D_{lr} = \frac{1}{4} \left(K^2 + \frac{J^2}{N-1} \right). \tag{A.8}$$

Note that for $N \gg 1$ the diffusion coefficient coincides with the single-rotor one for $K > K_c$. In Figure A.1 this property is clearly shown: $E(n)$, computed at fixed $K = 5.0$ but different values of $J = 0, 2.5, 5$, always shows the same behaviour, growing linearly in time with the same angular coefficient.

A remarkable difference emerges for $K < K_c$: in this case the single rotor manifests dynamical localization, while the presence of an interaction induces a growth of the kinetic energy which starts being only subdiffusive and becomes diffusive after

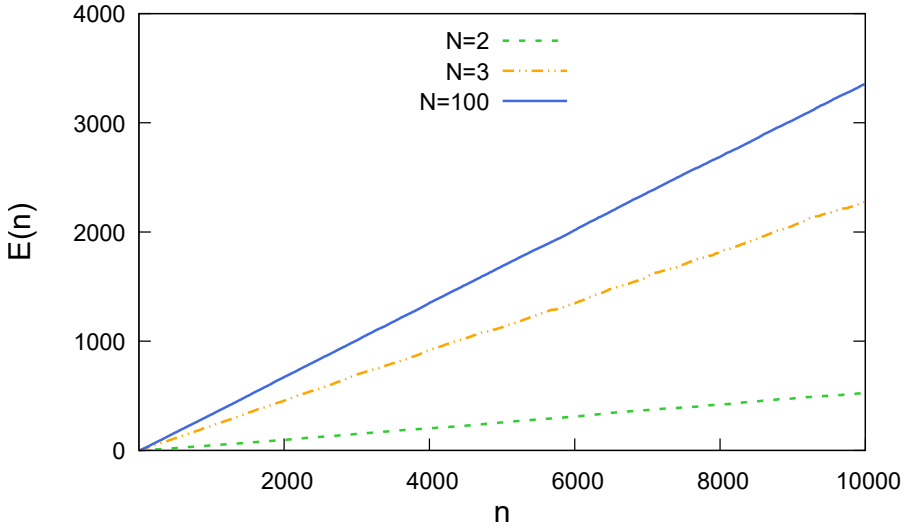

Figure A.3: In this figure the time evolution of $E(n)$ is plotted with $K = 0.5$ and $J = 1$. As the number of rotors is increased the diffusion coefficient grows approaching the asymptotic value ($N = 100$ rotors). Nevertheless the exact value of the diffusion coefficient in Eq. A.9 is reached for $K \gtrsim 2$.

a transient (see Ref. [119] for the same phenomenon in a different model). This behaviour is perfectly consistent with the Nekhoroshev theorem [118] and we show it in Figure. A.2 by plotting the evolution of $E(n)$ for different values of K.

The classical behavior of the short-ranged model is very similar. With analogous calculations we find that the diffusion coefficient for the kinetic energy, in absence of correlations and with $N \to \infty$, is

$$D_{sr} = \frac{1}{4}\left(K^2 + \frac{J^2}{2}\right) . \tag{A.9}$$

With small N (like the cases $N = 2, 3$ we consider in the text for the quantum model) finite size effects [118] reduce the diffusion coefficient as it is shown in Figure A.3. Moreover, some corrections due to correlations modify the diffusion coefficient, as it has been seen in Ref. [125] for two rotors; they disappear for $J \gtrsim 2$.

To conclude, we have shown that a classical interacting rotors model exhibits an ergodic behavior and, at long times, a linear growth of the kinetic energy: this characteristic is manifested for all the values of K and J, independently from the number of rotors.

Appendix B

Exact diagonalization code

In this Appendix we describe the steps of the exact diagonalization code.

States counting

Suppose we have L sites and each site can be in one of M possible states: the total Hilbert space has dimension $D = M^L$.

We have to define and assign an order to the M^L states. We work in the angular momentum basis in which a global state is characterized by the local state on each site: we have that the mth state is $|m\rangle \equiv (m_1, m_2, ...m_L)$ and its position is

$$m = \sum_{i=0}^{L-1} m_{i+1}\, M^i, \tag{B.1}$$

namely the configuration of the mth state is given by its decomposition in the M-basis. This choice provides an immediate way to compute the matrix elements corresponding to the single and interaction kick. Indeed, we want to compute the states resulting from a kick applied the jth rotor, starting from the state $|m\rangle$. In this case the local basis is the momentum basis and the integer-valued momentum assigned to each state is

$$\hat{m}_j|m_j\rangle = ((1-M)/2 + m_j)|m_j\rangle. \tag{B.2}$$

In this basis the $\cos\hat{\theta}_j$ operator is represented as

$$\cos\hat{\theta}_j = \frac{1}{2}\sum_{m=-\infty}^{+\infty}(|m\rangle\langle m+1|_j + |m+1\rangle\langle m|_j). \tag{B.3}$$

it follows that applying the operator $\cos\hat{\theta}_j$ the state $|m\rangle$ is transformed in two states with identifying numbers n^+ and n^- such that, in principle, the components of the jth site will be respectively $n_j \pm 1$. Due to the choice made in eq.(B.1) we have that

$$m^{+(-)} = m \pm M^{j-1}. \tag{B.4}$$

Note that if m_j is zero $(M-1)$ the numbers $n^{-(+)}$ don't correspond to any state of the Hilbert space. With this procedure the hopping elements can be computed with DM operations plus an initial normalization instead of D^2 necessary to find all the

correspondences between the states. Moreover there is no need to keep track of the configurations of all the states since they are encoded in the representative number and can be easily computed when needed.

Parity symmetry

Given a state $|n\rangle$ and its local states decomposition $\{n_i\}_{1\leqslant i\leqslant N_{rot}}$ the inversion of the momentum on each sites corresponds to the local transformation

$$n_i \to d - n_i \,. \tag{B.5}$$

This means that

$$\hat{P}|n\rangle = |n'\rangle \equiv |D-1-n\rangle \,. \tag{B.6}$$

It follows that the states labeled with $n \in [0,(D-1)/2]$ are connected to the following ones via the action of $\hat{P}$ and connected states are symmetrically ordered. Of course $\hat{P}^2 = \mathbf{1}$, therefore a basis diagonal under $\hat{P}$ can be built by taking

$$|v_\alpha\rangle = \frac{1}{\sqrt{2}}(|n\rangle \pm \hat{P}|n\rangle). \tag{B.7}$$

The Hamiltonian can be computed directly in this basis by observing that, if $|n'\rangle = \hat{H}|n\rangle$ also $\hat{P}|n'\rangle = \hat{H}\hat{P}|n\rangle$ since $[\hat{H},\hat{P}] = 0$. It will be sufficient to compute how $\hat{H}$ acts on the first $M = D/2+1$ states of the initial basis to know the action of the symmetrized vectors $|v_\alpha\rangle$.

The idea is that each basis vector $|v\rangle$ in the symmetric subspace of the parity operator can be written as

$$|v\rangle = |n\rangle + \hat{P}|n\rangle, \tag{B.8}$$

with $n \leqslant M$. It follows that, given two eigenstates of $\hat{P}$ $|v_\alpha\rangle$ and $|v_\beta\rangle$, we can find $n, m < M$ such that $|v_\alpha\rangle = (|n\rangle + \hat{P}|n\rangle)/\sqrt{2}$ and $(|v_\beta\rangle = |m\rangle + \hat{P}|m\rangle)/\sqrt{2}$. What follows is that

$$H_{\alpha\beta} = \langle v_\alpha|\hat{H}|v_\beta\rangle = \langle n|\hat{H}|m\rangle. \tag{B.9}$$

From a practical point of view for each state $|n\rangle$ we compute the outcoming vectors and their identifying numbers automatically return the indexes of the nonvanishing matrix elements. We must also take into account the possibility that $|n'\rangle = \hat{H}|n\rangle$ and $n' > M$: in this case it will exist a vector $|\tilde{n}'\rangle$ such that $\hat{P}|\tilde{n}'\rangle = |n'\rangle$ and the corresponding matrix element to be considered will be $H_{\tilde{n}'n}$, with $\tilde{n}' = D - n'$.

A very last issue is related to the normalization of the states, since Eq. B.9 holds only if the two states have the same normalization factor. The only case in which this condition is not valid is if one of the two is a state parity invariant $|n*\rangle = \hat{P}|n*\rangle$. In this case we have

$$H_{\alpha\,\beta} = \sqrt{2}H_{m\,n*} \,. \tag{B.10}$$

Translational symmetry

Here we explain a way to reduce the Hamiltonian matrix to a subspace given by a set of degenerate eigenstates of the translation operator $\hat{T}$. The method consists in defining the isometry transforming the total Hilbert space $\mathcal{H}$ in $\mathcal{H}'$ with a dimension $D' < D$.

In particular, we will explain how to write the matrix, hereafter called $\hat{V}$, through which this isometry can be implemented. The matrix $\hat{V}$ is a $D \times D'$ dimensional one in which each column corresponds to an eigenstate of the $\hat{T}$ for a fixed, degenerate eigenvalue.

The eigenvalue that we consider is $\lambda_{\hat{T}} = 1$ (or, equivalently, the zero momentum mode) since it offers a direct way to find the eigenvectors, avoiding the diagonalization of the translation operator matrix. Indeed, given a state $|n\rangle$ in the canonical base of the local states we can build what is called an invariant M-cycle $|v\rangle$ as

$$|v\rangle = \frac{1}{\mathcal{N}} \sum_{i=0}^{M-1} \hat{T}^i |n\rangle \tag{B.11}$$

where $\mathcal{N}$ provides the proper normalization and M is such that $\hat{T}^M = |n\rangle$. Observe that $M \leqslant L$ and $\mathcal{N} = \sqrt{M}$.

Eq. (B.11) provides a direct way for computing the desired eigenstates of the translation operator: one simply has to generate the invariant cycles starting from the canonical basis vectors $|n\rangle$ skipping during this operation the states already included in a cycle.

This symmetry can be joined with the parity symmetry explained in the previous paragraph: in this case, with the same exact procedure, one generates the invariant cycles involving the parity-symmetrized states defined in Eq. (B.7). As discussed for the Hamiltonian matrix elements, one build the cycle just looking at the vector with $n \leqslant (D+1)/2$ and considering the symmetric state $\tilde{n} = D - 1 - n'$ if for some i it should happen $T^i|n\rangle = n'$ with $n' > (D+1)/2$.

A fast way of obtaining the translated states comes by remembering that a state $|n\rangle$ is identified, in its local representation, by the decomposition in the d-dimensional basis. If $|n\rangle \equiv (n_0, n2, ...n_{L-1})$ it follows that

$$\hat{T}|n\rangle = (n_{L-1}, n_0, n2, ...n_{L-2}) = |n'\rangle \tag{B.12}$$

with

$$n' = n_{L-1} + \sum_{i=0}^{N-2} n_i \, d^{i+1}. \tag{B.13}$$

We have that

$$n' = n_{L-1} + d(n - d^{L-1}(n \operatorname{div} d^{L-1})). \tag{B.14}$$

The advantage of this method is that the translated state can be computed with a fixed number of operations, independent on the size of the system and the full configuration is not required.

Inversion symmetry

The Hamiltonian also present a symmetry under the spatial inversion operation $\hat{I}$. Since the inversion operator commute with the operator $\sum_{i=0}^{L-1} \hat{T}^i$ it follows that in the zero momentum mode of the translation operator also this symmetry must be taken into account.

Charge conservation

If $K = 0$ the total momentum of the system, called P_{tot}, is conserved. From a computational point of view it means that given a state in the local momentum basis $|n\rangle \equiv (n_0, n2, ...n_{L-1})$ the subspace to be considered is the one whose states satisfy the condition

$$\sum_{i=0}^{L-1} n_i = P_{tot} + L\frac{d+1}{2}\,, \tag{B.15}$$

where d is the truncating dimension of the local Hilbert space (remember that $n_i = 0$ corresponds to a local momentum value $m_i = -(d-1)/2$).

Appendix C

Absence of localization in a infinite dimensional lattice

The result presented in this Appendix has been obtained by Angelo Russomanno. We show that an infinite dimensional disordered lattice is expected to never exhibit Anderson localization. To this purpose we use the scaling theory of localization introduced in Ref. [62] which we briefly summarize to fix the notation. Consider a N dimensional system with conductivity σ and linear size L and focus on the properties of the dimensionless conductance $g = \frac{\hbar}{e^2} L^{N-2}\sigma$. We make the assumption that g only depends on the scale L at which the system is probed and on the dimensionality N and we start at some scale L_0 where the dimensionless conductivity is g_0: we see how g flows as L is increased. For that purpose it is crucial to focus on the properties of the logarithmic derivative $\beta(g) \equiv \frac{\mathrm{d}\log g}{\mathrm{d}\log L}$ and in particular on its dependence on g: knowing the form of $\beta(g)$ and integrating this flow equation, the bulk behavior for $L \to \infty$ is obtained. It is possible to find the behavior of $\beta(g)$ in the limits $g \ll 1$ and $g \gg 1$. When $g \ll 1$ there is Anderson localization, and the conductance obeys the law $g(L) \sim A\mathrm{e}^{-L/\xi}$ for some localization length ξ: this relation implies

$$\beta(g) = \log g + \text{const}\,. \tag{C.1}$$

In this limit, $\beta(g)$ versus $\log g$ is a line whose slope is independent of the localization length and equals 1. In the opposite limit of $g \gg 1$ there is Ohmic conductivity, σ does not depend on L and $\beta(g) = N - 2$. The question is how to interpolate between these two limits. One can show [62, 156, 157] that, because of the quantum corrections to the Ohm's law, in the limit of large g it is

$$\beta(g) \simeq N - 2 - \frac{C(N)}{g}\,, \tag{C.2}$$

for some $C(N)$ depending on the dimension. Connecting this large-g behavior with the small-g linear one Eq. (C.1) in a continuous and derivable way, one gets a $\beta(g)$ which is always monotonously increasing. (The physical assumption behind this connection is that at some point the "weak localization" due to the quantum corrections to the Ohm's law becomes the strong Anderson localization). Therefore, we always have $\frac{\mathrm{d}\beta(g)}{\mathrm{d}\log g} > 0$. This gives rise to interesting consequences. For $N \leqslant 2$ we find as a consequence that $\beta(g) = \frac{\mathrm{d}\log g}{\mathrm{d}\log L} < 0$ for all g: when larger and larger values of L

are considered, whichever are the initial values L_0 and g_0, they always flow towards small values of g, the ones corresponding to Anderson localization. If instead $N > 2$, there is some value g_N^* where $\beta(g_N^*) = 0$. For $g > g_N^*$ we have $\beta(g) > 0$ and $g < g_N^*$ implies $\beta(g) < 0$. Therefore, if $g_0 < g_N^*$ the system flows towards small values of g for $L \to \infty$ and there is Anderson localization in the bulk; if instead $g_0 > g_N^*$ the flow moves towards large values of g and there is an Ohmic behavior. Therefore for $N > 2$, the bulk of the system undergoes a localization/delocalization transition. We have observed exactly this phenomenon in Section **??** for the model with three rotors mapped over the $N = 3$-dimensional disordered lattice Eq. (3.1.3): in this case K played the role of g_0. Now we would like to explore the behavior of g_N^* in the limit $N \to \infty$. To that purpose, we study the behavior of the conductivity: its quantum corrections to the Ohmic behavior are [156, 157]

$$\begin{aligned} \delta\sigma(L) &= -\frac{e^2}{\pi\hbar}\int_{1/L}^{1/l}\frac{\mathrm{d}^N Q}{(2\pi)^N}\frac{1}{Q^2} \\ &= -\frac{2e^2}{\pi\hbar(2\pi)^N}\frac{S_{N-1}}{N-2}\left(\frac{1}{l^{N-2}} - \frac{1}{L^{N-2}}\right), \end{aligned} \tag{C.3}$$

where

$$S_{N-1} = \frac{2(\pi/2)^{N/2}}{\Gamma(N/2)} \tag{C.4}$$

is the measure of the $N-1$-dimensional unit sphere and l is the classical mean-free-path in the disordered potential (its precise value is not important because it will disappear in the next formulae). Using that $g(L) = \frac{\hbar}{e^2}L^{N-2}(\sigma(\infty) + \delta\sigma(L))$, we easily find that $\beta(g)$ has the form given in Eq. (C.2) with

$$C(N) = \frac{(\pi/2)^{N/2}}{(2\pi)^N\Gamma(N/2)}\,. \tag{C.5}$$

Connecting Eq. (C.2) in a continuous and derivable way with the Anderson-localized behavior Eq. (C.1) valid at small g, we find that the critical value g_N^* is given by

$$\log g_N^* = -N + 3 + \log\left(\frac{2}{\pi}\frac{1}{(2\sqrt{2\pi})^N}\frac{1}{\Gamma(N/2)}\right), \tag{C.6}$$

for N large enough. For $N \gg 1$, using the Stirling approximation for the Gamma function, we find

$$\begin{aligned} \log g_N^* &= -N + 3 + \log(2/\pi) - N\log(2\sqrt{2\pi}) \\ &- \left(\frac{N}{2}+1\right)\left[\log\left(\frac{N}{2}+1\right) - 1\right]. \end{aligned} \tag{C.7}$$

Appendix D

Exactness of the mean field approach in the fully connected model

In this Appendix we demonstrate that $\langle\hat{\delta}_r\hat{\delta}_s\rangle \to 0$ in the limit $L \to \infty$ if we start from a separable state at time $n = 0$. We first observe that $\langle\hat{\delta}_r\hat{\delta}_s\rangle = c(r, s; n)$, where

$$c(r, s; n) = \langle\cos\hat{\theta}_r(n)\cos\hat{\theta}_s(n)\rangle - \langle\cos\hat{\theta}_r(n)\rangle\langle\cos\hat{\theta}_s(n)\rangle. \tag{D.1}$$

is the time dependent, spatial connected correlator between different rotors. Therefore the relation $\langle\hat{\delta}_r\hat{\delta}_s\rangle \to 0$ for $L \to \infty$ means that the system does not develop spatial correlation during the evolution in the thermodynamic limit.

We set $\hbar = 1$; for simplicity we define $\alpha = \epsilon K/(L-1)$ and then we set $K = 0$: without losing generality we are considering only the interacting part in the kick.

The scheme of the demonstration is the following: we expand the term $\langle\cos\hat{\theta}_r(n)\cos\hat{\theta}_s(n)\rangle$ keeping the ones which are $O(1/L)$. Some of the resulting terms are canceled out by $\langle\cos\hat{\theta}_r(n)\rangle\langle\cos\hat{\theta}_s(n)\rangle$: we show that only a finite number of terms $O(1/L)$ remains: therefore, they vanish in the thermodynamic limit.

Once we have demonstrated the absence of spatial correlations we define the operator $\hat{\Delta}_L = 1/(L-1)\sum_{r\neq s}\hat{\delta}_r\hat{\delta}_s$: it is the sum of fluctuation terms which appears in Eq. (4.1.5). By applying the central limit theorem we show that it increases in a non extensive way. Therefore, it brings negligible contributions to the Hamiltonian in the thermodynamic limit.

As a first step we introduce some notation useful for the demonstration: we write the one-period propagator as $\hat{U} = \hat{K}\,\hat{T}$, with $\hat{K}$ containing the kick part of the propagator and $\hat{T}$ the kinetic one. We define $\hat{K}_r = \mathrm{e}^{i\alpha\sum_{s\neq r}\cos(\hat{\theta}_r-\hat{\theta}_s)}$ and $\hat{T}_r = \mathrm{e}^{i\frac{\hat{p}_r^2}{2}}$. We have $[\hat{T}_r, \hat{T}_s] = [\hat{K}_r, \hat{K}_s] = 0\ \forall\, r, s$; also,

$$\mathcal{C}_{1,2}(\hat{\theta}_r, \hat{\theta}_s, \hat{p}_r) = \pm[\mathrm{e}^{\mp i\alpha\cos(\hat{\theta}_r-\hat{\theta}_s)}, \mathrm{e}^{\mp i\frac{\hat{p}_r^2}{2}}]\,. \tag{D.2}$$

These commutators are bounded operators, since they come from unitary operators. Moreover, one can easily deduce that $||\mathcal{C}_{1,2}(\hat{\theta}_r, \hat{\theta}_s, \hat{p}_r)|| \sim 1/(L-1)$ from a first order expansion of $\mathrm{e}^{\mp i\alpha\cos(\hat{\theta}_r-\hat{\theta}_s)}$. In the next subsection we go through the expansion of the term $\langle\cos\hat{\theta}_r(n)\cos\hat{\theta}_s(n)\rangle$.

Expansion of $\langle \cos\hat{\theta}_r(n)\cos\hat{\theta}_s(n)\rangle$

Given the initial factorized state $|\Psi_0\rangle$ the expectation value of the product at time $n=2$ is given by

$$\langle\Psi_0|\left[(U^\dagger)^2\cos\hat{\theta}_r\,U^2\right]\left[(U^\dagger)^2\cos\hat{\theta}_s\,U^2\right]|\Psi_0\rangle\,. \tag{D.3}$$

The choice of $n=2$ is motivated by the fact that at this time correlations start to develop. We focus on the content of the left squared brackets. First, we write $\hat{U}$ and $\hat{U}^\dagger$ by using the definition given above. Then we simplify all the terms which freely commute and what remains is the following:

$$\hat{T}^\dagger\,\hat{K}_r^\dagger\,\hat{T}_r^\dagger\,\cos\hat{\theta}_r\,\hat{T}_r\,\hat{K}_r\,\hat{T} \tag{D.4}$$

The kinetic operator $\hat{T}^\dagger$ on the right automatically simplifies with the relative term $\hat{T}$ in the right squared brackets so we neglect it. Also, we define $|\tilde{\Psi}_0\rangle=\hat{T}|\Psi_0\rangle$ so we can restrict our study to the term $\hat{K}_r^\dagger\,\hat{T}_r^\dagger\,\cos\hat{\theta}_r\,\hat{T}_r\,\hat{K}_r$. In order to expand this term we need to invert the operators $K_r^\dagger\,\hat{T}_r^\dagger$ and $\hat{T}_r\,\hat{K}_r$ respectively, so we need to compute the two commutators $[\hat{K}_r^\dagger,\hat{T}_r^\dagger]$ and $[\hat{T}_r,\hat{K}_r]$.

For the first commutator we have (we consider $r=L$ for simplicity but the generalization is straightforward):

$$\begin{aligned}[\hat{K}_L^\dagger,\hat{T}_L^\dagger] &= \mathcal{C}_1(\hat{\theta}_L,\hat{\theta}_n,\hat{p}_L)\prod_{\nu=1}^{L-2}\mathrm{e}^{-i\alpha\cos(\hat{\theta}_L-\hat{\theta}_\nu)}+ \\ &\sum_{n=1}^{L-2}\left[\left(\prod_{\nu=1}^{n}\mathrm{e}^{-i\alpha\cos(\hat{\theta}_L-\hat{\theta}_\nu)}\right)\mathcal{C}_1(\hat{\theta}_L,\hat{\theta}_n,\hat{p}_L)\left(\prod_{\mu=n+1}^{L-2}\mathrm{e}^{-i\alpha\cos(\hat{\theta}_L-\hat{\theta}_\mu)}\right)\right].\end{aligned} \tag{D.5}$$

Also, for each term in the sum labeled by n we have:

$$\begin{aligned}&\left(\prod_{\nu=1}^{n}\mathrm{e}^{-i\alpha\cos(\hat{\theta}_L-\hat{\theta}_\nu)}\right)\mathcal{C}_1(\hat{\theta}_L,\hat{\theta}_n,\hat{p}_L) \\ &=\left(\prod_{\nu=1}^{n-1}\mathrm{e}^{-i\alpha\cos(\hat{\theta}_L-\hat{\theta}_\nu)}\right)\left(\mathcal{C}_1(\hat{\theta}_L,\hat{\theta}_n,\hat{p}_L)\mathrm{e}^{-i\alpha\cos(\hat{\theta}_L-\hat{\theta}_n)}+\xi_1(\hat{\theta}_L,\hat{\theta}_n,\hat{p}_L)\right) \\ &=\mathcal{C}_1(\hat{\theta}_L,\hat{\theta}_n,\hat{p}_L)\left(\prod_{\nu=1}^{n}\mathrm{e}^{-i\alpha\cos(\hat{\theta}_L-\hat{\theta}_\nu)}\right)+\sum_{\nu=1}^{n}\left(\xi_1(\hat{\theta}_L,\hat{\theta}_\nu,\hat{p}_L)\prod_{\mu\neq\nu}^{n}\mathrm{e}^{-i\alpha\cos(\hat{\theta}_L-\hat{\theta}_\mu)}\right) \\ &\quad+O(1/L^2),\end{aligned} \tag{D.6}$$

where

$$\xi_{1,2}(\hat{\theta}_r,\hat{\theta}_s,\hat{p}_r)=\pm[\mathrm{e}^{\mp i\alpha\cos(\hat{\theta}_r-\hat{\theta}_s)},\mathcal{C}_{1,2}]\,. \tag{D.7}$$

Note that $\xi_{1,2}$ is an operator whose norm is $O(1/L^2)$. The $O(1/L^2)$ terms in the last equation come from higher order commutators and we henceforth neglect them. Therefore Eq. (D.5) can be rewritten as follows:

$$[\hat{K}_L^\dagger,\hat{T}_L^\dagger]\simeq\sum_{n=1}^{L-1}\left[\mathcal{C}_1(\hat{\theta}_L,\hat{\theta}_n,\hat{p}_L)+\sum_{\nu=1}^{n}\xi_1(\hat{\theta}_L,\hat{\theta}_\nu,\hat{p}_L)\right]\hat{K}_L^\dagger, \tag{D.8}$$

An analogous result can be obtained for the commutator $[\hat{T}_L, \hat{K}_L]$:

$$[\hat{T}_L, \hat{K}_L] \simeq \hat{K}_L \sum_{n=1}^{L-1} \left[\mathcal{C}_2(\hat{\theta}_L, \hat{\theta}_n, \hat{p}_L) + \sum_{\nu=1}^{n} \xi_2(\hat{\theta}_L, \hat{\theta}_\nu, \hat{p}_L) \right]. \tag{D.9}$$

The important point of Equations (D.8) and (D.9) is that the commutators can be written as the sum of $L-1$ terms of order $1/(L)$ and $(L-1)^2/2$ terms of order $O(1/L^2)$, up to higher order terms.

Now we can factorize the term $\hat{K}_r^\dagger \hat{T}_r^\dagger \cos\hat{\theta}_r \hat{T}_r \hat{K}_r$ by using Equations (D.8) and (D.9):

$$\begin{aligned}
&\hat{K}_r^\dagger \hat{T}_r^\dagger \cos\hat{\theta}_r \hat{T}_r \hat{K}_r \qquad\qquad (D.10)\\
&= \left[\left(\hat{T}_r^\dagger + \sum_{n\neq r} \mathcal{C}_1(\hat{\theta}_r, \hat{\theta}_n, \hat{p}_r) + \sum_{n\neq r\,,\nu=1}^{n} \xi_1(\hat{\theta}_r, \hat{\theta}_\nu, \hat{p}_r) \right) \hat{K}_r^\dagger \right] \\
&\quad \cos\hat{\theta}_r \\
&\quad \left[\hat{K}_r \left(\hat{T}_r^\dagger + \sum_{m\neq r} \mathcal{C}_2(\hat{\theta}_r, \hat{\theta}_m, \hat{p}_r) + \sum_{n\neq r\,,\nu=1}^{n} \xi_2(\hat{\theta}_r, \hat{\theta}_\nu, \hat{p}_r) \right) \right] \\
&= \hat{T}_r^\dagger \cos\hat{\theta}_r \hat{T}_r + \sum_{n\neq r} \mathcal{C}_1(\hat{\theta}_r, \hat{\theta}_n, \hat{p}_r) \cos\hat{\theta}_r \\
&\quad + \cos\hat{\theta}_r \sum_{m\neq r} \mathcal{C}_2(\hat{\theta}_r, \hat{\theta}_m, \hat{p}_r) + \sum_{n\neq r\,,\nu=1}^{n} \xi_1(\hat{\theta}_r, \hat{\theta}_\nu, \hat{p}_r) \cos\hat{\theta}_r \\
&\quad + \cos\hat{\theta}_r \sum_{n\neq r\,,\nu=1}^{n} \xi_2(\hat{\theta}_r, \hat{\theta}_\nu, \hat{p}_r).
\end{aligned}$$

Analogously the right squared brackets term in Eq. (D.3) returns:

$$\begin{aligned}
&\hat{K}_s^\dagger \hat{T}_s^\dagger \cos\hat{\theta}_s \hat{T}_s \hat{K}_s \qquad\qquad (D.11)\\
&= \hat{T}_s^\dagger \cos\hat{\theta}_s \hat{T}_s + \sum_{n\neq s} \mathcal{C}_1(\hat{\theta}_s, \hat{\theta}_n, \hat{p}_s) \cos\hat{\theta}_s + \\
&\quad \cos\hat{\theta}_s \sum_{m\neq s} \mathcal{C}_2(\hat{\theta}_s, \hat{\theta}_m, \hat{p}_s) + \sum_{n\neq s\,,\nu=1}^{n} \xi_1(\hat{\theta}_s, \hat{\theta}_\nu, \hat{p}_s) \cos\hat{\theta}_s \\
&\quad + \cos\hat{\theta}_s \sum_{n\neq s\,,\nu=1}^{n} \xi_2(\hat{\theta}_s, \hat{\theta}_\nu, \hat{p}_s).
\end{aligned}$$

Now we multiply the results in Equations (D.10) and (D.11) keeping explicit only first order terms and take the expectation values. At the zeroth order we have

$$\langle \tilde{\Psi}_0 | \hat{T}_r^\dagger \cos\hat{\theta}_r \hat{T}_r \hat{T}_s^\dagger \cos\hat{\theta}_s \hat{T}_s | \tilde{\Psi}_0 \rangle, \tag{D.12}$$

which represents the evolution without kick and can be factorized. At the first order we have two sums which provide respectively

$$\Sigma_r = \langle \tilde{\Psi}_0 | \hat{T}_r^\dagger \cos\hat{\theta}_r \hat{T}_r \sum_{n\neq s} \left[\mathcal{C}_1(\hat{\theta}_s, \hat{\theta}_n, \hat{p}_s) \cos\hat{\theta}_s + \cos\hat{\theta}_s \mathcal{C}_2(\hat{\theta}_s, \hat{\theta}_n, \hat{p}_s) \right] | \tilde{\Psi}_0 \rangle \tag{D.13}$$

and an analogous term Σ_s is defined. In an analogous way the sums of the second order terms $\Pi_{1,2}$ containing $\xi_{1,2}$ must be considered.

$O(1/L)$ terms in $c(r,s;n)$

We henceforth explain how the extensive sums $\Sigma_{r,s}$ and $\Pi_{1,2}$ reduce to a non extensive amount of contributions in $c(r,s;n)$. We explain the mechanism for $\Sigma_{r,s}$ but it equally apply for the $\Pi_{1,2}$.

We indeed focus on $c(r,s;n)$ and check which terms does not cancel out when we take the difference $\langle \cos\hat{\theta}_r(n)\, \cos\hat{\theta}_s(n)\rangle - \langle\cos\hat{\theta}_r(n)\rangle\langle\cos\hat{\theta}_s(n)\rangle$. Almost all the terms in $\Sigma_{r,s}$ can be factorized and therefore cancel out with equal contributions coming from the product $\langle\cos\hat{\theta}_r(n)\rangle\langle\cos\hat{\theta}_s(n)\rangle$: the only exceptions are two terms with $n=r$ in Σ_r and two with $n=s$ in Σ_s. Indeed we obtain four differences which do not cancel, one of those is

$$\begin{aligned}&\langle\tilde{\Psi}_0|\hat{T}_r^\dagger\, \cos\hat{\theta}_r\, \hat{T}_r\, \mathcal{C}_1(\hat{\theta}_s,\hat{\theta}_r,\hat{p}_s)\cos\hat{\theta}_s|\tilde{\Psi}_0\rangle - \\ &\langle\tilde{\Psi}_0|\hat{T}_r^\dagger\, \cos\hat{\theta}_r\, \hat{T}_r|\tilde{\Psi}_0\rangle\, \langle\tilde{\Psi}_0|\mathcal{C}_1(\hat{\theta}_s,\hat{\theta}_r,\hat{p}_s)\cos\hat{\theta}_s|\tilde{\Psi}_0\rangle\,.\end{aligned} \tag{D.14}$$

The three others terms have the same structure.

Therefore $c(r,s;n=2)$ does not vanish because of a finite number of $O(1/L)$ corrections (now we neglect the $O(1/L^2)$ terms coming from $\xi_{1,2}$): we have found the first contributions in Equations (D.10) and (D.11). Also, we have found the contributions $O(1/L)$ coming from Σ_r and Σ_s. At a time $n>2$ the number of these contributions linearly increases, although it is always finite. Since, anyway, the limit $L\to\infty$ is taken before the evolution starts, the correlations are always going to zero like $1/L$: the final result we obtain is that $\langle\hat{\delta}_r\hat{\delta}_s\rangle \to \langle\hat{\delta}_r\rangle\langle\hat{\delta}_s\rangle$ in the thermodynamic limit.

Central limit theorem and conclusion

According to the previous result, we concentrate on the operator $\hat{\Delta}_L$ defined above. Since $\langle\hat{\delta}_r\hat{\delta}_s\rangle = \langle\hat{\delta}_r\rangle\langle\hat{\delta}_s\rangle$ its expectation value over the state $|\phi(n)\rangle$ is:

$$\langle\phi(n)|\hat{\Delta}_L|\phi(n)\rangle = \frac{1}{(L-1)}\sum_{i\neq j}\left[(\langle\cos\hat{\theta}_i\rangle-\chi)(\langle\cos\hat{\theta}_j\rangle-\chi))\right] \tag{D.15}$$

Each of the two sums represents the fluctuations of a set of independent, random variables: we can apply the central limit theorem and state that $1/(L-1)\sum_{i\neq j}(\langle\cos\hat{\theta}_i\rangle - \chi) \sim 1/\sqrt{L}$. It follows that $\langle\phi(n)|\hat{\Delta}_L|\phi(n)\rangle \sim \sqrt{L}$: since the fluctuation term in the Hamiltonian grows less than extensively it can be neglected in the thermodynamic limit. We conclude that the mean field approach is therefore exact.

Appendix E

Details about the mean field analysis

In this Appendix we report some details concerning the dynamics of the mean field parameter in order to show the features which make it different from a pure white noise signal. We will indicate with $\epsilon = J/K$. We focus on the analysis of the dynamics of the following quantities:

1. the kinetic energy $E(n) = \overline{\langle \hat{p}^2 \rangle_n}/2$ averaged over the initial conditions (for each evolution we define $\langle \hat{p}^2 \rangle_n \equiv \langle \psi(n) | \, \hat{p}^2 \, | \psi(n) \rangle$);
2. the power spectrum $P(\omega) = |\widetilde{\psi}_\omega|^2$, where $\widetilde{\psi}_\omega$ are the Fourier coefficients of $\overline{\psi_{MF}(n)}$;
3. the power spectrum $P_{ac}(\omega; n_0) = |\widetilde{c}_{MF}(\omega; n_0)|^2$, where we define the correlator

$$c_{MF}(k; n_0) = \overline{\psi_{MF}(n_0)\psi_{MF}(n_0 + k)} - \overline{\psi_{MF}(n_0)}\,\overline{\psi_{MF}(n_0 + k)}; \tag{E.1}$$

4. the variance of the mean field parameter, defined as

$$\sigma_{MF}(n) = \overline{\psi_{MF}(n)^2} - \left(\overline{\psi_{MF}(n)}\right)^2. \tag{E.2}$$

Power spectrum $P(\omega)$

In the study of $P(\omega)$ we distinguish its behavior at low and high frequencies: at low frequency we observe either a power law decay in ω or a constant power spectrum depending on whether (K, ϵ) are in the subdiffusive or diffusive region.

The low frequencies behavior is shown in panel (a) of Figure E.1: we plot $P(\omega)$ for two cases, one corresponding to subdiffusion, with a small value of ϵ, and one to diffusion of momentum. In the first case (continuous line) a power-law behavior is observed, while in the second (dashed line) the power spectrum is flat in ω. The dependence of the power law exponent of $P(\omega)$ on K and ϵ is shown in Figure E.2, where we consider $K = 4.0$, panel (a), and $K = 11.0$, panel (b). The dynamics is described by the full green squares which represent the power law exponent of the kinetic energy growth. The exponent of $P(\omega)$ vanishes (empty blue squares) when the dynamics is diffusive and it is negative when it is subdiffusive.

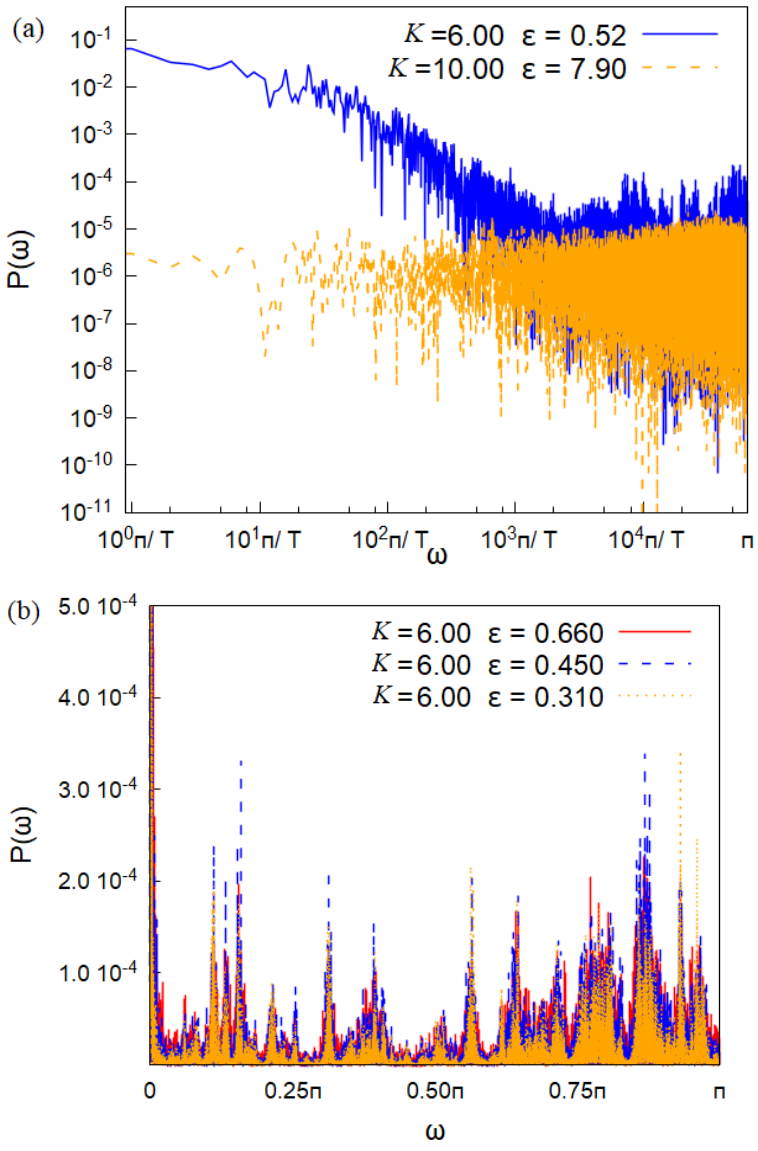

Figure E.1: (a) The low frequencies behavior of $P(\omega)$ is plotted for a case in which the dynamics is diffusive (dashed line) and another in which it is subdiffusive manifests (continuous line). $\mathcal{T} = 65536$ is the length of the time interval which has been used to compute the Fourier transform; it coincides with the number of frequencies which has been considered. (b) High frequencies behavior of $P(\omega)$ for a fixed value of K and different values of ϵ: the positions of the peaks almost coincide. The norm of the power spectrum has been normalized to unity in order to enhance the visibility of the peaks within the same order of magnitude. In the simulations $\hbar = 2.79$.

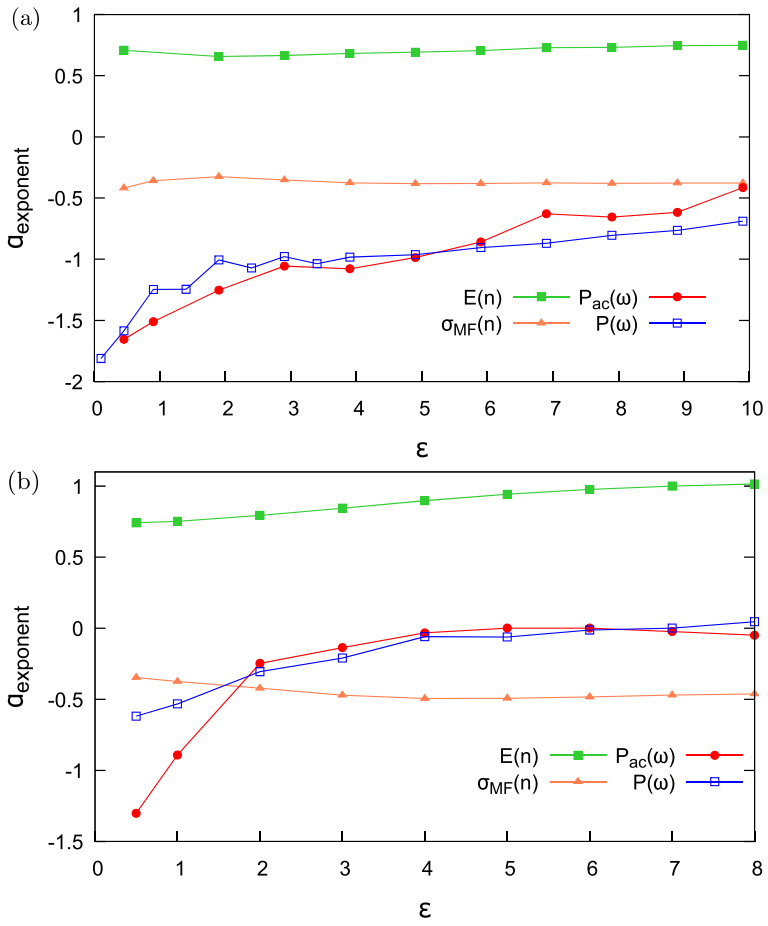

Figure E.2: The power-law exponents for $E(n)$ and $\sigma_{MF}(n)$ in the time domain and for $P(\omega)$ and $P_{ac}(\omega)$ in frequency domain are plotted. (a) $K = 4.0$: the exponents relative to $E(n)$ and $\sigma_{MF}(n)$ (green square and orange triangles respectively) are uniform in ϵ; the power laws exponents of the power spectra (red circles for $P(\omega)$ and empty blue ones for $P_{ac}(\omega)$) increase with ϵ. (b) $K = 11.0$: the dynamics of the system passes from subdiffusive to diffusive when ϵ is increased. The exponents of the power laws of $P(\omega)$ and $P_{ac}(\omega)$ vanish when the dynamics is diffusive. In the simulations $\hbar = 2.79$.

The high frequency behavior of $P(\omega)$ is characterized by a series of peaks whose positions depend on K; by increasing ϵ they spread and become smoother until they disappear when the system enters the diffusive region of the (K, ϵ) plane. In panel (b) of Figure E.1 this property is shown plotting the power spectrum for increasing values of ϵ at fixed K: we chose $\epsilon \leqslant 1$ it clearly appears that the peaks coincide in the three cases.

Power spectrum $P_{ac}(\omega)$

Let us now discuss the power spectrum of the time-correlator $P_{ac}(\omega; n_0)$ at different n_0: if the process $\psi_{MF}(n)$ is stationary, the time-correlator $c(k; n_0)$ and its power spectrum are independent on n_0. The small frequency results for our case are shown in panel (a) of Figure E.3 where we plot $P_{ac}(\omega; n_0)$ corresponding to $n_0 = 10^3$ and $n_0 = 10^4$: the two curves show a power-law behavior at low ω with the same exponent. The larger is n_0, however, the smaller the amplitude of $P_{ac}(\omega)$. It follows that $c_{MF}(k; n_0)$ scales to 0 as n_0 is increased: this result leads us to conclude that $\psi_{MF}(n)$ is not a stationary signal.

As already mentioned, $P_{ac}(\omega; n_0)$ decays like a power law in the subdiffusive region of the (K, ϵ) plane. This behavior is smoothed by increasing ϵ or K until it disappears when diffusion starts: the exponent of the power law reduces and a uniform region at low ω appears. In the diffusive region of the (K, ϵ) plane $P_{ac}(\omega)$ is flat.

In panel (b) of Figure E.3 we qualitatively show how $P_{ac}(\omega; n_0)$ changes as ϵ is increased. We consider $K = 3.0$, for which the system is always in the subdiffusive region (see Figure 4.2), and $K = 10.0$, for which the system passes from subdiffusive to diffusive as ϵ is increased. In the first case $P_{ac}(\omega)$ exhibits a power-law behavior at low frequencies for $\epsilon = 2.0$: this behavior is smoothed out when $\epsilon = 7.0$. In the second case the power-law behavior is much less evident when $\epsilon = 1.0$; it completely disappears when $\epsilon = 7.9$ and the system is diffusive. In Figure E.2 the power law exponents relative to $P_{ac}(\omega)$ are plotted (red circles): for $K = 4.0$, see panel (a), the exponent approaches the value of -0.5 without vanishing. On the other side in panel (b) we set $K = 11.0$ and it vanishes for $\epsilon > 4.0$: indeed for higher values of ϵ the system is diffusive.

At high frequencies $P_{ac}(\omega; n_0)$ is characterized by some peaks whose positions depend on K, similarly to what has been found for $P(\omega)$.

Variance of the mean field parameter $\sigma_{MF}(n)$

Let us now turn to $\sigma_{MF}(n)$ which is found to show a power law behavior, much clearer and robust than the one exhibited by $P_{ac}(\omega; n_0)$ and $P(\omega)$. In the subdiffusive region $\sigma_{MF}(n)$ decreases as $n^{-\beta}$, with β slightly varying between to $0.3 \div 0.4$ while in the diffusive one $\sigma_{MF}(n) \sim n^{-\beta}$ with $\beta \simeq 0.5$. In Figure E.4 $\sigma_{MF}(n)$ is plotted in two particular cases, one in the subdiffusive region and the other in the diffusive one.

In panel (a) of Figure E.2 we set $K = 4.0$: the system is always subdiffsive and the power law exponent of σ_{MF} (orange triangles) is constant as ϵ is varied. In panel (b) we set $K = 11.0$: the system passes from subdiffusive to diffusive for $\epsilon = 4.0$ as it can be seen in Figure 4.2. Accordingly, the exponent of σ_{MF} tends to -0.5; this transition is also enhanced by the exponent of the time-correlator (red circles) which vanishes at $\epsilon = 4.0$. Of course, the behavior of $\sigma_{MF}(n)$ clearly shows that $c_{MF}(k = 0; n_0)$ is

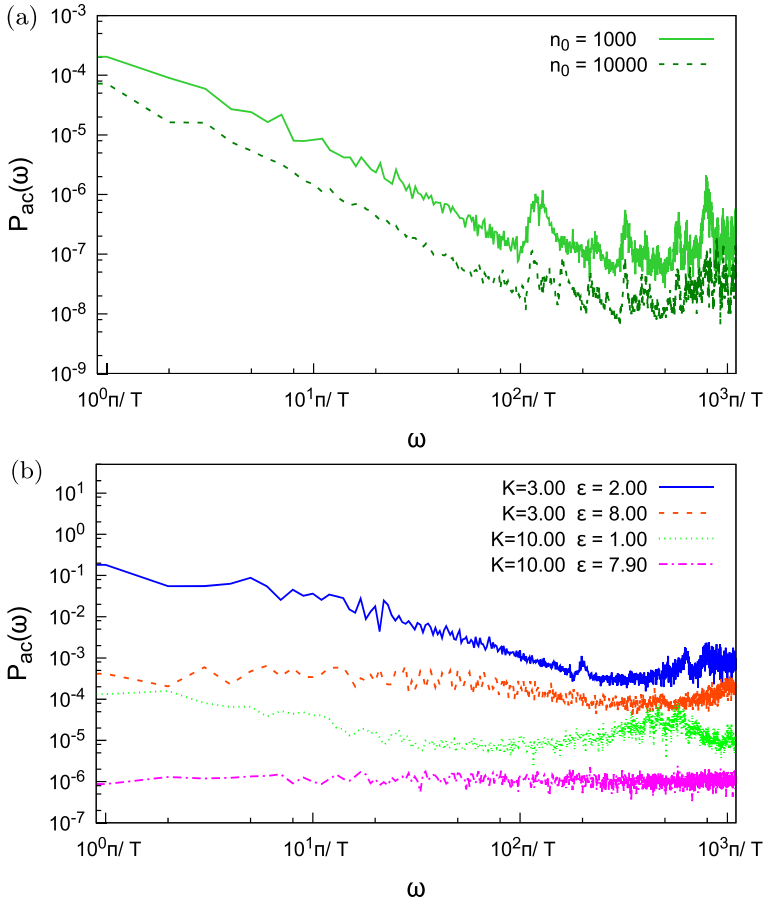

Figure E.3: (a) $P_{ac}(\omega; n_0)$ is plotted for two values of n_0: in the low frequencies region the slope of the curves is the same while the initial amplitude changes. This scaling is related to the power-law time dependence of σ_{MF}. Numerical parameters: $K = 6.0$ and $\epsilon = 0.52$. (b) A power-law behavior can be observed in the curve corresponding to $K = 3.00$, $\epsilon = 2.00$ (first curve from above) and it flattens as K and ϵ are increased. The bottom line has been shifted down by an order of magnitude for a better visibility. In the simulations $\hbar = 2.79$.

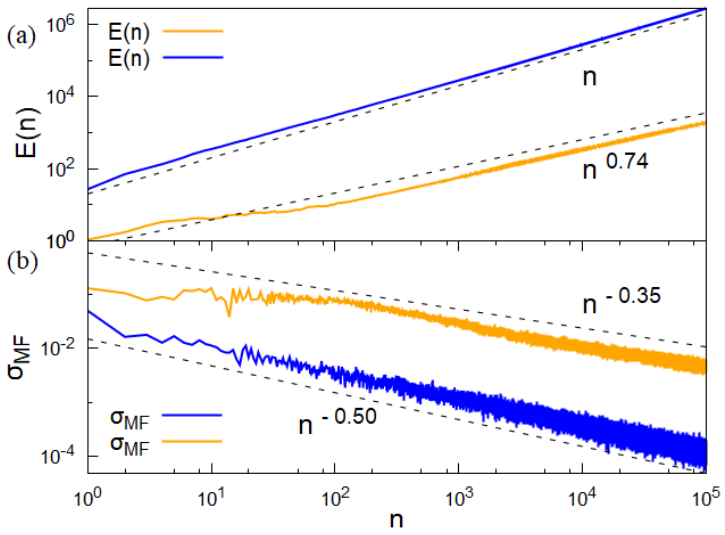

Figure E.4: Two cases of dynamics are considered, a diffusive one with $K = 30.0$, $\epsilon = 4.90$ (blue, dark line, color online) and a subdiffusive one with $K = 6.0$, $\epsilon = 0.52$ (orange, light one). (a) The growth of the kinetic energy is plotted for the two cases; the dotted lines stresses the relative slopes. (b) The evolution of σ_{MF} is plotted for the two cases so the corresponding power law behaviors are enhanced.

not stationary. In order to better understand how the features we are analyzing are relevant for the dynamics of our system we generate two artificial signals, $\phi(n)$ and $f(n)$, with some of the spectral properties we have found in $\psi_{MF}(n)$ and study the dynamics of a system perturbed by them instead of $\psi_{MF}(n)$. The first signal $\phi(n)$ has a power spectrum like the one in Figure E.1 (power law behavior in panel (a)) and random phases assigned to the Fourier coefficients: the corresponding evolution operator, according to the definition in Eq.(4.1.7), contains the kicking modulation $K'(n) = K - J\phi(n)$. The dynamics of this system is found to be subdiffusive up to a finite time, after which $E(n)$ grows linearly in time, analogously to what was found in the classical system in Ref. [119]: this means that the features of $P(\omega)$ are not a sufficient ingredient to reproduce the power law growth of $E(n)$. On the other side, if we take $K''(n) = K - J\phi(n))$, where $f(n)$ is a stationary white noise process, the power law is uniform in ω and the energy grows linearly in time. Therefore, while some features of the dynamics obtained can be associated to the properties of the time series the robust subdiffusion observed cannot be reproduced by a simple Gaussian process.

Appendix F

Crossover region

The crossover region appears first of all by looking at the value of the level spacing ratio $\langle r \rangle$ which smoothly interpolates between the Poisson value and the Wigner Dyson one (see Figure 3.4). Now we want to investigate the properties of the system in this range of values, by focusing on a line in the parameters space with $J/\hbar = 0.3$. We will show that in this region there is a coexistence of localized and delocalized states and that this coexistence persists when we increase M up to the maximum value allowed by computational limitations.

We start by looking at the scaling properties of the IPR in order to check whether the Floquet eigenstates are localized or not.We find that the averaged IPR decreases as the local truncation M is increased, but the behavior is slower than a power law, differently from what we found in the delocalized region. We can see this in the panels of Figure F.1 in which the red curves (circle points) show the IPR for $K/\hbar = 0.5, 0.7, 0.9, 1.1$ (panels (a),..., (d) respectively).

We observe a straight power law decaying of the IPR for small values of M in panel (d) which then slows down at higher values of the truncation. We can interpret this behavior by saying that localized and delocalized states participate to the mean IPR; for small values of M the support of the localized states is larger than the truncated Hilbert space and therefore the IPR of all the states, both the localized and the delocalized ones, decays as a power law with M. At larger truncations the IPRs of the localized and delocalized states behave differently and the decaying of the averaged IPR changes consequently.

In order to understand the role played by the fluctuations of the IPR_α we plot the log-average IPR_{log} in Figure F.1 (yellow squares). The curve relative to the mean IPR and to the log one do not coincide, revealing the presence of fluctuations, but neither they strongly diverge. This means that stronger fluctuations may emerge by considering the IPR relative to another basis of vectors, namely the eigenstates of the angular momentum. To the purpose of testing this hypothesis we define the inverse participation ratio of the angular momentum eigenstates as

$$\mathrm{IPR}_{\mathbf{m}} := \sum_\alpha |\langle \phi_\alpha | \mathbf{m} \rangle|^4. \tag{F.1}$$

If we consider a momentum eigenstate as initial state and we let it evolve in time it can be easily shown that $\mathrm{IPR}_{\mathbf{m}}$ is invariant during the evolution: this means that $\mathrm{IPR}_{\mathbf{m}}$ can tell us if the dynamics of a given initial state will be localized or not in

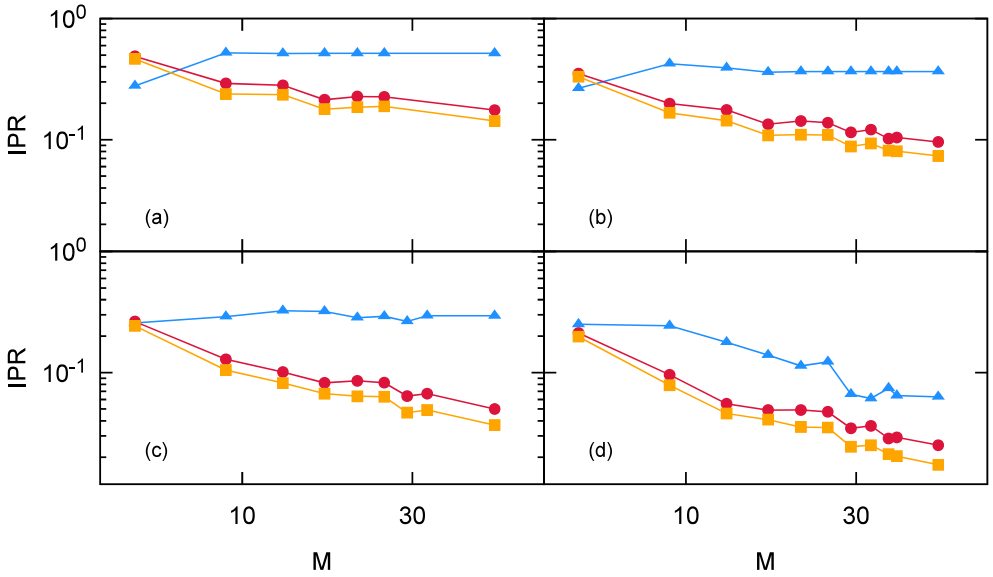

Figure F.1: In this log-log plot we show how in the crossover region the IPR of the zero momentum angular momentum eigenstate (blue triangles) passes from being constant in M to decreasing with M, while the averaged IPR (red circles) always decreases. We plot also the logarithmic average (yellow squares) to show that fluctuations in the IPR, given by localized states, reduces the slope of the scaling. In panels (a) ,... (d) we have $K/\hbar = 0.5, 0.7, 0.9, 1.1$ respectively. Other parameters: $L = 3$, $\hbar = 5.0$.

the angular momentum space. Indeed if $\mathrm{IPR}_{\mathbf{m}}$ is constant as M is increased it means that the state $\mathbf{m}$ has a finite support in the Hilbert space and its dynamics will be localized, while if $\mathrm{IPR}_{\mathbf{m}}$ scales with M the dynamics is delocalized.

We apply this argument to a particular momentum eigenstate, namely $|\mathbf{0}\rangle = |m_1 = 0, ..., m_L = 0\rangle$. The peculiarity of this state is that it is the one which is more distant from the Hilbert space boundary and therefore less affected by finite size effects. It follows that we can look at $\mathrm{IPR}_{\mathbf{0}}$ to verify that the scaling of the IPR in the intermediate region is due to states with different localization properties.

In Figure F.1 we plot the scaling of $\mathrm{IPR}_{\mathbf{0}}$ (blue curve with triangular points) compared to the IPR. It emerges that $\mathrm{IPR}_{\mathbf{0}}$ reaches a constant value against M while on the contrary the IPR does not: this means that in this region of the parameters space there are momentum eigenstates which are localized and other which are not. We conclude by arguing that the Floquet eigenstates present a fractal behavior, which emerges by looking at the scaling properties of the IPR. Also, it emerges that in the local basis of the angular momentum there is a coexistence of localized and delocalized eigenstates. This result is in agreement which preceding results stating the absence of a mobility edge in the Floquet eigenstates [158] and allow us to predict that in this region the dynamics of the system would depend on the kinetic energy of the initial state.

Bibliography

[1] Anderson, P. W. (1972) More is different. *Science*, **177**, 393–396.

[2] Bukov, M., D'Alessio, L., and Polkovnikov, A. (2015) Universal high-frequency behavior of periodically driven systems: from dynamical stabilization to floquet engineering. *Advances in Physics*, **64**, 139–226.

[3] Nature Publishing Group (2016) Topology on top. *Nature Physics*, **12**, 615, editorial.

[4] Oka, T. and Aoki, H. (2009) Photovoltaic hall effect in graphene. *Phys. Rev. B*, **79**, 081406.

[5] Jiang, L., Kitagawa, T., Alicea, J., Akhmerov, A. R., Pekker, D., Refael, G., Cirac, J. I., Demler, E., Lukin, M. D., and Zoller, P. (2011) Majorana fermions in equilibrium and in driven cold-atom quantum wires. *Phys. Rev. Lett.*, **106**, 220402.

[6] Lindner, N. H., Refael, G., and Galitski, V. (2011) Floquet topological insulator in semiconductor quantum wells. *Nature Physics*, **7**, 490 EP –, article.

[7] Ando, T., Matsumoto, Y., and Uemura, Y. (1975) Theory of hall effect in a two-dimensional electron system. *Journal of the Physical Society of Japan*, **39**, 279–288.

[8] Thouless, D. J. (1983) Quantization of particle transport. *Phys. Rev. B*, **27**, 6083–6087.

[9] Laughlin, R. B. (1981) Quantized hall conductivity in two dimensions. *Phys. Rev. B*, **23**, 5632–5633.

[10] Prange, R. E. and Girvin, S. M. (1990) The quantum hall effect. Includes bibliographical references.

[11] Wang, Y. H., Steinberg, H., Jarillo-Herrero, P., and Gedik, N. (2014) Observation of floquet-bloch states on the surface of a topological insulator. *19th International Conference on Ultrafast Phenomena*, p. 10.Thu.A.2, Optical Society of America.

[12] Mahmood, F., Chan, C.-K., Alpichshev, Z., Gardner, D., Lee, Y., Lee, P. A., and Gedik, N. (2016) Selective scattering between floquet-bloch and volkov states in a topological insulator. *Nature Physics*, **12**, 306 EP –.

[13] Dagotto, E. (1994) Correlated electrons in high-temperature superconductors. *Rev. Mod. Phys.*, **66**, 763–840.

[14] Lee, P. A., Nagaosa, N., and Wen, X.-G. (2006) Doping a mott insulator: Physics of high-temperature superconductivity. *Rev. Mod. Phys.*, **78**, 17–85.

[15] Keimer, B., Kivelson, S. A., Norman, M. R., Uchida, S., and Zaanen, J. (2015) From quantum matter to high-temperature superconductivity in copper oxides. *Nature*, **518**, 179 EP –, review Article.

[16] Kennes, D. M., Wilner, E. Y., Reichman, D. R., and Millis, A. J. (2017) Transient superconductivity from electronic squeezing of optically pumped phonons. *Nature Physics*, **13**, 479 EP –, article.

[17] Kennes, D. M., Claassen, M., Sentef, M. A., and Karrasch, C. (2018) Light-induced d-wave superconductivity through Floquet-engineered Fermi surfaces in cuprates. *ArXiv e-prints*.

[18] Eckardt, A., Weiss, C., and Holthaus, M. (2005) Superfluid-insulator transition in a periodically driven optical lattice. *Phys. Rev. Lett.*, **95**, 260404.

[19] Liu, G., Hao, N., Zhu, S.-L., and Liu, W. M. (2012) Topological superfluid transition induced by a periodically driven optical lattice. *Phys. Rev. A*, **86**, 013639.

[20] Polkovnikov, A., Sengupta, K., Silva, A., and Vengalattore, M. (2011) Nonequilibrium dynamics of closed interacting quantum systems. *Rev. Mod. Phys.*, **83**, 863.

[21] Feynman, R. P. (1982) Simulating physics with computers. *International journal of theoretical physics*, **21**, 467–488.

[22] Tarruell, L. and Sanchez-Palencia, L. (2018) Quantum simulation of the Hubbard model with ultracold fermions in optical lattices. *ArXiv e-prints*.

[23] Gross, C. and Bloch, I. (2017) Quantum simulations with ultracold atoms in optical lattices. *Science*, **357**, 995–1001.

[24] Greiner, M., Mandel, O., Esslinger, T., Hänsch, T. W., and Bloch, I. (2002) Quantum phase transition from a superfluid to a mott insulator in a gas of ultracold atoms. *Nature*, **415**, 39 EP –, article.

[25] Jördens, R., Strohmaier, N., Günter, K., Moritz, H., and Esslinger, T. (2008) A mott insulator of fermionic atoms in an optical lattice. *Nature*, **455**, 204.

[26] Lepers, M. and Dulieu, O. (2017) Long-range interactions between ultracold atoms and molecules. *ArXiv e-prints*.

[27] Livi, L. F., et al. (2016) Synthetic dimensions and spin-orbit coupling with an optical clock transition. *Phys. Rev. Lett.*, **117**, 220401.

[28] Jaksch, D. and Zoller, P. (2003) Creation of effective magnetic fields in optical lattices: the hofstadter butterfly for cold neutral atoms. *New Journal of Physics*, **5**, 56.

[29] Zohar, E., Cirac, J. I., and Reznik, B. (2015) Quantum simulations of lattice gauge theories using ultracold atoms in optical lattices. *Reports on Progress in Physics*, **79**, 014401.

[30] Rigol, M., Dunjko, V., and Olshanii, M. (2008) Thermalization and its mechanism for generic isolated quantum systems. *Nature*, **452**, 854 EP –.

[31] Kaufman, A. M., Tai, M. E., Lukin, A., Rispoli, M., Schittko, R., Preiss, P. M., and Greiner, M. (2016) Quantum thermalization through entanglement in an isolated many-body system. *Science*, **353**, 794–800.

[32] D'Alessio, L., Kafri, Y., Polkovnikov, A., and Rigol, M. (2016) From quantum chaos and eigenstate thermalization to statistical mechanics and thermodynamics. *Advances in Physics*, **65**, 239–362.

[33] Gogolin, C. and Eisert, J. (2016) Equilibration, thermalisation, and the emergence of statistical mechanics in closed quantum systems. *Reports on Progress in Physics*, **79**, 056001.

[34] Faddeev, L. (1980) Soviet scientific reviews sect. *C*, **1**, 107.

[35] Basko, D., Aleiner, I., and Altshuler, B. (2006) Metal–insulator transition in a weakly interacting many-electron system with localized single-particle states. *Annals of Physics*, **321**, 1126 – 1205.

[36] Imbrie, J. Z. (2016) On many-body localization for quantum spin chains. *Jour. Stat. Phys*, **163**, 998–1048.

[37] Anderson, P. W. (1958) Absence of diffusion in certain random lattices. *Phys. Rev.*, **109**, 1492–1505.

[38] Thouless, D. (1974) Electrons in disordered systems and the theory of localization. *Physics Reports*, **13**, 93 – 142.

[39] Ros, V., Mueller, M., and Scardicchio, A. (2015) Integrals of motion in the many-body localized phase. *Nuclear Physics B*, **891**, 420–465.

[40] Chandran, A., Kim, I. H., Vidal, G., and Abanin, D. A. (2015) Constructing local integrals of motion in the many-body localized phase. *Physical Review B*, **91**, 085425.

[41] Bordia, P., Lüschen, H., Schneider, U., Knap, M., and Bloch, I. (2017) Periodically driving a many-body localized quantum system. *Nature Physics*, **13**, 460–464.

[42] D'Alessio, L. and Rigol, M. (2014) Long-time Behavior of Isolated Periodically Driven Interacting Lattice Systems. *Phys. Rev. X*, **4**, 041048.

[43] Lazarides, A., Das, A., and Moessner, R. (2014) Equilibrium states of generic quantum systems subject to periodic driving. *Phys. Rev. E*, **90**, 012110.

[44] Russomanno, A., Fazio, R., and Santoro, G. E. (2015) Thermalization in a periodically driven fully connected quantum Ising ferromagnet. *EPL*, **110**, 37005.

[45] Ponte, P., Papić, Z., Huveneers, F., and Abanin, D. A. (2015) Many-body localization in periodically driven systems. *Phys. Rev. Lett.*, **114**, 140401.

[46] Lazarides, A., Das, A., and Moessner, R. (2015) Fate of many-body localization under periodic driving. *Phys. Rev. Lett.*, **115**, 030402.

[47] Abanin, D. A., Roeck, W. D., and Huveneers, F. (2016) Theory of many-body localization in periodically driven systems. *Annals of Physics*, **372**, 1 – 11.

[48] Schreiber, M., Hodgman, S. S., Bordia, P., Lüschen, H. P., Fischer, M. H., Vosk, R., Altman, E., Schneider, U., and Bloch, I. (2015) Observation of many-body localization of interacting fermions in a quasi-random optical lattice. *Science*.

[49] Abanin, D. A., De Roeck, W., and Huveneers, F. m. c. (2015) Exponentially slow heating in periodically driven many-body systems. *Phys. Rev. Lett.*, **115**, 256803.

[50] Abanin, D. A., De Roeck, W., Ho, W. W., and Huveneers, F. m. c. (2017) Effective hamiltonians, prethermalization, and slow energy absorption in periodically driven many-body systems. *Phys. Rev. B*, **95**, 014112.

[51] Bukov, M., Heyl, M., Huse, D. A., and Polkovnikov, A. (2016) Heating and many-body resonances in a periodically driven two-band system. *Phys. Rev. B*, **93**, 155132.

[52] Mori, T., Ikeda, T. N., Kaminishi, E., and Ueda, M. (2018) Thermalization and prethermalization in isolated quantum systems: a theoretical overview. *Journal of Physics B Atomic Molecular Physics*, **51**, 112001.

[53] Weidinger, S. A. and Knap, M. (2017) Floquet prethermalization and regimes of heating in a periodically driven, interacting quantum system. *Scientific Reports*, **7**, 45382.

[54] Citro, R., Torre, E. G. D., D'Alessio, L., Polkovnikov, A., Babadi, M., Oka, T., and Demler, E. (2015) Dynamical stability of a many-body kapitza pendulum. *Annals of Physics*, **360**, 694 – 710.

[55] Huang, B., Wu, Y.-H., and Liu, W. V. (2018) Clean floquet time crystals: Models and realizations in cold atoms. *Phys. Rev. Lett.*, **120**, 110603.

[56] Russomanno, A., Iemini, F., Dalmonte, M., and Fazio, R. (2017) Floquet time crystal in the lipkin-meshkov-glick model. *Phys. Rev. B*, **95**, 214307.

[57] Else, D. V., Bauer, B., and Nayak, C. (2016) Floquet time crystals. *Phys. Rev. Lett.*, **117**, 090402.

[58] Chirikov, B. V. (1979) A universal instability of many-dimensional oscillator systems. *Physics Reports*, **52**, 263 – 379.

[59] Casati, G., Chirikov, B. V., Ford, J., and M., I. F. (1979) Stochastic behaviour of classical and quantum hamiltonian systems. *Lecture Notes in Physics*, vol. 93 , p. 334, Springer.

[60] Fishman, S., Grempel, D. R., and Prange, R. E. (1982) Chaos, quantum recurrences, and anderson localization. *Phys. Rev. Lett.*, **49**, 509–512.

[61] Grempel, D. R., Prange, R. E., and Fishman, S. (1984) Quantum dynamics of a nonintegrable system. *Phys. Rev. A*, **29**, 1639.

[62] Abrahams, E., Anderson, P. W., Licciardello, D. C., and Ramakrishnan, T. V. (1979) Scaling theory of localization: Absence of quantum diffusion in two dimensions. *Phys. Rev. Lett.*, **42**, 673.

[63] Notarnicola, S., Iemini, F., Rossini, D., Fazio, R., Silva, A., and Russomanno, A. (2018) From localization to anomalous diffusion in the dynamics of coupled kicked rotors. *Phys. Rev. E*, **97**, 022202.

[64] Roy, S., Lev, Y. B., and Luitz, D. J. (2018) Anomalous thermalization and transport in disordered interacting floquet systems. *Phys. Rev. B*, **98**, 060201.

[65] Alet, F. and Laflorencie, N. (2018) Many-body localization: An introduction and selected topics. *Comptes Rendus Physique*.

[66] Gring, M., Kuhnert, M., Langen, T., Kitagawa, T., Rauer, B., Schreitl, M., Mazets, I., Smith, D. A., Demler, E., and Schmiedmayer, J. (2012) Relaxation and prethermalization in an isolated quantum system. *Science*, **337**, 1318–1322.

[67] Langen, T., Gasenzer, T., and Schmiedmayer, J. (2016) Prethermalization and universal dynamics in near-integrable quantum systems. *Journal of Statistical Mechanics: Theory and Experiment*, **2016**, 064009.

[68] von Neumann, J. (2010) Proof of the ergodic theorem and the h-theorem in quantum mechanics. *The European Physical Journal H*, **35**, 201–237.

[69] Deutsch, J. M. (1991) Quantum statistical mechanics in a closed system. *Phys. Rev. A*, **43**, 2046–2049.

[70] Srednicki, M. (1994) Chaos and quantum thermalization. *Phys. Rev. E*, **50**, 888–901.

[71] Deutsch, J. M. (2018) Eigenstate thermalization hypothesis. *Reports on Progress in Physics*, **81**, 082001.

[72] Jancel, R. (1969) *Foundations of classical and quantum statistical mechanics*. International series of monographs in natural philosophy, Pergamon Press.

[73] Deutsch, J. M. (1991) Quantum statistical mechanics in a closed system. *Phys. Rev. A*, **43**, 2046–2049.

[74] Berry, M. V. (1981) Regularity and chaos in classical mechanics, illustrated by three deformations of a circular 'billiard'. *European Journal of Physics*, **2**, 91.

[75] Shinbrot, T., Grebogi, C., Wisdom, J., and Yorke, J. A. (1992) Chaos in a double pendulum. *American Journal of Physics*, **60**, 491–499.

[76] Poincaré, H. (1992) *New methods of celestial mechanics*, vol. 13. Springer Science & Business Media.

[77] Constantin, P. and Foias, C. (1988) *Navier-stokes equations*. University of Chicago Press.

[78] Berry, M. V. (1983) Semiclassical mechanics of regular and irregular motion. G. Ioos, R. S., R. H. G. Helleman (ed.), *Les Houches, Session XXXVI, 1981 — Chaotic Behaviour of Deterministic Systems*, pp. 174–271, North-Holland Publishing Company.

[79] Arnold, L., Crauel, H., and Eckmann, J. (1991) *Lyapunov exponents: proceedings of a conference held in Oberwolfach, May 28-June 2, 1990*. Lecture notes in mathematics, Springer-Verlag.

[80] Angelo, V., Fabio, C., and Massimo, C. (2009) *Chaos: From Simple Models To Complex Systems*, vol. 17. World Scientific.

[81] Kitaev, A. (2018) Hidden correlations in the hawking radiation and thermal noise. *talk given at the fundamental physics prize symposium*, caltech.

[82] Aleiner, I. L., Faoro, L., and Ioffe, L. B. (2016) Microscopic model of quantum butterfly effect: Out-of-time-order correlators and traveling combustion waves. *Annals of Physics*, **375**, 378 – 406.

[83] Mehta, M. L. (2004) 27 - restricted trace ensembles. Mehta, M. L. (ed.), *Random Matrices*, vol. 142 of *Pure and Applied Mathematics*, pp. 487 – 493, Elsevier.

[84] Haake, F. (2001) *Quantum Signatures of Chaos (*2^{nd} *ed)*. Springer.

[85] Bohigas, O., Giannoni, M. J., and Schmit, C. (1984) Characterization of chaotic quantum spectra and universality of level fluctuation laws. *Phys. Rev. Lett.*, **52**, 1.

[86] Porter, C. (1965) *Statistical Theories of Spectra: Fluctuations : a Collection of Reprints and Original Papers*. Perspectives in physics : A series of reprint collections, Acad. Press.

[87] Haq, R. U., Pandey, A., and Bohigas, O. (1982) Fluctuation properties of nuclear energy levels: Do theory and experiment agree? *Phys. Rev. Lett.*, **48**, 1086–1089.

[88] Camarda, H. S. and Georgopulos, P. D. (1983) Statistical behavior of atomic energy levels: Agreement with random-matrix theory. *Phys. Rev. Lett.*, **50**, 492–495.

[89] Poilblanc, D., Ziman, T., Bellissard, J., Mila, F., and Montambaux, G. (1993) Poisson vs. goe statistics in integrable and non-integrable quantum hamiltonians. *Europhys. Lett.*, **22**, 537–542.

[90] Oganesyan, V. and Huse, D. A. (2007) Localization of interacting fermions at high temperature. *Phys. Rev. B*, **75**, 155111.

[91] Royal Society of London (1985) Semiclassical theory of spectral rigidity. *Proceedings of the Royal Society of London A: Mathematical, Physical and Engineering Sciences*, **400**, 229–251.

[92] Müller, S., Heusler, S., Braun, P., Haake, F., and Altland, A. (2004) Semiclassical foundation of universality in quantum chaos. *Phys. Rev. Lett.*, **93**, 014103.

[93] Kos, P., Ljubotina, M., and Prosen, T. c. v. (2018) Many-body quantum chaos: Analytic connection to random matrix theory. *Phys. Rev. X*, **8**, 021062.

[94] Santos, L. F. and Rigol, M. (2010) Onset of quantum chaos in one-dimensional bosonic and fermionic systems and its relation to thermalization. *Phys. Rev. E*, **81**, 036206.

[95] Chirikov, B., Izrailev, F., and Shepelyansky, D. (1988) Quantum chaos: Localization vs. ergodicity. *Physica D: Nonlinear Phenomena*, **33**, 77 – 88.

[96] Sakurai, J. and Napolitano, J. (2011) *Modern Quantum Mechanics*. Addison-Wesley.

[97] Floquet, G. (1883) Sur les équations différentielles linéaires à coefficients périodiques. *Annales scientifiques de l'École Normale Supérieure*, **12**, 47–88.

[98] Shirley, J. H. (1965) Solution of Schrödinger equation with a hamiltonian periodic in time. *Phys. Rev.*, **138**, B979.

[99] Casati, G. and Molinari, L. (1989) "quantum chaos" with time-periodic hamiltonians. *Progress of Theoretical Physics Supplement*, **98**, 287–322.

[100] Casati, G. and Molinari, L. (1989) Quantum chaos with time-periodic hamiltonians. *Progress of Theoretical Physics Supplement*, **98**, 287–322.

[101] Sambe, H. (1973) Steady states and quasienergies of a quantum-mechanical system in an oscillating field. *Phys. Rev. A*, **7**, 2203.

[102] Wegner, F. (1980) Inverse participation ratio in $2+\epsilon$ dimensions. *Zeitschrift für Physik B Condensed Matter*, **36**, 209–214.

[103] Kravtsov, V. E. and Muttalib, K. A. (1997) New class of random matrix ensembles with multifractal eigenvectors. *Phys. Rev. Lett.*, **79**, 1913–1916.

[104] Castellani, C. and Peliti, L. (1986) Multifractal wavefunction at the localisation threshold. *Journal of Physics A: Mathematical and General*, **19**, L429.

[105] Rodriguez, A., Vasquez, L. J., Slevin, K., and Römer, R. A. (2011) Multifractal finite-size scaling and universality at the anderson transition. *Phys. Rev. B*, **84**, 134209.

[106] Pracz, K., Janssen, M., and Freche, P. (1996) Correlation of eigenstates in the critical regime of quantum hall systems. *Journal of Physics: Condensed Matter*, **8**, 7147.

[107] Huckestein, B. and Schweitzer, L. (1994) Relation between the correlation dimensions of multifractal wave functions and spectral measures in integer quantum hall systems. *Phys. Rev. Lett.*, **72**, 713–716.

[108] Salamon, D. (2004) The kolmogorov-arnold-moser theorem. *Math. Phys. Electron. J*, **10**, 1–37.

[109] Greene, J. M. (1979) A method for determining a stochastic transition. *Journal of Mathematical Physics*, **20**, 1183–1201.

[110] Rhombus, D. (2011) *License https://creativecommons.org/licenses/by-sa/3.0/deed.en*.

[111] B.V., C., F.M., I., and D.L., S. (1981) Dynamical stochasticity in classical and quantum mechanics. *Sov. Sci. Rev.*, **2C**.

[112] Moore, F. L., Robinson, J. C., Bharucha, C. F., Sundaram, B., and Raizen, M. G. (1995) Atom optics realization of the quantum δ-kicked rotor. *Phys. Rev. Lett.*, **75**, 4598–4601.

[113] Duffy, G., Parkins, S., Müller, T., Sadgrove, M., Leonhardt, R., and Wilson, A. (2004) Experimental investigation of early-time diffusion in the quantum kicked rotor using a bose-einstein condensate. *Physical Review E*, **70**, 056206.

[114] d'Arcy, M., Godun, R., Oberthaler, M., Cassettari, D., and Summy, G. (2001) Quantum enhancement of momentum diffusion in the delta-kicked rotor. *Physical review letters*, **87**, 074102.

[115] Sadgrove, M., Hilliard, A., Mullins, T., Parkins, S., and Leonhardt, R. (2004) Observation of robust quantum resonance peaks in an atom optics kicked rotor with amplitude noise. *Physical Review E*, **70**, 036217.

[116] Romanelli, A. (2009) Decoherence without classicality in the resonant quantum kicked rotor. *Physical Review A*, **80**, 022102.

[117] Ammann, H., Gray, R., Shvarchuck, I., and Christensen, N. (1998) Quantum delta-kicked rotor: Experimental observation of decoherence. *Physical review letters*, **80**, 4111.

[118] Konishi, T. and Kaneko, K. (1990) Diffusion in hamiltonian chaos and its size dependence. *Journal of Physics A: Mathematical and General*, **23**, L715.

[119] Kaneko, K. and Konishi, T. (1989) Diffusion in hamiltonian dynamical systems with many degrees of freedom. *Phys. Rev. A*, **40**, 6130.

[120] Rajak, A., Citro, R., and Dalla Torre, E. G. (2018) Stability and prethermalization in chains of classical kicked rotors. *ArXiv e-prints*.

[121] Howell, O., Weinberg, P., Sels, D., Polkovnikov, A., and Bukov, M. (2018) Frequency-Controlled Thermalization Phase Transition in a Chaotic Periodically-Driven Classical Spin Chain. *ArXiv e-prints*.

[122] Nekhoroshev, N. N. (1971) Behavior of hamiltonian systems close to integrable. *Functional Analysis and Its Applications*, **5**, 338–339.

[123] Matsui, F., Yamada, H. S., and Ikeda, K. S. (2015) Lifetime of the arrow of time inherent in chaotic eigenstates: case of coupled kicked rotors. *arXiv:1510.00199 [cond-mat.stat-mech]*.

[124] Rozenbaum, E. B. and Galitski, V. (2017) Dynamical localization of coupled relativistic kicked rotors. *Phys. Rev. B*, **95**, 064303.

[125] Toloui, B. and Ballentine, L. E. (2009) Quantum localization for two coupled kicked rotors. *arXiv:0903.4632v2 [quant-ph]*.

[126] Manai, I., Clément, J.-F. m. c., Chicireanu, R., Hainaut, C., Garreau, J. C., Szriftgiser, P., and Delande, D. (2015) Experimental observation of two-dimensional anderson localization with the atomic kicked rotor. *Phys. Rev. Lett.*, **115**, 240603.

[127] Casati, G., Guarneri, I., and Shepelyansky, D. L. (1989) Anderson transition in a one-dimensional system with three incommensurate frequencies. *Phys. Rev. Lett.*, **62**, 345–348.

[128] Wang, J. and García-García, A. M. (2009) Anderson transition in a three-dimensional kicked rotor. *Phys. Rev. E*, **79**, 036206.

[129] Delande, D. (2013) Kicked rotor and anderson localization (lectures 1 and 2), http://boulderschool.yale.edu/sites/default/files/files/Delande-kicked_rotor_lectures_1_and_2.pdf.

[130] Lemarié, G., Chabé, J., Szriftgiser, P., Garreau, J. C., Grémaud, B., and Delande, D. (2009) Observation of the anderson metal-insulator transition with atomic matter waves: Theory and experiment. *Phys. Rev. A*, **80**, 043626.

[131] Keser, A. C., Ganeshan, S., Refael, G., and Galitski, V. (2016) Dynamical many-body localization in an integrable model. *Phys. Rev. B*, **94**, 085120.

[132] Chirikov, B. V. (1991) Time-dependent quantum systems. M.-J.Giannoni, Voros, A., and Zinn-Justin, J. (eds.), *Chaos and quantum mechanics*, vol. 52 of *Les Houches Lecture Series*, p. 443–545, Elsevier Sci. Publ., Amsterdam.

[133] Edwards, J. T. and Thouless, D. J. (1972) Numerical studies of localization in disordered systems. *J. Phys. C*, **5**, 807.

[134] Devakul, T. and Huse, D. A. (2017) Anderson localization transitions with and without random potentials. *Phys. Rev. B*, **96**, 214201.

[135] Roati, G., D'Errico, C., Fallani, L., Fattori, M., Fort, C., Zaccanti, M., Modugno, G., Modugno, M., and Inguscio, M. (2008) Anderson localization of a non-interacting bose–einstein condensate. *Nature*, **453**, 895.

[136] Lemarié, G., Grémaud, B., and Delande, D. (2009) Universality of the anderson transition with the quasiperiodic kicked rotor. *EPL*, **87**, 37007.

[137] Abramowitz, m. and Stegun I. A. (eds.) (1972) *Handbook of Mathematical Functions*. Dover.

[138] Luitz, D. J. and Lev, Y. B. The ergodic side of the many-body localization transition. *Annalen der Physik*, **529**, 1600350.

[139] Luitz, D. J. and Bar Lev, Y. (2016) Anomalous thermalization in ergodic systems. *Phys. Rev. Lett.*, **117**, 170404.

[140] Schomerus, H. and Lutz, E. (2008) Controlled decoherence in a quantum lévy kicked rotator. *Phys. Rev. A*, **77**, 062113.

[141] Doherty, A. C., Vant, K. M. D., Ball, G. H., Christensen, N., and Leonhardt, R. (2000) Momentum distributions for the quantum δ-kicked rotor with decoherence. *Journal of Optics B: Quantum and Semiclassical Optics*, **2**, 605.

[142] Sadgrove, M., Hilliard, A., Mullins, T., Parkins, S., and Leonhardt, R. (2004) Observation of robust quantum resonance peaks in an atom optics kicked rotor with amplitude noise. *Phys. Rev. E*, **70**, 036217.

[143] Abanin D. A., Altman E., Bloch I., Serbyn M. (2018) Ergodicity, entanglement and many-body localization. *arXiv:1804.11065 [cond-mat.dis-nn]*.

[144] Relaño, A. (2018) Anomalous thermalization in quantum collective models. *Phys. Rev. Lett.*, **121**, 030602.

[145] Suret, P., Randoux, S., Jauslin, H. R., and Picozzi, A. (2010) Anomalous thermalization of nonlinear wave systems. *Phys. Rev. Lett.*, **104**, 054101.

[146] Khripkov, C., Vardi, A., and Cohen, D. (2015) Quantum thermalization: anomalous slow relaxation due to percolation-like dynamics. *New Journal of Physics*, **17**, 023071.

[147] Haldar, A., Moessner, R., and Das, A. (2018) Onset of floquet thermalization. *Phys. Rev. B*, **97**, 245122.

[148] Seetharam, K., Titum, P., Kolodrubetz, M., and Refael, G. (2018) Absence of thermalization in finite isolated interacting floquet systems. *Phys. Rev. B*, **97**, 014311.

[149] Bloch, I., Dalibard, J., and Zwerger, W. (2008) Many-body physics with ultracold gases. *Reviews of modern physics*, **80**, 885.

[150] Bloch, I. (2008) Quantum coherence and entanglement with ultracold atoms in optical lattices. *Nature*, **453**, 1016–1022.

[151] Eckardt, A. (2017) Colloquium: Atomic quantum gases in periodically driven optical lattices. *Reviews of Modern Physics*, **89**, 011004.

[152] Houck, A. A., Türeci, H. E., and Koch, J. (2012) On-chip quantum simulation with superconducting circuits. *Nature Physics*, **8**, 292–299.

[153] Stöckmann, H.-J. (2000), Quantum chaos: an introduction.

[154] Ott, E. (2002) *Chaos in dynamical systems (*2^{nd} *Ed.)*. Cambridge University Press.

[155] Ruelle, D. (1993) *Chance and Chaos*. Princeton University Press.

[156] Rammer, J. (2004) *Quantum Transport Theory*. Frontiers in Physics, Avalon Publishing.

[157] Lee, P. A. and Ramakrishnan, T. V. (1985) Disordered electronic systems. *Rev. Mod. Phys.*, **57**, 287.

[158] Kim, H., Ikeda, T. N., and Huse, D. A. (2014) Testing whether all eigenstates obey the eigenstate thermalization hypothesis. *Phys. Rev. E*, **90**, 052105.

Acknowledgments

I would like to express my sincere gratitude to my supervisors, Professors Alessandro Silva and Rosario Fazio, for the work they did in these years. They helped me to understand how to approach a research problem with a lot of hints, suggestions and corrections; at the same time, they always let me free to follow my interests and my intuitions. I would like to thank Angelo as a friend and as a colleague for all the support he gave to me: he has always been available for guiding me with a lot of discussions regarding my research project and for supporting me in some critical moments.

I would like to thank all the Professors I met in SISSA and at ICTP for their contribution to my education. In particular, I would like to thank Professor Kravtsov for the discussions we had, since they have been very stimulating for the last part of my work.

I thank all the SISSA institute, a place in which everyone does his best to create an extremely efficient environment. I would like to acknowledge the support I received in these years from the ICTP institute and in particular the CMSP sector.

I thank Professors Emanuele Dalla Torre and Roberta Citro for their Referee work and for their suggestions to improve my work.

I thank the SISSA Medialab and, in particular, Olga Puccioni and Simona Cerrato for allowing me to discover my interest in scientific communication.

I would like now to say thank you to all the people I met in these four years: they contributed to transforming a simple workplace in a second home. Thank you to all the colleagues and friends which I have met at SISSA and at ICTP: we have shared the working daily routine, good and bad days, as well as unforgettable moments. I hope these friendships will last in the future.

I would like to thank the Agesci scout group Trieste 6o for including me: they gave to me the possibility to continue my growth as an educator, to meet new people and new friends which made my time here unique.

Thanks to my friends, from Bari as well as from all around Italy and beyond, with whom I still share my life events even throughout the distance.

Thanks to all my family for the unconditional and certain support, as proven in these years by phone calls, boxes delivery, visits and even more, up to their presence here today. Thanks to my sister, who will host me in Paris sooner or later and makes me feel better than her by asking me statistical advice for her work.

Thanks to Angela because, more important than all the moments we spent so far together, her being always beside me gives a sense to this goal and to the whole journey towards it.